High-resolution laser spectroscopy and Zeeman effect of NO[3] radical

Tada, Kohei

(Degree)
博士（理学）

(Date of Degree)
2015-03-25

(Date of Publication)
2016-03-01

(Resource Type)
doctoral thesis

(Report Number)
甲第6325号

(URL)
https://hdl.handle.net/20.500.14094/D1006325

Doctoral Dissertation

High-resolution laser spectroscopy and Zeeman effect of NO_3 radical

（NO_3 ラジカルの高分解能レーザー分光とゼーマン効果）

Submitted to Department of Chemistry, Graduate School of Science

in partial fulfillment of the requirements for the degree of

Doctor of Science

at

Kobe University

by

Kohei Tada

January 2015

Table of contents

List of tables

List of figures

Chapter 1. Introduction

1.1. Born-Oppenheimer approximation and high-resolution laser spectroscopy

The Born-Oppenheimer approximation

By 1920s, experiments of molecular system have already revealed that the energy ratio of three types of motion in molecules can be approximately described as (electronic) : (vibrational) : (rotational) ~ 1 : 10^{-2} : 10^{-4}. In order to explain this experimental result theoretically, Born and Oppenheimer [1] introduced a parameter which is sometimes called the Born-Oppenheimer parameter,

$$\kappa = \left(\frac{m}{M} \right)^{1/4}, \tag{1-1}$$

where m is the electron mass and M is an effective average of nuclear masses. Then, they showed that this energy ratio can be described by using a power series of κ, as (electronic) : (vibrational) : (rotational) ~ 1 : κ^2 : κ^4, and demonstrated that these three types of motion may be approximately separated. The coupling terms among them or other small terms correspond to the higher orders of the power series of κ; however, they were not treated in their paper. The separation of three types of motion in molecules is now called the Born-Oppenheimer approximation.

In this Born-Oppenheimer approximation, the Schrödinger equation of a molecule can be separated into the individual equations treating the electronic part and the nuclear part. Accordingly, the total wavefunction of a molecule can be factored into the product of the electronic and the nuclear wavefunctions, and the total energy of a molecule can be given by the sum of the electronic and the nuclear energies. In their paper, they also proved that the eigenfunctions of the Schrödinger equation of the electronic part play the role of potentials for the nuclear motions. Therefore, one can describe the motion of nuclei classically as a swinging ball with an effective mass on the Born-Oppenheimer potential energy surfaces generated by electrons.

Molecular rotations and vibrations [2,3]

Under the rigid rotor approximation, the rotational energy structures of a polyatomic molecule can be completely characterized by the three rotational constants,

$$A = \frac{\hbar^2}{2I_a}, \quad B = \frac{\hbar^2}{2I_b}, \quad C = \frac{\hbar^2}{2I_c}. \tag{1-2}$$

Here, I_a, I_b, and I_c are the *a*, *b*, and *c* axis components, respectively, of the moment of inertia tensor, which are related to the geometrical structure of the molecule in question, and $\hbar$ is reduced Planck's constant, or Dirac's constant. According to the tradition of molecular spectroscopy, three molecular axes are usually supposed to be chosen such that $I_a \leq I_b \leq I_c$;

therefore, $A \geq B \geq C$.

Considering a non-linear N atomic molecule, this molecule has $(3N - 6)$ degrees of freedom of the molecular vibrations. Then, supposing that the amplitudes of the molecular vibrations are infinitesimal comparing to the bond lengths and therefore these vibrations can be treated as the harmonic oscillators obeying the Hooke's law, we may separate any molecular vibrations into the $(3N - 6)$ normal vibrational modes by a transformation matrix. Each normal vibrational mode has the specific vibrational angular frequency

$$\omega = \sqrt{\frac{k}{\mu}} \tag{1-3}$$

or the frequency

$$\nu = \frac{1}{2\pi}\sqrt{\frac{k}{\mu}}\,, \tag{1-4}$$

where k is the effective spring constant and μ is the reduced mass, along the vibrational coordinate in question. The constant k is related to the rigidity of the spring connecting nuclei, i.e., the rigidity of chemical bonds.

High-resolution laser spectroscopy

The Bohr condition

$$\Delta E = h\nu = \hbar\omega, \tag{1-5}$$

suggests that we are able to determine directly the discrete energy separations among the molecular electronic, rotational and vibrational quantum levels from the frequencies of the absorbed or emitted electromagnetic wave caused by molecular system of interest. Here, h is Planck's constant, and v and ω are frequency and angular frequency of the electromagnetic wave interacting with molecules, respectively.

Typical electronic transition energy is in the order of several electron-Volts, or ~ 10^4 cm^{-1}. Considering the Born-Oppenheimer parameter κ, we can roughly estimate the typical vibrational and rotational energies to be 10^2 – 10^3 cm^{-1} and 10^{-1} – 10^0 cm^{-1}, respectively. Simultaneously, higher orders of the power series of κ corresponding to the coupling among the degrees of freedom of molecules and other small perturbations, which may be called the breakdown of the Born-Oppenheimer approximation, may be estimated to be the order of 10^{-3} – 10^{-2} cm^{-1}. This means, if we are able to observe absorption or emission spectra of molecules in high-resolution of 0.001 cm^{-1} or better, we can determine the precise spectroscopic constants of molecules such as the rotational constants and the vibrational frequencies, and also we can find some anomalies of rovibronic transitions such as the transition energy shifts and the line broadening. It is true that the Born-Oppenheimer approximation has been believed as one of the excellent approximations to treat molecules effectively. However, from the point of views of chemistry and chemical reaction, this approximation is crude and we must not ignore the small breakdown of the Born-Oppenheimer approximation, because this small anomaly can

actually play an important role as the starting points of chemical reactions. The mission of the high-resolution laser spectroscopy is to determine the precise molecular constants of the electronically excited molecules, and simultaneously, to reveal experimentally the breakdown of the Born-Oppenheimer approximation. The precise molecular constants provide us the fundamental *static* information such as the molecular geometrical structures and the rigidity of chemical bonds of electronically excited molecules. On the other hand, the spectral anomalies provide us the *dynamic* information of the excited molecules: the energy shifts suggest the rovibronic perturbations by surrounding other rovibronic levels, and the anomalously broadened lines, which indicates anomalously short lifetime of the excited states, may suggest the pre-dissociation of the excited molecules [4-11].

Equation (1-1) suggests that molecules consisting of relatively light nuclei give the larger Born-Oppenheimer parameter κ, leading to the larger coupling in magnitude among the three types of motion in a molecule. Therefore, relatively small and light molecules may be suitable for the purpose of the detailed investigation of the intra-molecular interactions beyond the Born-Oppenheimer approximation.

1.2. Free radicals

Chemistry is one of the important realms of natural science, which often treats the

transformations of materials, i.e., chemical reactions. From the microscopic point of view, we may say that chemical reactions are the process in which old chemical bonds are broken and new chemical bonds are created. Then, we can easily imagine that the molecules with *incomplete chemical bonds* should be existed as the intermediates during the process of chemical reactions. Simultaneously, we can also imagine that these molecules should play an important role to promote the successive chemical reactions, because the *incomplete chemical bonds* must show the chemical instability and must be eager to create *complete chemical bonds*. The wording *incomplete chemical bonds* should be substituted with the wording unpaired electrons, and the molecules with unpaired electrons are called radicals.

Generally speaking, owing to this chemical instability, radicals are so short-lived that people could not isolate and detect them in ancient times, with a few stable exceptions such as O_2 molecule and nitrogen dioxide (NO_2). That is why people had to postulate the existence of free radicals in the era when most of chemical reactions was a kind of black box. However, the development of spectroscopic methods has enabled us to observe free radicals directly. One good example of such free radicals is the Criegee intermediate, which is one of the peroxy radicals. The ozonolysis reaction of alkenes to yield carbonyl compounds is one of the well-known reactions in the field of organic chemistry. During this ozonolysis reaction, the radical called the Criegee intermediate, whose constitutional formula is schematically written as R_1R_2COO, has been predicted to be existed more than 50 years ago [12,13]. Very recently

the Criegee intermediates with simpler structures such as CH_2OO, CH_3CHOO, $(CH_3)_2COO$, and CH_3CH_2CHOO were spectroscopically detected and the precise geometric structures were reported [14-21]. The Criegee intermediate is of importance for not only the ozonolysis reaction of alkenes but also the OH radical generation in the troposphere. Lester and her co-workers reported that the particular vibrational mode promotes the unimolecular reaction of the Criegee intermediates to generate OH radical [21,22].

From the point of views of molecular science and molecular spectroscopy, free radicals are of quite interest because of the non-zero electronic spin angular momentum. This *new* degree of freedom couples with other degrees of freedom in molecular frameworks, and provides us much information about radicals in question through the fine structures and the hyperfine structures in high-resolution spectra.

The electronic spin angular momentum also couples with external magnetic and electric fields, resulting in the Zeeman and Stark splitting of rovibronic levels, respectively. In the case of molecules with zero electronic spin and zero electronic orbital angular momenta, the magnitude of the Zeeman splitting of the rovibronic levels is characterized by the nuclear magneton, $\mu_N = 5.05078 \times 10^{-27}$ J T^{-1}, or 2.54262×10^{-8} G^{-1} cm^{-1}. This means that we need an external magnetic field of 4×10^5 G, or 40 T to observe the Zeeman splitting of the order of 0.01 cm^{-1}. On the other hand, in the case of free radicals with the non-zero electronic spin, we need only an external magnetic field of 2×10^2 G, or 0.02 T to observe the Zeeman splitting

of the order of 0.01 cm^{-1}, because of the Bohr magneton: $\mu_B = 9.27401 \times 10^{-24}$ J T^{-1}, or 4.66864×10^{-5} G^{-1} cm^{-1} which is three orders of magnitude larger than the nuclear magneton. Therefore, in the case of free radicals, we can observe the noticeable Zeeman splitting of rotational lines in high-resolution spectra, even in a weaker external magnetic field. The distinct Zeeman splitting allows us unambiguous rotational assignments even in the massively complicated spectra [23].

1.3. Nitrate radical

This doctoral dissertation focuses on nitrate radical (NO_3). NO_3 is one of the main species of the atmospheric nitrogen oxides (NO_X) in the environment. NO_3 has attracted attention because of the characteristic property in the atmosphere. During the daytime, NO_3 is absent in the atmosphere, because NO_3 is photolyzed by the sunlight to generate $NO_2 + O$ or $NO + O_2$. On the other hand during the night-time without sunlight, NO_3 acts as a NO_X reservoir and as an oxidant among various atmospheric chemical reactions. Therefore, the cycles of NO_3 concentration in day-to-day, season-to-season, and year-to-year as well as the vertical distribution of NO_3 in the atmosphere have been monitored [24-40]. Numerous chemical kinetic investigations on NO_3 radical have been reviewed in a few articles [41,42].

NO_3 strongly absorbs the visible light, and this strong absorption is often used for the

detection of NO_3 in the atmosphere. More than one hundred years ago, NO_3 was identified by this strong visible absorption [43]. Jones and Wulf also reported the absorption spectrograms of NO_3 in the visible region [44]. Based on the molecular orbital theory, Walsh [45] predicted that the ground electronic state $\tilde{X}$ of NO_3 has the A_2' symmetry owing to the …$(4e')^4(1e'')^4(1a_2')^1$ electronic configuration under the assumption of the D_{3h} molecular structure. He also predicted two low-lying excited electronic states; the first excited state $\tilde{A}$ with the E" symmetry owing to the …$(4e')^4(1e'')^3(1a_2')^2$ electronic configuration, and the second excited state $\tilde{B}$ with the E' symmetry owing to the …$(4e')^3(1e'')^4(1a_2')^2$ electronic configuration. He explained that this visible absorption to be due to the optically allowed $\tilde{B}$ $^2E' \leftarrow \tilde{X}\ ^2A_2'$ electronic transition. Later, Walker and Horsley applied the non-empirical LCAO SCF MO method to NO_3 and predicted that the two excited electronic states $\tilde{A}\ ^2E''$ and $\tilde{B}\ ^2E'$ lie 0.01306 Hartree (= 2866 cm^{-1}) and 0.06454 Hartree (= 14170 cm^{-1}), respectively, above the ground electronic state $\tilde{X}\ ^2A_2'$ [46].

Recent spectroscopic study of NO_3 has been carried out for several decades. Nelson *et al.*, Ishiwata *et al.*, and Kim *et al.* independently reported dispersed fluorescence spectra following the optical excitation to the $\tilde{B}\ ^2E'$ state [47-49]. These three groups observed almost the same fluorescence spectra; however, they arrived at different conclusions about the molecular geometrical structure; Nelson *et al.* concluded the molecular structure as C_{2v}, whereas Ishiwata *et al.* concluded the D_{3h} structure. Kim *et al.* interpreted the experimental

result as following; the potential energy surface has D_{3h} symmetry with three shallow minima, which correspond to the local C_{2v} structure, but on the time scale of molecular rotations the averaged vibrations around these three minima lead to the D_{3h} structure. Stanton *et al.* also pointed out the non-rigidity of the potential energy surface [50]. Ishiwata *et al.* determined the three fundamental vibrational frequencies in the ground electronic state of $^{14}NO_3$ to be ν_1 (a_1', symmetric N-O stretch) = 1060 cm^{-1}, ν_3 (e', degenerate asymmetric N-O stretch) = 1480 cm^{-1}, and ν_4 (e', degenerate ONO deformation) = 380 cm^{-1}, under the D_{3h} molecular structure consideration [48]. Friedl and Sander identified the remaining ν_2 mode (a_2", out of plane bending) at 762.327 cm^{-1} [51]. Figure 1-1 schematically shows these four normal vibrational modes of NO_3. The first high-resolution spectroscopy of NO_3 was carried out for the 1480 cm^{-1} band using the infrared diode laser by Ishiwata, Kawaguchi and co-workers [52,53]. They clarified that the upper state of this 1480 cm^{-1} band has the E' symmetry, the band origin is located at 1492 cm^{-1}, and the molecule takes a regular triangle structure of D_{3h} symmetry in the ground electronic state. Simultaneously, they recognized some anomalies in this 1492 cm^{-1} band. Especially, it is strange and interesting that the upper E' symmetry state needs the small but not negligible effective spin-orbit interaction terms for the rotational analysis, though the ground $\tilde{X}\,^2A_2$' state originally has no electronic orbital angular momentum. Hirota *et al.* discussed that these anomalies in the upper state result from the vibronic interactions between the $\tilde{X}\,^2A_2$' state and the $\tilde{B}\,^2E$' state through the e' symmetry vibrational modes [54,55].

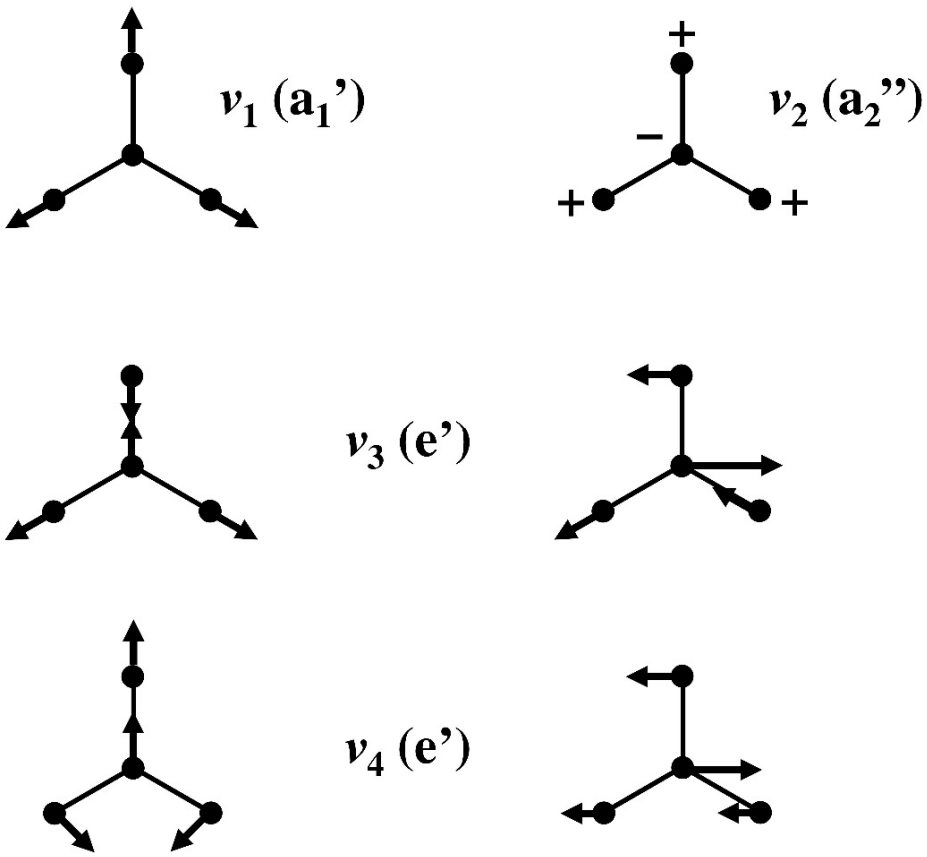

Figure 1-1. Vibrational modes of NO_3 in D_{3h} geometry.

After that, many vibration-rotation spectra in the infrared region up to 3000 cm^{-1} have been observed and analyzed [56-58]. As mentioned above the vibrational assignment in the ground electronic state has been carried out experimentally; however, recently Stanton and his co-workers proposed another vibrational assignment by theoretical calculation [59-61]. This proposal claims that the ν_3 frequency is about 1100 cm^{-1}, and the 1492 cm^{-1} band should be assigned as the $\nu_3 + \nu_4$ combination band. Stanton *et al.* tried to explain the anomalous ν_4 progressions in the photoelectron spectrum of NO_3^- anion reported by Weaver *et al.* [62], in

terms of the vibronic coupling, where Stanton employed an *ab initio* potential energy surface developed by Köppel *et al* [63]. Several other groups also predicted the lower v_3 frequency [64-66]. Just for reference, I list here the frequencies of normal vibrational modes of NO_3^- anion as following: v_1 = 1050 cm^{-1}, v_2 = 831 cm^{-1}, v_3 = 1390 cm^{-1}, and v_4 = 720 cm^{-1} in solution [67,68] and v_3 = 1356.2 cm^{-1} for $^{14}N^{16}O_3^-$ isotopologue in neon matrix [69], which are closer to the frequencies of the traditional vibrational assignment comparing to the new proposal. However, I do not intend to judge which vibrational assignment is correct. In the wake of the proposal for the vibrational assignment, several groups have carried out the detailed spectroscopic studies including the hot bands and the combination bands in neon matrix [70,71] and in a gas phase [72-75], focusing on the $^{14/15}N$ and $^{16/18}O$ vibrational isotope shifts, the symmetry lowering from D_{3h} to C_{2v}, and the perturbation analysis. If the experimental vibrational assignment is correct the ratio of the normal mode frequencies is almost $v_4 : v_2 : v_1 : v_3 = 1 : 2 : 3 : 4$, whereas the theoretical vibrational assignment leads to the frequency ratio of $v_4 : v_2 : v_1 : v_3 = 1 : 2 : 3 : 3$. Either way, the closely-lying vibrational excited states, which include the combination bands and the overtones, may end up with the strong Fermi resonances and the complicated inter-vibrational states interactions. In spite of the deceptively simple molecular structure consisting of only four light atoms, the ground electronic state of NO_3 radical is still a challenging subject for both experimentalists and theoreticians.

The first excited electronic state $\tilde{A}\,^2E''$ is now known to be located about 7060 cm^{-1}

above the $\tilde{X}\,^2A_2$' state. Weaver *et al.* reported the first observation of this $\tilde{A}\,^2E$" state by the photoelectron spectroscopy of NO_3^- anion [62]. Before this identification of the $\tilde{A}\,^2E$" state, some scientists thought that the 1492 cm^{-1} band which is now assigned to the vibrational transition in the $\tilde{X}\,^2A_2$' state was possible to be assigned to the $\tilde{A}\,^2E" \leftarrow \tilde{X}\,^2A_2$' electronic transition. Kim *et al.* carried out *ab initio* calculations for the low-lying electronic states of NO_3, and their highest level calculation predicted that the vertical $\tilde{A}\,^2E" - \tilde{X}\,^2A_2$' energy separation was about 3600 cm^{-1} [76]. The $\tilde{A}\,^2E" \leftarrow \tilde{X}\,^2A_2$' transition is originally optically forbidden; however, for several decades the high-resolution spectra of this electronic transition have been reported. Hirota *et al.* reported the first high-resolution spectroscopic study of this electronic transition in the 7602 cm^{-1} region, where the vibronically allowed $^2A_1" - {}^2A_2$' component of the 4^1_0 band in the $\tilde{A}\,^2E" \leftarrow \tilde{X}\,^2A_2$' electronic transition exists [77]. The spectroscopic study of NO_3 in the near infrared region is under progress using the cavity ring down spectroscopy, which is one of the high sensitive spectroscopic methods, by Okumura and his co-workers [78-81]. Jacox and Thompson reported the absorption spectrum of the $\tilde{A} - \tilde{X}$ transition ranging 7000 – 10000 cm^{-1} [82]. These groups obtained the evidence for the significant Jahn-Teller interaction. The static and dynamic Jahn-Teller coupling in this $\tilde{A}\,^2E"$ state has been analyzed theoretically [83,84]. Symmetrically speaking the $a_2"$ symmetry vibrational modes are able to mediate the vibronic coupling between the $\tilde{A}\,^2E"$ state and the $\tilde{B}\,^2E$' state, and the appearance of the dark $\tilde{A}\,^2E"$ state can be expressed to be due to the

intensity borrowing from the optically allowed $\tilde{B}$ – $\tilde{X}$ electronic transition.

As discussed above, the massive vibronic coupling among the low-lying electronic states $\tilde{X}$ $^2A_2$', $\tilde{A}$ ^{2}E", and $\tilde{B}$ ^{2}E' should be taken into account for the appropriate understanding of the high-resolution spectra of NO_3. Simultaneously, the vibronic coupling among these electronic states was found to be important for the photolysis pathways of NO_3 such as the roaming mechanism [85-94]. Therefore, the detailed investigation of the $\tilde{B}$ ^{2}E' state is desired to understand the intra-molecular interactions in NO_3.

The second excited electronic state $\tilde{B}$ ^{2}E' is located about 15100 cm^{-1} above the $\tilde{X}$ $^2A_2$' state. The low-resolution absorption spectra and laser induced fluorescence spectra of the $\tilde{B}$ – $\tilde{X}$ transition have been reported by many groups [47,48,95-103]. Ramsay photographed the NO_3 absorption spectrum for 665 – 500 nm region [95]. He recognized the vibronic bands progression with about 940 cm^{-1} spacing, whose vibronic bands wavenumbers are 15093 cm^{-1}, 16043 cm^{-1}, 16969 cm^{-1}, and 17890 cm^{-1}, and tentatively assigned them as the 0^0_0, 1^1_0, 1^2_0, and 1^3_0 bands, respectively. The first high-resolution spectroscopic study of the $\tilde{B}$ – $\tilde{X}$ transition was reported by Carter *et al.* in jet-cooled condition, in 1996 [104]. They observed the fluorescence excitation spectrum in high-resolution of about 200 MHz at low rotational temperature of about 20 K; however, the observed spectrum was broad and unstructured. However they also applied the Zeeman beat measurement to this electronic transition, a detailed analysis could not be successfully carried out because of the complexity

of the observed spectrum. Therefore, the $\tilde{B}\,^2$E' state of NO_3 is still remained to be far from well understood, and we have a very limited understanding of the vibronic coupling including this $\tilde{B}\,^2$E' state.

1.4. Aim of this study and composition of doctoral dissertation

Again, this doctoral dissertation treats only one small polyatomic radical NO_3. However, this radical is of consequence for the development of molecular science. As described in the previous section, the various spectroscopic studies have revealed that the real molecular properties of NO_3 are fully beyond the Born-Oppenheimer approximation. These experimental results of NO_3 suggest that the breakdown of the Born-Oppenheimer approximation might cause serious misunderstanding of the real molecular nature. Then, it is believed that the detailed spectroscopic study of NO_3 is one of the keys to create *new* molecular theory beyond the Born-Oppenheimer approximation.

The present study aimed at obtaining more detailed information about the remaining $\tilde{B}\,^2$E' electronic state of NO_3 radical than before, and also aimed at understanding the intra-molecular interactions including the $\tilde{B}\,^2$E' state. Then, high-resolution laser spectroscopic method and the Zeeman effect observation have been applied to the 0 – 0 band of the $\tilde{B}\,^2$E' ← $\tilde{X}\,^2A_2$' electronic transition of $^{14}NO_3$ and $^{15}NO_3$ isotopologues. The present study provides

the new knowledge about the $\tilde{B}\,^2$E' state through the detailed analysis of the observed spectra. Simultaneously, the present study demonstrates that we are able to analyze the high-resolution spectrum even if it is massively complicated, by the combination of the detailed experiments under high-resolution and high-accurate condition, and the appropriate quantum mechanical treatments. I believe that the present study is an important step forward in molecular spectroscopy and molecular science, which might lead us to the new ground in the field of molecular science in the future.

In this Chapter 1, the brief introductions about the Born-Oppenheimer approximation, molecular rotations and vibrations, high-resolution laser spectroscopy and free radicals were given. Then, the numerous NO_3 experimental and theoretical studies were introduced to describe the current situation of this free radical, from mainly the point of views of molecular science and molecular spectroscopy.

In Chapter 2, theoretical treatments of NO_3 radical will be given. The quantum chemistry calculations of the low-lying electronic states, the basis functions and the rovibronic energy representation including the nuclear spin statistics, the Zeeman interaction, the selection rules and the transition probabilities, the perturbation theory and the intensity borrowing mechanism, and several examples of linewidth, will be described.

In Chapter 3, the principles of experiments and the setup of high-resolution laser spectroscopy of this study will be described. The generation methods of NO_3 radical, the

molecular beam method and the light source with a narrow energy width which are indispensable for high-resolution laser spectroscopy, the Zeeman effect observation using electromagnets, the absolute wavenumber calibration procedures, and high-resolution spectroscopy of NO_2 radical will be given.

In Chapter 4, rotationally-resolved high-resolution laser spectroscopy and the Zeeman effect observation of $^{14}NO_3$ radical will be reported. The observed spectra were massively complicated; however, it was demonstrated that the Zeeman splitting under the high-resolution and high-accurate condition is quite useful for the unambiguous rotational assignment. This is the first study that the rotational assignment of the NO_3 $\tilde{B}\,^2E' \leftarrow \tilde{X}\,^2A_2'$ system was successfully carried out. Based on the density of the experimentally identified vibronic states, the intra-molecular interactions of NO_3 radical will be discussed.

In Chapter 5, rotationally-resolved high-resolution laser spectroscopy and the Zeeman effect observation of $^{15}NO_3$ isotopologue will be reported. This is the first high-resolution spectroscopic study of the electronic transition of this isotopologue. The observed $^{15}NO_3$ spectrum was found to be much simpler than the $^{14}NO_3$ spectrum, and the rotational branch structures were identified. The Zeeman effect observation was useful for the obvious rotational assignment, and the molecular constants of the $\tilde{B}\,^2E'$ state were estimated.

Chapter 2. Theoretical treatment

2.1. Quantum chemistry calculation

Table 2-1 lists the results of quantum chemistry calculations of NO_3 radical with the Gaussian 03 program [105] by using *ab initio* calculation and the density functional theory (DFT) calculation with several basis sets, under the fixed molecular geometrical structure of D_{3h} symmetry with the N-O bond length of 1.2378 Å. This structure was estimated from the recent high-resolution spectroscopic study in the infrared region [74]. Unfortunately, all listed results using the unrestricted configuration-interaction singles (UCIS) excited states calculation are not consistent both qualitatively and quantitatively with the experimental result concerning the low-lying electronic states; the calculations expect the first excited electronic state is a bright E' state and the second is a dark E" state. On the other hand, the DFT calculation with the unrestricted B3LYP (UB3LYP) method provided the reasonable results which are somewhat consistent with the experimental results. Here, I do not intend to judge which calculation is better for NO_3 radical. Based on these quantum chemistry calculations, what I would like to emphasize here are the following two points.

1. There are four excited electronic states, which are actually two doubly-degenerate excited electronic states, within 2 eV above the ground electronic state.

Table 2-1. Comparison of the energies of the excited electronic states between the quantum chemistry calculations and the experiments. The irreducible representations in D_{3h} point group are written in the parentheses. The energies of the excited electronic states are in units of electron-Volt.

	Doublet excited electronic state			
method	$\tilde{A}$ state	$\tilde{B}$ state	$\tilde{C}$ state	$\tilde{D}$ state
***Ab initio* calculation**				
UCIS/6-31G	0.113 (E')	0.715 (E")	3.181 (E")	4.915 (E')
UCIS/6-31G(df)	0.463 (E')	1.142 (E")	3.896 (E")	5.644 (E')
UCIS/6-31G(2df)	0.497 (E')	1.185 (E")	3.933 (E")	5.659 (E')
UCIS/6-31G(3df)	0.574 (E')	1.252 (E")	3.964 (E")	5.670 (E')
UCIS/6-31++G	0.189 (E')	0.775 (E")	3.119 (E")	4.878 (E')
UCIS/6-31++G(df)	0.576 (E')	1.225 (E")	3.859 (E")	5.604 (E')
UCIS/6-31++G(3df)	0.616 (E')	1.278 (E")	3.911 (E")	5.627 (E')
UCIS/cc-pVQZ	0.579 (E')	1.263 (E")	3.892 (E")	5.628 (E')
UCIS/aug-cc-pVQZ	0.596 (E')	1.276 (E")	3.878 (E")	5.615 (E')
DFT calculation				
UB3LYP/STO-3G	0.895 (E")	1.187 (E')	3.902 (E')	4.117 (E")
UB3LYP/3-21G	1.207 (E")	1.742 (E')	4.448 (E')	4.892 (E")
UB3LYP/3-21+G	1.263 (E")	1.818 (E')	4.434 (E')	4.871 (A_1")
UB3LYP/6-31G	1.227 (E")	1.793 (E')	4.389 (E')	4.868 (E")
UB3LYP/6-311G	1.230 (E")	1.781 (E')	4.368 (E')	4.832 (E")
UB3LYP/6-31++G	1.234 (E")	1.787 (E')	4.330 (E')	4.796 (E")
UB3LYP/6-31++G(3df)	1.449 (E")	1.971 (E')	4.806 (E')	5.117 (A_1")
UB3LYP/cc-pVQZ	1.444 (E")	1.961 (E')	4.803 (E')	5.127 (A_1")
Experimental	0.875 (E")[a]	1.872 (E')[b]	3.690 (?)[c]	

[a] Ref. 62 (Photo-electron spectroscopy). [b] Ref. 95 (Absorption spectroscopy).

[c] Ref. 106. This experimental result was obtained from absorption spectroscopy in a condensed phase. Then, this energy may be different from that in a gas phase.

2. The other excited electronic states lie in higher energy region such as ultraviolet or vacuum ultraviolet.

From these two points, the excited electronic states excluding the low-lying $\tilde{X}\,^2A_2$', $\tilde{A}\,^2E$", and $\tilde{B}\,^2E$' states are not important to discuss the $\tilde{B}\,^2E$' state of NO_3 radical, because these higher excited electronic states are so far from the $\tilde{B}\,^2E$' state that the vibronic coupling between those states and the $\tilde{B}\,^2E$' state should not be dominant and might be ignored. Therefore, now we can focus our attention only on the three low-lying electronic states $\tilde{X}\,^2A_2$', $\tilde{A}\,^2E$", and $\tilde{B}\,^2E$' to deal with the intra-molecular interactions of NO_3 radical.

2.2. Rovibronic energy structure

Angular momenta

To describe the rovibronic energy structure of NO_3 radical, angular momenta and their projections were defined as the following (in this doctoral dissertation, vectors and tensors are written in Roman bold letters, whereas scalars in Italic unbold letters):

R the molecular rotation angular momentum.

L the electronic orbital angular momentum.

S the electronic spin angular momentum.

J the total angular momentum (**J** = **R** + **L** + **S**).

N the total angular momentum excluding the electronic spin (**N** = **J** – **S**).

Λ the projection of **L** along the molecular fixed *z* axis.

Σ the projection of **S** along the molecular fixed *z* axis.

P the projection of **J** along the molecular fixed *z* axis.

k the projection of **N** along the molecular fixed *z* axis ($k = P - \Sigma$).

M_L the projection of **L** along the space fixed *Z* axis.

M_S the projection of **S** along the space fixed *Z* axis.

M_J the projection of **J** along the space fixed *Z* axis.

M_N the projection of **N** along the space fixed *Z* axis.

These angular momenta and their projections are schematically shown in Figure 2-1. Note that the quantum numbers J, Σ, P, M_S and M_J are half-integers, while the other quantum numbers R, L, N, k, Λ, M_L and M_N are integers, when molecules in question have the electronic spin $S = 1/2$ such as NO_3 radical.

The $\tilde{B}\,^2$E' state of NO_3

Under the Born-Oppenheimer approximation, the basis functions for the rotating molecules in certain vibronic states are generally able to be described in Hund's coupling case

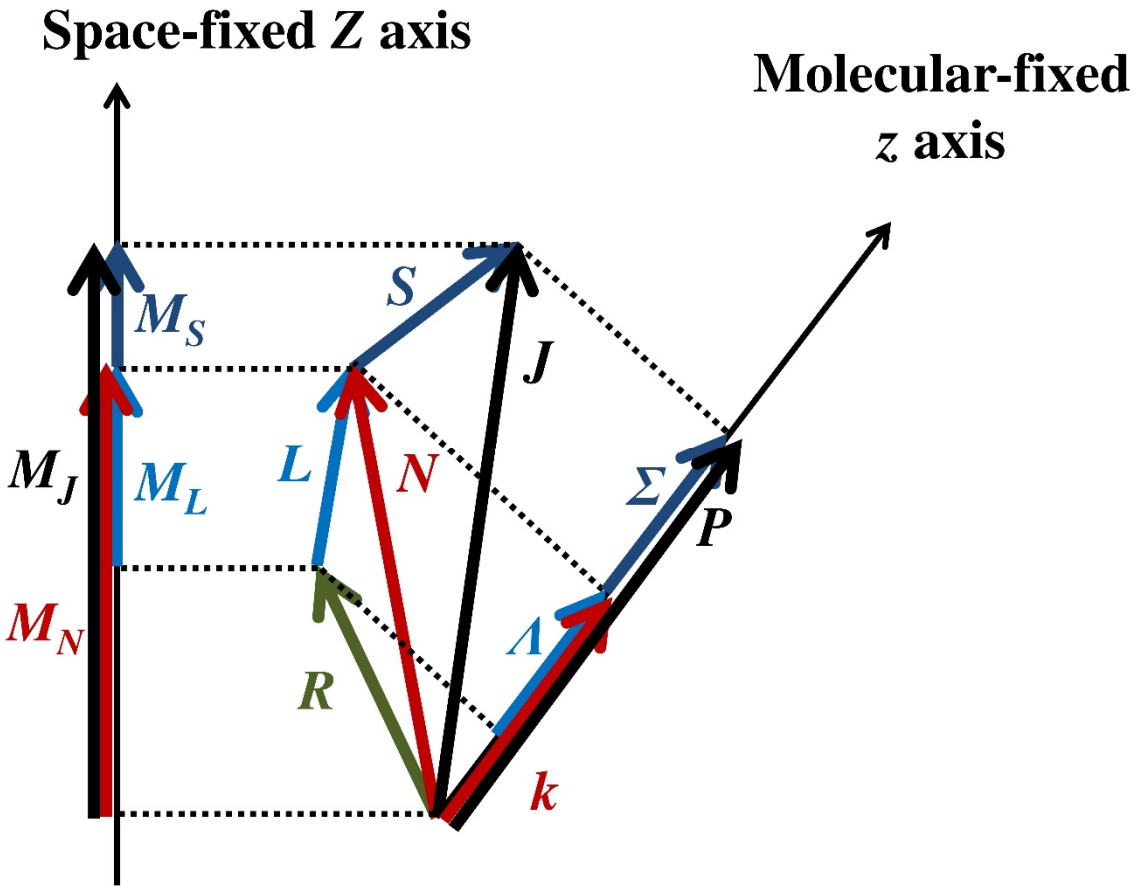

Figure 2-1. The definition of angular momenta and their projections.

(a), as the product of the ket vectors of the electronic orbital part $|\Lambda\rangle$, the electronic spin part $|S,\Sigma\rangle$, the molecular vibrational part $|v\rangle$, and the rotational part of a symmetric top molecule $|J,P,M_J\rangle$:

$$|\Lambda\rangle|S,\Sigma\rangle|v\rangle|J,P,M_J\rangle. \qquad (2\text{-}1)$$

The $\tilde{B}\,^2$E' (v = 0) state of NO_3 radical was found to be described well by Hund's coupling case (a) from this work, as later mentioned in Chapter 4. In the limit of Hund's

coupling case (a), the significant spin-orbit interaction splits the $\tilde{B}\,^2\mathrm{E}'$ state into the $^2\mathrm{E}'_{3/2}$ and the $^2\mathrm{E}'_{1/2}$ spin-orbit components. Under the assumption of the D_{3h} molecular structure, the symmetry-adapted linear combination (SALC) for the $^2\mathrm{E}'_{3/2}$ spin-orbit component can be written as

$$\begin{aligned}&\left|\tilde{B}^2\mathrm{E}'_{3/2}\,(v=0), J, P, \Sigma=+0.5, M_J\right\rangle \\ &=\frac{1}{\sqrt{2}}\left[\left|+1\right\rangle\left|0.5,+0.5\right\rangle\left|0\right\rangle\left|J, P, M_J\right\rangle+(-)^{J-P}\left|-1\right\rangle\left|0.5,-0.5\right\rangle\left|0\right\rangle\left|J,-P, M_J\right\rangle\right]\end{aligned} \tag{2-2}$$

and that for the $^2\mathrm{E}'_{1/2}$ spin-orbit component can be written as

$$\begin{aligned}&\left|\tilde{B}^2\mathrm{E}'_{1/2}\,(v=0), J, P, \Sigma=-0.5, M_J\right\rangle \\ &=\frac{1}{\sqrt{2}}\left[\left|+1\right\rangle\left|0.5,-0.5\right\rangle\left|0\right\rangle\left|J,-P, M_J\right\rangle+(-)^{J+P+1}\left|-1\right\rangle\left|0.5,+0.5\right\rangle\left|0\right\rangle\left|J, P, M_J\right\rangle\right].\end{aligned} \tag{2-3}$$

The rotational energy structure of each spin-orbit component can be expressed in the similar way with that of the singlet state as

$$E_{J,P}=T_0+BJ(J+1)+(C-B)P^2-D_J J^2(J+1)^2-D_{JP}J(J+1)P^2-D_P P^4, \tag{2-4}$$

by ignoring the small interaction terms and substituting K of the singlet molecule into P. Here T_0 is the vibronic energy, B and C are the rotational constants, and D_J, D_{JP} and D_P are the first-order centrifugal distortion constants.

The energy separation between the spin-orbit components can be calculated by introducing the spin-orbit interaction Hamiltonian:

$$\hat{H}_{SO}=A_{SO}\hat{\mathbf{L}}\cdot\hat{\mathbf{S}}, \tag{2-5}$$

where A_{SO} is the spin-orbit interaction constant. The diagonal matrix element of the spin-

orbit interaction is

$$\left\langle \Sigma \left| \left\langle \Lambda \left| \hat{H}_{\mathrm{SO}} \right| \Lambda \right\rangle \right| \Sigma \right\rangle = A_{\mathrm{SO}} \zeta_e d\Sigma = A_{\mathrm{SO}}^{\mathrm{eff}} \Sigma \,, \tag{2-6}$$

where ζ_e is the electronic Coriolis interaction constant, and d is Child and Longuet-Higgins' vibronic coupling parameter which represents the degree of quenching of angular momentum by the Jahn-Teller effect. The product $\zeta_e d$ represents the effective value of $\left\langle \Lambda \left| \hat{L}_z \right| \Lambda \right\rangle$, whose value is less than unity in magnitude, because the molecular axial component of **L** is often partly quenched in a symmetric top molecule with a C_3 axis [107,108]. This $\zeta_e d$ value reduces the *original* spin-orbit interaction constant to the *effective* spin-orbit interaction constant represented by $A_{\mathrm{SO}}^{\mathrm{eff}}$ in Equation (2-6). In conclusion, the rotational structure of the $\tilde{B}\,^2$E' (υ = 0) state including the spin-orbit interaction can be written as

$$\begin{aligned} E_{J,P} &= T_0 + A_{\mathrm{SO}} \zeta_e d\Sigma \\ &+ BJ(J+1) + (C-B)P^2 - D_J J^2 (J+1)^2 - D_{JP} J(J+1) P^2 - D_P P^4 \end{aligned} \tag{2-7}$$

The $\tilde{X}\,^2\mathrm{A}_2$' state of NO_3

When the spin-orbit interaction is zero or negligibly small in magnitude, the basis functions of symmetric top molecules can be described by Hund's coupling case (b) basis $\left| N, k, S, J, M_J \right\rangle$, where N and k become the good quantum numbers. The basis functions of Hund's coupling case (a) and Hund's coupling case (b) may be transformed to each other by the following relationship

$$\left| N,k,S,J,M_J \right\rangle = \sqrt{2N+1}\sum_P \sum_\Sigma (-)^{N-S+P} \begin{pmatrix} N & S & J \\ k & \Sigma & -P \end{pmatrix} \left| S,\Sigma \right\rangle \left| J,P,M_J \right\rangle . \qquad (2\text{-}8)$$

Here the parentheses with 2 × 3 matrix denote the Wigner 3-j symbols whose explicit form can be written as [109]

$$\begin{pmatrix} a & b & c \\ \alpha & \beta & \gamma \end{pmatrix} = \delta_{\alpha+\beta+\gamma,0} \sqrt{\frac{(a+b-c)!(a+c-b)!(b+c-a)!}{(a+b+c+1)!}} \times \sum_t \frac{(-)^{c-\gamma+t} \sqrt{(a+\alpha)!(a-\alpha)!(b+\beta)!(b-\beta)!(c+\gamma)!(c-\gamma)!}}{t!(a+b-c-t)!(a-\alpha-t)!(b+\beta-t)!(c-b+\alpha+t)!(c-a-\beta+t)!}. \qquad (2\text{-}9)$$

The sum is taken over all values of *t* which lead to non-negative factorials. The Kronecker's delta $\delta_{\alpha+\beta+\gamma,0}$ in Equation (2-9) indicates that the Wigner 3-j symbols survive when the condition $\alpha + \beta + \gamma = 0$ is satisfied. Hereafter I call this condition the closure relationship of the Wigner 3-j symbol.

In Hund's coupling case (b) limit, each *N* level splits into (2*S* + 1) spin components by the spin-rotation interaction. The $\tilde{X}\,^2\mathrm{A}_2'$ ($v = 0$) state of NO_3 is known to be described by Hund's coupling case (b) [51-53,56-58,72-75,77]. Then, in this case, because of the electronic spin *S* of 1/2, each *N* level splits into two F_1 and F_2 spin components whose total angular momenta are $J = N + 0.5$ and $J = N - 0.5$, respectively. SALC for the F_1 spin component can be written as

$$\begin{aligned} &\left| \tilde{X}\,^2\mathrm{A}_2'(v=0), N, k, J = N+0.5, M_J \right\rangle \\ &= \sqrt{\frac{N+k+1}{2N+2}} \left| 0 \right\rangle \left| 0.5,+0.5 \right\rangle \left| 0 \right\rangle \left| J, k+0.5, M_J \right\rangle \\ &+ \sqrt{\frac{N-k+1}{2N+2}} \left| 0 \right\rangle \left| 0.5,-0.5 \right\rangle \left| 0 \right\rangle \left| J, k-0.5, M_J \right\rangle \end{aligned} \qquad (2\text{-}10)$$

and that for the F_2 spin component can be written as

$$\begin{aligned}&\left|\tilde{X}^2\mathrm{A}_2'(v=0),N,k,J=N-0.5,M_J\right\rangle\\&=-\sqrt{\frac{N-k}{2N}}\left|0\right\rangle\left|0.5,+0.5\right\rangle\left|0\right\rangle\left|J,k+0.5,M_J\right\rangle\\&+\sqrt{\frac{N+k}{2N}}\left|0\right\rangle\left|0.5,-0.5\right\rangle\left|0\right\rangle\left|J,k-0.5,M_J\right\rangle.\end{aligned} \tag{2-11}$$

The rotational energy structure in Hund's coupling case (b) is calculated by diagonalization of the Hamiltonian matrix whose total Hamiltonian consists of the rotational Hamiltonian with the first-order centrifugal distortion correction and the spin-rotation interaction Hamiltonian:

$$\begin{aligned}\hat{H}&=\hat{H}_{\mathrm{ROT}}+\hat{H}_{\mathrm{SR}}\\&=B\hat{\mathbf{N}}^2+(C-B)\hat{N}_z^2-D_N\hat{\mathbf{N}}^4-D_{NK}\hat{\mathbf{N}}^2\hat{N}_z^2-D_K\hat{N}_z^4+\boldsymbol{\varepsilon}\cdot\hat{\mathbf{N}}\cdot\hat{\mathbf{S}},\end{aligned} \tag{2-12}$$

where D_N, D_{NK}, and D_K are the first-order centrifugal distortion constants, and $\boldsymbol{\varepsilon}$ is the spin-rotation interaction tensor.

Based upon the theory of angular momentum with the spherical tensor operators, the non-zero matrix elements are given by

$$\left\langle N,k\left|\hat{H}_{\mathrm{ROT}}\right|N,k\right\rangle=BN(N+1)+(C-B)k^2-D_NN^2(N+1)^2-D_{NK}N(N+1)k^2-D_Kk^4, \tag{2-13}$$

$$\begin{aligned}&\left\langle N,k,S,J\left|\hat{H}_{\mathrm{SR}}\right|N,k,S,J\right\rangle\\&=\left[\varepsilon_{bb}-\frac{(\varepsilon_{bb}-\varepsilon_{cc})k^2}{N(N+1)}\right]\frac{J(J+1)-N(N+1)-S(S+1)}{2},\end{aligned} \tag{2-14}$$

$$\left\langle N-1,k,S,J\left|\hat{H}_{\mathrm{SR}}\right|N,k,S,J\right\rangle=\frac{(\varepsilon_{bb}-\varepsilon_{cc})k\sqrt{N^2-k^2}}{2N}. \tag{2-15}$$

Here ε_{bb} and ε_{cc} are the *b* and *c* axial components, respectively, of the spin-rotation interaction tensor.

Nuclear spin statistics

Supposing that NO_3 radical has the regular triangle structure with D_{3h} symmetry and all oxygen atoms are ^{16}O atomic isotope, three ^{16}O nuclei are equivalent; therefore, we have to consider the nuclear spin statistics of each rotational level. Because ^{16}O nucleus is boson, which has null nuclear spin, this nucleus obeys the Bose-Einstein statistics: the total wavefunction of NO_3 must not change its sign for interchanging three equivalent ^{16}O nuclei.

Under the Born-Oppenheimer approximation, the irreducible representation of the total wavefunction of molecules can be factored into the product of the representations of the electronic wavefunction, the vibrational wavefunction, the rotational wavefunction, and the nuclear spin wavefunction. The Bose-Einstein statistics requests that the irreducible representation of the total wavefunction includes the totally symmetric representation. In the case of the D_{3h} point group it is A_1'. When we consider the vibrational ground state, we do not need to take the vibrational wavefunction into account, because the representation of the vibrational wavefunction is A_1'. Moreover in the case of NO_3 in D_{3h}, the nuclear spin wavefunction also is not needed, because the nitrogen nucleus lies at the center of mass and the representation of the nuclear spin wavefunction is also A_1'.

In case of the $\tilde{X}\ ^2A_2$' ($\upsilon = 0$) state, only the rotational levels with A_2' representation survive. Therefore, only $k = 0, \pm3, \pm6 \ldots$ stacks are allowed to be existed, and only odd N

levels survive in the $k = 0$ stack. On the other hand in case of $\tilde{B}\,^2$E' ($v = 0$) state, only the rotational levels with E' representation survive. Then only $k = \ldots -5, -2, +1, +4 \ldots$ stacks are allowed to be existed. These k stacks correspond to $P = \ldots -4.5, -1.5, +1.5, +4.5 \ldots$ for the $^2E'_{3/2}$ spin-orbit component, and $P = \ldots -5.5, -2.5, +0.5, +3.5 \ldots$ for the $^2E'_{1/2}$ spin-orbit component, because of the relationship $k = P - \Sigma$.

2.3. The Zeeman effect

The Hamiltonian of the Zeeman interaction in the molecule with the electronic spin and electronic orbital angular momenta can be written as

$$\hat{H}_Z = g_S \mu_B \mathbf{H} \cdot \mathbf{S} + g_L \mu_B \mathbf{H} \cdot \mathbf{L}\,, \tag{2-16}$$

where g_S is the electron spin g-factor, g_L is the electron orbital g-factor, μ_B (= 4.66864×10^{-5} G^{-1} cm^{-1}) is the Bohr magneton, and **H** is the external magnetic field vector. For the $\tilde{X}\,^2A_2$' state, the second term of Equation (2-16) vanishes because the $\tilde{X}$ state does not have the electronic orbital angular momentum. On the other hand for the $\tilde{B}\,^2$E' state, the second term of Equation (2-16) does not vanish.

The first-order non-zero matrix elements of the Zeeman interaction for the $\tilde{X}\,^2A_2$' state can be derived as [110]

$$\begin{aligned}&\left\langle N,k,S,J',M_J\left|\hat{H}_Z\right|N,k,S,J,M_J\right\rangle \\ &= g_S\mu_B H(-)^{J'-M_J+S+N+J+1}\sqrt{(2J'+1)(2J+1)S(S+1)(2S+1)} \\ &\times\begin{Bmatrix}S & J' & N\\ J & S & 1\end{Bmatrix}\begin{pmatrix}J' & 1 & J\\ -M_J & 0 & M_J\end{pmatrix},\end{aligned} \tag{2-17}$$

where H indicates the magnetic field strength: $H = |\mathbf{H}|$. The curly braces with 2 × 3 matrix denote the Wigner 6-j symbols, whose explicit form is given by Equations (36) and (37) in Ref. 109. The Hamiltonian matrix of the Zeeman interaction can be solved analytically, and the solutions are given by

$$\begin{aligned}E &= E_{\mathrm{ROT}} - \frac{1}{4}\left[\varepsilon_{bb} - \frac{(\varepsilon_{bb}-\varepsilon_{cc})k^2}{N(N+1)}\right] \\ &\pm\frac{1}{2}\sqrt{\left(N+\frac{1}{2}\right)^2\left[\varepsilon_{bb} - \frac{(\varepsilon_{bb}-\varepsilon_{cc})k^2}{N(N+1)}\right]^2 + 2g_S\mu_B HM_J\left[\varepsilon_{bb} - \frac{(\varepsilon_{bb}-\varepsilon_{cc})k^2}{N(N+1)}\right] + (g_S\mu_B H)^2}\end{aligned} \tag{2-18}$$

for the levels with $|M_J| < (N + 1/2)$, and

$$E = E_{\mathrm{ROT}} + \frac{N}{2}\left[\varepsilon_{bb} - \frac{(\varepsilon_{bb}-\varepsilon_{cc})k^2}{N(N+1)}\right] \pm \frac{1}{2}g_S\mu_B H \tag{2-19}$$

for the levels with $M_J = \pm (N + 1/2)$. Here, E_{ROT} is the rotational energy given by Equation (2-13), excluding the spin-rotation interaction. Equations (2-18) and (2-19) are exact when the off-diagonal matrix elements of the spin-rotation interaction vanish or are ignorable. In a relatively weak magnetic field, the M_J levels are separated approximately equally (so-called the anomalous Zeeman effect). In a stronger magnetic field, where the Zeeman splitting exceeds the spin-rotation splitting in magnitude, the rotational level N splits into $(2S + 1)$ levels by M_S, and then each M_S level splits into $(2N + 1)$ levels by M_N (the Paschen-Back limit). This

means that the electronic spin is almost decoupled from the molecular framework and M_N and M_S become the good quantum numbers; however, M_J is still remained as a good quantum number.

The first-order non-zero matrix elements of the Zeeman interaction for the ^{2}E'-type vibronic state can be derived as [111]

$$\begin{aligned}
&\left\langle J', P', \Sigma', M_J' \middle| \hat{H}_Z \middle| J, P, \Sigma, M_J \right\rangle \\
&= \mu_B H \delta_{M_J', M_J} \sum_q (-)^{J'-M_J'} \begin{pmatrix} J' & 1 & J \\ -M_J' & 0 & M_J \end{pmatrix} (-)^{J'-P'} \begin{pmatrix} J' & 1 & J \\ -P' & q & P \end{pmatrix} \\
&\times \sqrt{(2J'+1)(2J+1)} \\
&\times \left[g_L \zeta_e d \delta_{P',P} \delta_{\Sigma',\Sigma} + (-)^{S-\Sigma'} \begin{pmatrix} S & 1 & S \\ -\Sigma' & q & \Sigma \end{pmatrix} \sqrt{S(S+1)(2S+1)} \right].
\end{aligned} \tag{2-20}$$

In case of the $\tilde{B}\,^2$E' state of NO_3 radical, Equation (2-20) can be simplified as

$$\begin{aligned}
&\left\langle J', P, \Sigma = \pm 0.5, M_J \middle| \hat{H}_Z \middle| J, P, \Sigma = \pm 0.5, M_J \right\rangle \\
&= (-)^{2J'-M_J-P} \begin{pmatrix} J' & 1 & J \\ -M_J & 0 & M_J \end{pmatrix} \begin{pmatrix} J' & 1 & J \\ -P & 0 & P \end{pmatrix} \sqrt{(2J'+1)(2J+1)} \\
&\times \left(g_L \zeta_e d \pm \frac{g_S}{2} \right) \mu_B H \\
&= (-)^{2J'-M_J-P} \begin{pmatrix} J' & 1 & J \\ -M_J & 0 & M_J \end{pmatrix} \begin{pmatrix} J' & 1 & J \\ -P & 0 & P \end{pmatrix} \sqrt{(2J'+1)(2J+1)} g_{\text{eff}} \mu_B H,
\end{aligned} \tag{2-21}$$

because the terms with $q \neq 0$ vanish and/or are not important. I defined the effective *g*-factor of the ^{2}E' state as $g_{\text{eff}} = g_L\zeta_e d \pm g_S/2$, because $g_L\zeta_e d$ and g_S cannot be determined independently in this study. When we consider that the separation between the rotational levels with *J* and *J'* is large comparing to the Zeeman splitting and thus the terms with $J \neq J'$ are ignorable, the matrix element (2-21) becomes much simpler as

$$\begin{aligned}&\left\langle J,P,\Sigma=\pm0.5,M_J\left|\hat{H}_Z\right|J,P,\Sigma=\pm0.5,M_J\right\rangle\\&=(-)^{2J-M_J-P}\begin{pmatrix}J & 1 & J\\ -M_J & 0 & M_J\end{pmatrix}\begin{pmatrix}J & 1 & J\\ -P & 0 & P\end{pmatrix}(2J+1)g_{\text{eff}}\mu_B H\\&=\frac{M_J P}{J(J+1)}g_{\text{eff}}\mu_B H.\end{aligned} \tag{2-22}$$

In this case, M_J is always a good quantum number, and the separations among the Zeeman components are proportional to the magnetic field strength *H*.

2.4. Selection rules and transition probabilities

The spherical components of the space fixed coordinates **R** (*X*, *Y*, *Z*) and the molecular fixed coordinates **r** (*x*, *y*, *z*) may be defined as

$$R_{\pm1}=\mp\frac{1}{\sqrt{2}}(X\pm\mathrm{i}Y),\quad R_0=Z, \tag{2-23}$$

$$r_{\pm1}=\mp\frac{1}{\sqrt{2}}(x\pm\mathrm{i}y),\quad r_0=z. \tag{2-24}$$

The transformation between the space fixed coordinates and the molecular fixed coordinates can be expressed by using the rotation matrix $D^J_{M,N}$, as

$$R_\lambda=\sum_{t=0,\pm1}(-)^{\lambda-t}D^1_{-\lambda,-t}\,r_t, \tag{2-25}$$

$$r_t=\sum_{\lambda=0,\pm1}D^1_{\lambda,t}\,R_\lambda. \tag{2-26}$$

Here, the explicit form of the rotation matrix $D^J_{M,N}$ is given by [112]

$$\begin{aligned}D^J_{M,N}&=\exp\left[\mathrm{i}(M\psi+N\varphi)\right]\times\sum_r\frac{\sqrt{(J+M)!(J-M)!(J+N)!(J-N)!}}{(J-M-r)!(J+N-r)!r!(r+M-N)!}\\&\times\left(\cos\frac{\theta}{2}\right)^{2J-M+N-2r}\left(\sin\frac{\theta}{2}\right)^{2r+M-N},\end{aligned} \tag{2-27}$$

where ψ, θ, and φ are the Euler angles, and the sum is taken over all values of r which lead to non-negative factorials.

Then, the R_λ component of the electric dipole moment can be calculated as [113]

$$\begin{aligned}
&\left\langle \Lambda', S', \Sigma', v', J', P', M_J' \middle| \hat{\mu}_{R_\lambda} \middle| \Lambda'', S'', \Sigma'', v'', J'', P'', M_J'' \right\rangle \\
&= \sum_{t=0,\pm1} (-)^{\lambda - t} \left\langle v' \middle| \left\langle \Lambda' \middle| \hat{\mu}_{r_t} \middle| \Lambda'' \right\rangle \middle| v'' \right\rangle \left\langle S', \Sigma' \middle| S'', \Sigma'' \right\rangle \\
&\times \left\langle J', P', M_J' \middle| D^1_{-\lambda,-t} \middle| J'', P'', M_J'' \right\rangle \\
&= \sum_{t=0,\pm1} (-)^{\lambda - t + M'' - P''} \left\langle v' \middle| \left\langle \Lambda' \middle| \hat{\mu}_{r_t} \middle| \Lambda'' \right\rangle \middle| v'' \right\rangle \delta_{S',S''} \delta_{\Sigma',\Sigma''} \sqrt{(2J'+1)(2J''+1)} \\
&\times \begin{pmatrix} J'' & J' & 1 \\ -M_J'' & M_J' & -\lambda \end{pmatrix} \begin{pmatrix} J'' & J' & 1 \\ -P'' & P' & -t \end{pmatrix}.
\end{aligned} \tag{2-28}$$

Note that the quantum numbers of the upper state are labeled with primes, whereas the quantum numbers of the lower state are labeled with double primes, by following the tradition of molecular spectroscopy.

The space fixed coordinates are defined by an external magnetic field; the Z axis is selected to be parallel with the magnetic field vector, and the X and Y axes are selected to be perpendicular to the magnetic field vector. When we introduce a laser beam whose polarization is parallel with the magnetic field vector (the π-pump condition) onto molecular system, we set $\lambda = 0$. Then the selection rule $M_J' = M_J''$ (or $\Delta M_J = 0$) arises from the closure relationship of the Wigner 3-j symbol. On the other hand, when a laser beam whose polarization is perpendicular to the magnetic field vector falls onto molecules (the σ-pump condition), we set $\lambda = \pm 1$. Then the selection rule is $M_J' = M_J'' \pm 1$ (or $\Delta M_J = \pm 1$), because of the closure relationship of the Wigner 3-j symbol, again.

The $\langle v' | \langle \Lambda' | \hat{\mu}_{r_t} | \Lambda'' \rangle | v'' \rangle$ part also gives some selection rules. Under the Condon approximation, this vibronic part may be factored into the product of the vibrational part and the electronic orbital part: $\langle v' | v'' \rangle \langle \Lambda' | \hat{\mu}_{r_t} | \Lambda'' \rangle$. This factorization may not be a good approximation for NO_3 radical, because the degenerate normal modes with e' representation have the vibrational angular momentum which is mixed with the electronic orbital angular momentum to generate the effective angular momentum representing the degeneracy of the vibronic states. However, in case of the 0 – 0 band of the $\tilde{B}\ ^2\mathrm{E}' \leftarrow \tilde{X}\ ^2\mathrm{A}_2'$ transition of NO_3, this factorization may be reasonable, because there is no coupling between the vibrational angular momentum and the electronic orbital angular momentum, because of the zero vibrational angular momentum. The former vibrational part gives the Franck-Condon factor, and the latter electronic part gives the selection rules, i.e., the electronic orbital angular momentum must be changed by unity in magnitude during the optical transition in this case. Therefore we set $t = \pm 1$ in Equation (2-28). This means that this electronic transition should be a perpendicular transition, whose transition dipole moment is perpendicular to the molecular fixed *z* axis. From the closure relationship of the latter Wigner 3-j symbol in Equation (2-28), we obtain the selection rule $\Delta P = \pm 1$, and in case of the $\tilde{B}\ ^2\mathrm{E}' \leftarrow \tilde{X}\ ^2\mathrm{A}_2'$ transition of NO_3 this selection rule can be converted into $\Delta k = +1$. Under the condition $\Delta k = +1$, the Wigner 3-j symbol does not vanish only when $J' = J'' - 1$, J'', and $J'' + 1$. Then, we obtain the selection rule $\Delta J = 0, \pm 1$.

Table 2-2. Hönl-London factors as the functions of quantum numbers of the ground state.

Branch	F_1 spin component	F_2 spin component
$\tilde{B}\,^2E'_{1/2} \leftarrow \tilde{X}\,^2A_2'$ transition		
${}^rR_k(J)$	$\frac{(J-k+\frac{1}{2})(J+k+\frac{1}{2})(J+k+\frac{3}{2})}{6(J+1)(2J+1)^2}$	$\frac{(J+k+\frac{1}{2})^2(J+k+\frac{3}{2})}{6(J+1)(2J+1)^2}$
${}^rQ_k(J)$	$\frac{(J-k+\frac{1}{2})^2(J+k+\frac{1}{2})}{6J(J+1)(2J+1)}$	$\frac{(J-k+\frac{1}{2})(J+k+\frac{1}{2})^2}{6J(J+1)(2J+1)}$
${}^rP_k(J)$	$\frac{(J-k-\frac{1}{2})(J-k+\frac{1}{2})^2}{6J(2J+1)^2}$	$\frac{(J-k-\frac{1}{2})(J-k+\frac{1}{2})(J+k+\frac{1}{2})}{6J(2J+1)^2}$
$\tilde{B}\,^2E'_{3/2} \leftarrow \tilde{X}\,^2A_2'$ transition		
${}^rR_k(J)$	$\frac{(J+k-\frac{1}{2})(J+k+\frac{3}{2})(J+k+\frac{5}{2})}{6(J+1)(2J+1)^2}$	$\frac{(J-k+\frac{1}{2})(J+k+\frac{3}{2})(J+k+\frac{5}{2})}{6(J+1)(2J+1)^2}$
${}^rQ_k(J)$	$\frac{(J-k-\frac{1}{2})(J+k-\frac{1}{2})(J+k+\frac{3}{2})}{6J(J+1)(2J+1)}$	$\frac{(J-k-\frac{1}{2})(J-k+\frac{1}{2})(J+k+\frac{3}{2})}{6J(J+1)(2J+1)}$
${}^rP_k(J)$	$\frac{(J-k-\frac{3}{2})(J-k-\frac{1}{2})(J+k-\frac{1}{2})}{6J(2J+1)^2}$	$\frac{(J-k-\frac{3}{2})(J-k-\frac{1}{2})(J-k+\frac{1}{2})}{6J(2J+1)^2}$

In conclusion, the selection rules for the $\tilde{B}\,^2E' \leftarrow \tilde{X}\,^2A_2'$ transition of NO_3 are Δk = +1, ΔJ = 0, ±1, and ΔM_J = 0 for the π-pump condition or ΔM_J = ±1 for the σ-pump condition. Therefore, we observe only the ${}^rP$, ${}^rQ$, and ${}^rR$ branches, when we adopt the nomenclature ${}^{\Delta k}\Delta J$ for labeling the rotational lines of NO_3. When all of the selection rules mentioned above are satisfied, the rovibronic transition probabilities can be calculated as the product of the Franck-Condon factor and the Hönl-London factor, by using Equation (2-28) with the symmetry adapted basis sets, Equations (2-2), (2-3), (2-10), and (2-11). In this dissertation we are focusing only on the 0 – 0 band of the $\tilde{B}\,^2E' \leftarrow \tilde{X}\,^2A_2'$ transition of NO_3; therefore, there is

no need to take the Franck-Condon factor into account. The Hönl-London factors calculated by taking the sum over all possible values of M_J are tabulated in Table 2-2. The actual spectral line intensity is affected not only by the Hönl-London factor but also by the thermal distribution. Therefore, we can calculate the actual spectral line intensity by taking the product of the Hönl-London factor and the Boltzmann factor, under the assumption of the Maxwell-Boltzmann thermal distribution.

2.5. Perturbation

Eigenstates mixing

For the simplicity, we consider a two-level system. We suppose that two eigenstates $|1\rangle$ and $|2\rangle$ were orthonormal and their eigenvalues were E_1 and E_2 ($E_1 > E_2$) under the unperturbed condition. Therefore,

$$\hat{H}_0|i\rangle = E_i|i\rangle, \quad \langle i|j\rangle = \delta_{i,j}, \qquad (i, j = 1, 2) \tag{2-29}$$

where $\hat{H}_0$ is the zeroth-order Hamiltonian which has only diagonal matrix elements without any perturbation. Then, we now introduce a perturbation written by Hamiltonian $\hat{H}'$ which has only off-diagonal matrix elements. Then the secular equation we have to solve becomes

$$\begin{vmatrix} E_1 - E & H_{12} \\ H_{12}^* & E_2 - E \end{vmatrix} = 0, \tag{2-30}$$

where $H_{12} = \langle 1|\hat{H}'|2\rangle$. The solutions of the above secular equation are given by

$$E_{\pm} = \frac{1}{2}(E_1 + E_2) \pm \frac{1}{2}\sqrt{4|H_{12}|^2 + \Delta^2}, \quad \Delta = E_1 - E_2 . \tag{2-31}$$

Then, the orthonormalized *new* eigenvectors of the perturbed levels can be obtained by

$$|+\rangle = \left(\frac{\sqrt{4|H_{12}|^2 + \Delta^2} + \Delta}{2\sqrt{4|H_{12}|^2 + \Delta^2}} \right)^{1/2} |1\rangle - \left(\frac{\sqrt{4|H_{12}|^2 + \Delta^2} - \Delta}{2\sqrt{4|H_{12}|^2 + \Delta^2}} \right)^{1/2} |2\rangle \tag{2-32}$$

and

$$|-\rangle = \left(\frac{\sqrt{4|H_{12}|^2 + \Delta^2} - \Delta}{2\sqrt{4|H_{12}|^2 + \Delta^2}} \right)^{1/2} |1\rangle + \left(\frac{\sqrt{4|H_{12}|^2 + \Delta^2} + \Delta}{2\sqrt{4|H_{12}|^2 + \Delta^2}} \right)^{1/2} |2\rangle , \tag{2-33}$$

which have the eigenvalues E_+ and E_-, respectively. This result means that the perturbation $\hat{H}'$ mixes the *original* eigenstates $|1\rangle$ and $|2\rangle$ to create the *new* eigenstates $|+\rangle$ and $|-\rangle$. Simultaneously the energy shifts occur. The degree of the mixture of eigenstates and the degree of the energy shifts are characterized by the ratio $|H_{12}|/\Delta$.

Intensity borrowing

We suppose that we irradiate an electromagnetic wave onto a molecular system to excite it from the ground state $|\mathrm{g}\rangle$ to a bright excited state $|\mathrm{b}\rangle$. Also we suppose that the molecular system has a dark excited state $|\mathrm{d}\rangle$ (owing to any selection rules or other reasons), which is close to the bright excited state in energy. Therefore, we can suppose that the matrix

element of the electric dipole moment between $|\mathrm{g}\rangle$ and $|\mathrm{b}\rangle$ is non-zero, whereas that matrix element between $|\mathrm{g}\rangle$ and $|\mathrm{d}\rangle$ vanishes. The eigenstate mixing mechanism mentioned above indicates that in this case the bright state $|\mathrm{b}\rangle$ and the dark state $|\mathrm{d}\rangle$ are able to be mixed to generate the *new* excited states $|\mathrm{s}\rangle$ and $|\mathrm{w}\rangle$ ("s" means strong, whereas "w" means weak) which are written as

$$|\mathrm{s}\rangle = \left(\frac{\sqrt{4|H_{\mathrm{bd}}|^2 + \Delta^2} + \Delta}{2\sqrt{4|H_{\mathrm{bd}}|^2 + \Delta^2}} \right)^{1/2} |\mathrm{b}\rangle - \left(\frac{\sqrt{4|H_{\mathrm{bd}}|^2 + \Delta^2} - \Delta}{2\sqrt{4|H_{\mathrm{bd}}|^2 + \Delta^2}} \right)^{1/2} |\mathrm{d}\rangle, \tag{2-34}$$

$$|\mathrm{w}\rangle = \left(\frac{\sqrt{4|H_{\mathrm{bd}}|^2 + \Delta^2} - \Delta}{2\sqrt{4|H_{\mathrm{bd}}|^2 + \Delta^2}} \right)^{1/2} |\mathrm{b}\rangle + \left(\frac{\sqrt{4|H_{\mathrm{bd}}|^2 + \Delta^2} + \Delta}{2\sqrt{4|H_{\mathrm{bd}}|^2 + \Delta^2}} \right)^{1/2} |\mathrm{d}\rangle, \tag{2-35}$$

when the off-diagonal matrix element mixing the bright state and the dark state

$$H_{\mathrm{bd}} = \langle \mathrm{b}|\hat{H}'|\mathrm{d}\rangle \tag{2-36}$$

does not vanish. When this mixing between $|\mathrm{b}\rangle$ and $|\mathrm{d}\rangle$ is achieved, we may find the well-defined *splitting* of absorption or emission signal in the observed spectrum, where the stronger intensity component has the transition probability of

$$\begin{aligned} P_{\mathrm{s}} &\propto \left| \langle \mathrm{s}|\hat{\mu}|\mathrm{g}\rangle \right|^2 \\ &= \left| \left(\frac{\sqrt{4|H_{\mathrm{bd}}|^2 + \Delta^2} + \Delta}{2\sqrt{4|H_{\mathrm{bd}}|^2 + \Delta^2}} \right)^{1/2} \langle \mathrm{b}|\hat{\mu}|\mathrm{g}\rangle - \left(\frac{\sqrt{4|H_{\mathrm{bd}}|^2 + \Delta^2} - \Delta}{2\sqrt{4|H_{\mathrm{bd}}|^2 + \Delta^2}} \right)^{1/2} \langle \mathrm{d}|\hat{\mu}|\mathrm{g}\rangle \right|^2 \\ &= \frac{\sqrt{4|H_{\mathrm{bd}}|^2 + \Delta^2} + \Delta}{2\sqrt{4|H_{\mathrm{bd}}|^2 + \Delta^2}} \left| \langle \mathrm{b}|\hat{\mu}|\mathrm{g}\rangle \right|^2, \end{aligned} \tag{2-37}$$

and the weaker additional component has the transition probability of

$$
\begin{aligned}
P_{\mathrm{w}} &\propto \left|\langle \mathrm{w}|\hat{\mu}|\mathrm{g}\rangle\right|^2 \\
&= \left| \left(\frac{\sqrt{4|H_{\mathrm{bd}}|^2 + \Delta^2} - \Delta}{2\sqrt{4|H_{\mathrm{bd}}|^2 + \Delta^2}} \right)^{1/2} \langle \mathrm{b}|\hat{\mu}|\mathrm{g}\rangle + \left(\frac{\sqrt{4|H_{\mathrm{bd}}|^2 + \Delta^2} + \Delta}{2\sqrt{4|H_{\mathrm{bd}}|^2 + \Delta^2}} \right)^{1/2} \langle \mathrm{d}|\hat{\mu}|\mathrm{g}\rangle \right|^2 \\
&= \frac{\sqrt{4|H_{\mathrm{bd}}|^2 + \Delta^2} - \Delta}{2\sqrt{4|H_{\mathrm{bd}}|^2 + \Delta^2}} \left|\langle \mathrm{b}|\hat{\mu}|\mathrm{g}\rangle\right|^2 .
\end{aligned}
\tag{2-38}
$$

This result can be interpreted that the *originally* dark state obtained the transition intensity from the neighbor bright state through the coupling between them, and this is called the intensity borrowing mechanism. Here I have dealt with the simplest two-level system, and demonstrated the *splitting* of one signal into two components by the perturbation. If a given bright state couples with a number of surrounding dark states, the observed spectrum becomes much more complicated, resulting in the *forest* of signals.

2.6. Spectral linewidth

Doppler broadening

Random thermal distribution of gaseous molecules creates the Doppler shifts in absorption and emission of radiation. We suppose that the resonant angular frequency of a given molecular system is ω_0 in vacuum, and the propagation vector of the incident electromagnetic wave which interact with the molecular system is along the *X* axis. In this

case, the molecules, which have a component of velocity $u_X \neq 0$ along the X axis, experience a frequency shift; ω_0 is tuned to

$$\omega = \omega_0\left(1+\frac{u_X}{c}\right), \tag{2-39}$$

neglecting a small relativistic correction. Here c is the speed of light in vacuum. The velocity distribution at thermal equilibrium is described by the Maxwell-Boltzmann distribution; therefore, the number of molecule which interacts with the electromagnetic wave with angular frequency between ω and $\omega + \mathrm{d}\omega$ is given by [114]

$$n(\omega)\mathrm{d}\omega = \frac{cN_i}{\omega_0 u_p\sqrt{\pi}}\exp\left[-\left(\frac{c(\omega-\omega_0)}{\omega_0 u_p}\right)^2\right]\mathrm{d}\omega\,. \tag{2-40}$$

Here, N_i is the number density of molecules

$$N_i = \int n(u_z)\,\mathrm{d}u_z\,, \tag{2-41}$$

and u_p is the most probable speed

$$u_p = \sqrt{\frac{2RT}{W}}\,, \tag{2-42}$$

where R is gas constant, T is absolute temperature, and W is the molar mass. At the room temperature (T = 293 K), the most probable speeds of $^{14}NO_3$ and $^{15}NO_3$ are estimated to be u_p = 280 m s^{-1}. Spectral intensity is proportional to the density of molecules; therefore, the spectral shape is also given by a Gaussian function:

$$I(\omega) = I_0\exp\left[-\left(\frac{c(\omega-\omega_0)}{\omega_0 u_p}\right)^2\right]. \tag{2-43}$$

Full width at half maximum (FWHM) of this function is called the Doppler width, and this

linewidth is given by

$$\Delta\omega_D = \frac{2\omega_0}{c}\sqrt{\frac{2RT\ln 2}{W}}, \tag{2-44}$$

or in frequency,

$$\Delta\nu_D = \frac{2\nu_0}{c}\sqrt{\frac{2RT\ln 2}{W}}. \tag{2-45}$$

The above equation clearly indicates that the Doppler width is proportional to the resonant frequency of the molecular system of interest. Therefore, the reduction of the Doppler width is crucial for the high-resolution laser spectroscopy in the visible and/or ultraviolet region; otherwise the details of the observed spectra may not be revealed.

In case of the 0 – 0 band of the $\tilde{B}\,^2\mathrm{E}' \leftarrow \tilde{X}\,^2\mathrm{A}_2'$ transition of $^{14}NO_3$ radical which is located at 15100 cm^{-1}, inserting $\nu_0 = 4.53 \times 10^{14}$ Hz and $W = 0.062$ kg mol^{-1} leads to $\Delta\nu_D = 41 \times T^{1/2}$ in unit of MHz. At the room temperature ($T = 293$ K) the Doppler width is estimated to be 700 MHz (= 0.023 cm^{-1}). This Doppler width exceeds the spin-rotation interaction constant of NO_3 in the vibronic ground state in magnitude [74]. Therefore, again, it is indispensable that we reduce or cancel this Doppler width to realize rotationally-resolved high-resolution spectroscopy of NO_3.

Natural linewidth broadening

The Heisenberg uncertainty principle gives the natural linewidth in FWHM as

$$\Delta\omega_N = \frac{1}{\tau} \tag{2-46}$$

or in frequency,

$$\Delta v_N = \frac{1}{2\pi\tau}, \tag{2-47}$$

where τ is the spontaneous emission lifetime of excited molecules.

Nelson *et al.* reported that the NO_3 fluorescence decay from the $\tilde{B}\,^2E'$ state is non-exponential; the long-lived component (85% of the total emission) has the lifetime of 340 ± 20 μs, whereas the short-lived component (15%) has that of 27 μs [115]. These anomalously long fluorescence lifetimes result from so-called the Douglas effect [116]: the anomalously long lifetime owes to the large vibronic and/or rovibronic couplings between a bright state and the surrounding dark vibronic states. The long-lived lifetime and the short-lived one give the natural linewidth of 0.5 kHz and 5.9 kHz, respectively. These tiny natural linewidth broadenings can be negligible in this study.

Transit time broadening

The limited time of interaction between molecule and electromagnetic wave causes the broadening of observed spectral lines. We suppose here that the electromagnetic wave with a beam diameter of d is completely monochromatic with angular frequency ω_0, and the speed of molecule is v; therefore the molecule can interact with the electromagnetic wave for

a finite time $\tau_{\mathrm{int}} = d/v$ which is called the transit time.

The frequency distribution can be calculated by taking the Fourier transform of the monochromatic electromagnetic wave for the finite time τ_{int} as [117]

$$F(\omega) = \int_{-\tau_{\mathrm{int}}/2}^{+\tau_{\mathrm{int}}/2} E\cos(\omega_0 t)\exp[-i\omega t]\mathrm{d}t \approx \frac{E}{\omega_0 - \omega}\sin\left(\frac{\omega_0 - \omega}{2}\tau_{\mathrm{int}}\right), \tag{2-48}$$

where E is the amplitude of the electromagnetic wave. Because the line intensity is proportional to $|E|^2$, the unnormalized lineshape is given as

$$\left|F(\omega)\right|^2 = \frac{\sin^2\left(\frac{\omega_0 - \omega}{2}\tau_{\mathrm{int}}\right)}{(\omega_0 - \omega)^2}. \tag{2-49}$$

The normalized lineshape function is

$$g(\omega) = \frac{2\sin^2\left(\frac{\omega_0 - \omega}{2}\tau_{\mathrm{int}}\right)}{\pi\tau_{\mathrm{int}}(\omega_0 - \omega)^2}, \tag{2-50}$$

or in frequency,

$$g(\nu) = \frac{\sin^2\left(\pi(\nu - \nu_0)\tau_{\mathrm{int}}\right)}{\pi^2\tau_{\mathrm{int}}(\nu - \nu_0)^2}. \tag{2-51}$$

The FWHM of this function, which is called the transit time broadening, is numerically given by $0.89/\tau_{\mathrm{int}}$.

The most probable speed of $^{14}NO_3$ at the room temperature (293 K) is estimated to be 280 m s^{-1}, again, and we suppose the typical beam waist of the incident laser beam is 1 mm. In this case the transit time is estimated to be 3.6×10^{-6} s, leading to the transit time broadening of 25 kHz. This tiny broadening is also negligible in this study.

Power broadening

The application of an intense electromagnetic radiation to molecular system causes the broadening of spectral lines, because the Rabi frequency promoting the cycles between the ground state and the excited state is proportional to the amplitude of the incident electromagnetic wave:

$$\omega_R = \frac{\mu E}{\hbar}. \tag{2-52}$$

Here, E is the amplitude of the electromagnetic wave, and $\hbar$ is Dirac's constant. The physical quantity μ denotes a transition dipole moment, whose square is proportional to the absorption cross section σ:

$$\mu^2 = \frac{3\varepsilon_0 \hbar c}{\pi}\sigma, \tag{2-53}$$

where ε_0 is permittivity of vacuum. Equation (2-52) indicates that larger amplitude of the incident electromagnetic wave causes the higher Rabi oscillation frequency, leading to the shorter excited state lifetime. Then, analogously to the natural lifetime broadening, the spectral lines become broad. The power broadening in FWHM is given by

$$\Delta\nu_P \sim \frac{\omega_R}{4\pi^2}. \tag{2-54}$$

The absorption cross section of $^{14}NO_3$ radical at around 662 nm was reported to be 2.3 $\times 10^{-17}$ cm^2 = 2.3 $\times 10^{-21}$ m^2, by the low-resolution absorption spectroscopy [99]. In Chapter 4, we will see that the density of the observed rotational lines was about 1 $\times 10^3$ lines/nm in

this study. Therefore we can roughly estimate the absorption cross section per one rotational line to be 2×10^{-24} m^2, and then the transition dipole moment, which is also per one rotational line, is able to be estimated to be $\mu = 7 \times 10^{-31}$ C m = 0.2 Debye. In this study, the experimental power of the dye laser beam falling onto the NO_3 molecular beam was 200 – 300 mW, leading to the amplitude of the electromagnetic wave of $1 – 2 \times 10^4$ V m^{-1}, when the laser beam waist is 1 mm in diameter. Then the Rabi frequency is estimated to be 1×10^8 Hz, resulting in the power broadening of about 2 MHz. This broadening affects the observed linewidth, and therefore we should be careful about this broadening; however, this broadening is not so much problematic as the Doppler broadening.

Chapter 3. Experiment

3.1. NO_3 preparation

Various methods to generate NO_3 radical have been reported as following:

1) The pyrolysis reaction of N_2O_5 [118,119]:

$$N_2O_5 \rightarrow NO_3 + NO_2. \quad (3\text{-}1)$$

2) The photolysis reaction of N_2O_5:

$$N_2O_5 + h\nu \rightarrow NO_3 + NO_2. \quad (3\text{-}2)$$

3) The excimer laser photolysis reaction of peroxodisulfate anion ($S_2O_8^{2-}$) in the presence of nitrate anion [120]:

$$S_2O_8^{2-} + h\nu \rightarrow 2SO_4^{-}, \quad (3\text{-}3)$$

$$SO_4^{-} + NO_3^{-} \rightarrow SO_4^{2-} + NO_3. \quad (3\text{-}4)$$

4) The laser photolysis reaction of Cl_2 in the presence of $ClONO_2$ [101]:

$$Cl_2 + h\nu \rightarrow 2Cl, \quad (3\text{-}5)$$

$$Cl + ClONO_2 \rightarrow Cl_2 + NO_3. \quad (3\text{-}6)$$

5) The discharge reaction of F_2 in the presence of nitric acid [73-75]:

$$F_2 \rightarrow 2F, \quad (3\text{-}7)$$

$$F + HNO_3 \rightarrow HF + NO_3. \quad (3\text{-}8)$$

6) The photolysis reaction of ceric ammonium nitrate:

$$[Ce^{IV}(NO_3)_6]^{2-} + h\nu \rightarrow [Ce^{III}(NO_3)_5]^{2-} + NO_3. \quad (3\text{-}9)$$

7) The photolysis reaction of peroxyacetyl nitrate [121]:

$$CH_3C(O)O_2NO_2 + h\nu \rightarrow CH_3C(O)O + NO_3. \quad (3\text{-}10)$$

In this study, dinitrogen pentoxide (N_2O_5) was selected as a precursor of NO_3 radical, and NO_3 radical was generated by using the pyrolysis reaction of N_2O_5, because this reaction seemed to be the simplest method to generate NO_3 radical in the gas phase. Concerning to the generation method of NO_3, Carter *et al.* wrote in their paper that the discharge of N_2O_5 in neon was difficult to obtain the stable discharge conditions, and then they turned to the pyrolysis of N_2O_5 [104].

Professor Takashi Ishiwata (Graduate School of Information Sciences, Hiroshima City University) has provided me N_2O_5 during the course of study. N_2O_5 was synthesized in the dehydration reaction of nitric acid in the presence of phosphorus pentoxide:

$$2HNO_3 + P_2O_5 \rightarrow N_2O_5 + 2HPO_3. \quad (3\text{-}11)$$

In case of the spectroscopic study of $^{15}NO_3$ isotopologue, ^{15}N substituted dinitrogen pentoxide ($^{15}N_2O_5$) was a precursor of $^{15}NO_3$ radical, and the pyrolysis reaction of $^{15}N_2O_5$ was used to generate $^{15}NO_3$ radical. $^{15}N_2O_5$ was synthesized in the same way with $^{14}N_2O_5$, and $H^{15}NO_3$

Table 3-1. Natural abundance of NO_3.

Isotopologue	Natural abundance
$N^{16}O_3$	0.994
$N^{16}O_2{}^{18}O$	2×10^{-3}
$N^{16}O_2{}^{17}O$	4×10^{-4}
$N^{16}O^{18}O_2$	4×10^{-6}
$N^{16}O^{17}O^{18}O$	8×10^{-7}
$N^{16}O^{17}O_2$	2×10^{-7}
$N^{18}O_3$	8×10^{-9}
$N^{17}O^{18}O_2$	2×10^{-9}
$N^{17}O_2{}^{18}O$	3×10^{-10}
$N^{17}O_3$	6×10^{-11}

was prepared by the reaction of $Na^{15}NO_3$ (Shoko Co. Ltd., 99.8% ^{15}N) with H_2SO_4 and purified by vacuum distillation [72]. N_2O_5 solid was stored in a refrigerator, whose temperature was below –60°C.

The natural abundance of the atomic isotopes of oxygen was reported as ^{16}O (99.8%), ^{17}O (0.04%), and ^{18}O (0.2%) [122], resulting in the natural abundance of NO_3 radical as tabulated in Table 3-1, where $N^{16}O_3$ isotopologue is largely dominant. Therefore, it was considered that the isotopologues having only ^{16}O nuclei ($^{14}N^{16}O_3$ and $^{15}N^{16}O_3$) have been investigated during the course of study.

3.2. Molecular beam method and light source

Reduction of the Doppler width

To realize rotationally-resolved high-resolution laser spectroscopy of molecules, the reduction of the Doppler width is indispensable, because the Doppler width is proportional to the frequency of the electromagnetic wave interacting with molecular system, as already seen in Equation (2-45).

One of the fundamental ideas to achieve high-resolution spectroscopy beyond the Doppler limit is that we cross an aligned flow of molecules (a molecular beam) and the incident electromagnetic wave at the right angles in a vacuum chamber, in order to prevent molecules from having the velocity components along the propagation vector of the incident electromagnetic wave. The molecular beam is able to be realized by using a pulsed nozzle to eject gaseous sample into a vacuum chamber and mechanical apertures to collimate a molecular jet into a molecular beam.

When we place a mechanical skimmer whose diameter is b to collimate a molecular jet downstream of the nozzle by distance of d, the collimation ratio can be expressed by $b/(2d)$. Then the Doppler width can be reduced down to

$$\Delta\nu_D^* = \Delta\nu_D \tan\left(\frac{b}{2d}\right) \sim \Delta\nu_D \frac{b}{2d}. \tag{3-12}$$

Here, it was assumed that b is much smaller than d ($b << d$). The molecular beam method actually cannot eliminate the Doppler width completely, because the collimated molecular beam has a finite beam diameter. Then, high-resolution spectroscopy using a molecular beam belongs to sub-Doppler spectroscopic methods which are sometimes discriminated from Doppler-free spectroscopic methods because of the presence of remaining Doppler width. This remaining Doppler width is called the residual Doppler width.

Adiabatic cooling

The pulsed nozzle is also useful for the generation of a supersonic molecular jet by the adiabatic expansion which enables to cool molecules vibrationally and rotationally and allows us to observe much simpler spectra than those at the room temperature. Supersonic molecular jet was proposed by Kantrowitz and Grey in 1951 [123]. Here, I briefly summarize the supersonic jet expansion and the adiabatic cooling [124-126].

Under an isentropic free expansion of gas, the law of conservation in energy requires the equation

$$h_0 = h_1 + \frac{u^2}{2}, \tag{3-13}$$

where h_0 and h_1 are the enthalpies per unit mass before and after the adiabatic expansion, respectively, and u is the speed of molecules associated with the directed molecular flow.

Equation (3-13) indicates that the random thermal motions of molecules are converted into an aligned molecular flow along a particular direction. Temperature of gas corresponds to a variance of the Maxwell-Boltzmann distribution. This fact clearly shows that the aligned molecular flow has a low translational temperature. During random collisions of molecules, a part of vibrational and rotational energies can be converted into translational energy, toward equilibration. Therefore, under the free expansion into vacuum, gaseous molecules can be cooled vibrationally and rotationally.

We now suppose that the expanded gas is an ideal gas, which holds the relationship

$$h_0 - h_1 = C_{p,m}(T_0 - T_1) = \frac{\gamma}{\gamma - 1} R(T_0 - T_1) . \quad (3\text{-}14)$$

Here, R is gas constant, $C_{p,m}$ is the heat capacity at constant pressure per unit mass, and γ is the heat capacity ratio, i.e., $\gamma = C_{p,m}/C_{v,m}$, where $C_{v,m}$ is the heat capacity at constant volume per unit mass. T_0 and T_1 are the temperature of gas before and after expansion, respectively. From Equations (3-13) and (3-14) one can obtain the ratio of temperatures of gas after and before expansion as

$$\frac{T_1}{T_0} = \left(1 + \frac{\gamma - 1}{2} M^2\right)^{-1}, \quad (3\text{-}15)$$

where M is the Mach number which is the ratio of speed of a molecule u and the speed of sound a, i.e., $M = u/a$. Equation (3-15) indicates that larger M gives smaller T_1, because γ is larger than unity for all gases. Simultaneously, this equation also indicates that monoatomic gas is the most suitable as the carrier gas for the free expansion cooling, because the heat capacity

ratio γ of monoatomic gas, which is 5/3 (= 1.67), is larger than those of diatomic gases (γ = 7/5 = 1.40) or those of polyatomic gases (γ = 4/3 = 1.33).

Vacuum chamber setup and light source

A differentially-pumped vacuum chamber was used in this experiment. This vacuum chamber was separated into two chambers by a wall with one pinhole which is a skimmer. The first chamber in which gaseous sample is injected is called the source chamber. The second chamber in which sample and laser beam interact is called the main chamber. Each vacuum chamber was independently vacuumed by an oil diffusion pump (Edwards, Model 250/2000M, pumping speed in air: 2000 L s^{-1}) followed by a rotary pump (Edwards, E2M40, swept volume: 50.5 m^3 h^{-1} @60 Hz). In order to enlarge the swept volume, a mechanical booster pump (Edwards, EH 250) was attached to the rotary pump vacuuming the source chamber. The pressure of the each vacuum chamber was monitored independently with both a penning vacuum gauge (ULVAC, GI-PA) and an ionization vacuum gauge (ULVAC, GI-M2). Typical pressures of the source chamber and the main chamber were 1×10^{-2} Pa and 3×10^{-3} Pa, respectively, during the sample injection.

Figure 3-1 shows a part of the experimental setup of this study. N_2O_5 vapor was mixed with helium gas (about 1 bar) at –5°C, and injected into the source chamber through a

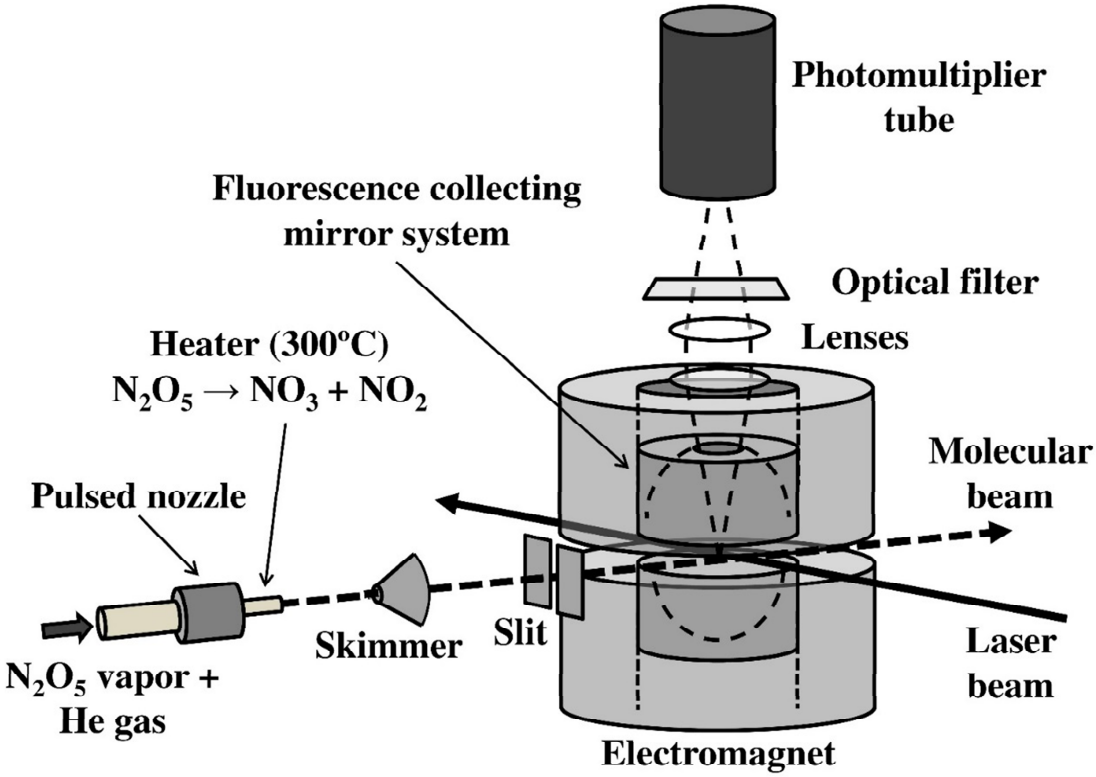

Figure 3-1. Schematic experimental setup for the fluorescence excitation spectroscopy and the Zeeman effect observation by using the molecular beam method.

pulsed nozzle which was converted from a solenoid valve (Toyota, automobile fuel injector, orifice diameter 0.8 mm). The mixture gas was heated to about 300°C with a heater attached to the pulsed nozzle, to generate NO_3 radical in a molecular jet by the N_2O_5 pyrolysis reaction: $N_2O_5 \rightarrow NO_3 + NO_2$. The heater to generate NO_3 radical consists of a ceramic tube (length 25 mm, inner and outer diameters are 1 mm and 2 mm respectively) with a Kanthal wire. Figure 3-2 schematically shows the setup of the pulsed nozzle and the heater for the NO_3 generation. The heater temperature was monitored during the experiment with an alumel-

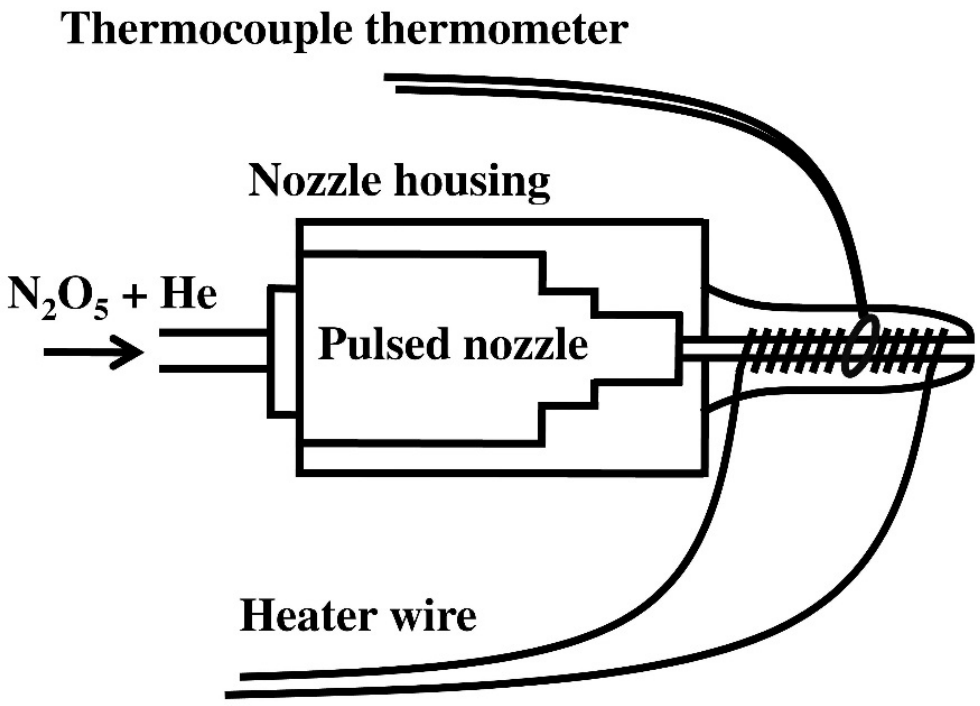

Figure 3-2. Setup of the pulsed nozzle and the heater for the NO_3 generation.

chromel thermocouple thermometer. The supersonic jet was collimated into a molecular beam with a skimmer (diameter 2 mm) and a slit (width 2 mm) which were placed about 5 cm and 30 cm, respectively, downstream of the pulsed nozzle. With this setup of the skimmer and the slit, the Doppler width could be reduced down to several megahertz.

A single-mode ring dye laser (Coherent, CR699-29, dye: DCM special, about 1 MHz energy linewidth) pumped by a Nd: YVO_4 laser (Coherent, Verdi V-10, wavelength 532 nm) was used as a tunable light source with a narrow linewidth. Single-mode operation of the dye laser was achieved by inserting a birefringent filter (BRF) and an intra-cavity assembly (ICA)

into the laser resonator. ICA consists of two étalons with different thickness from each other. Combination of BRF and ICA allowed us to reduce the gain below the laser threshold except only one selected frequency mode. Dye solution, which was a medium of the dye laser, was prepared by dissolving powder DCM special of 1 g by benzyl alcohol of 500 mL, which was followed by mixing with ethylene glycol of 500 mL. Benzyl alcohol was needed to dissolve DCM special, and ethylene glycol was needed to make the dye solution viscous for the stability of the dye jet flow. Typical powers of the output of the pump laser and the dye laser were 7 W and 600 mW (in the single-mode operation), respectively. The wavenumber scanning was carried out by tilting a galvanometer-driven Brewster plate, and the drive voltage for this wavenumber scanning of this dye laser was fed from a stable DC source (Yokogawa 7651). Typical frequency scanning rate of this study was 10 MHz/s, or 0.0003 cm^{-1}/s in wavenumber. The wavenumber of an output of the dye laser was monitored by a wavemeter (Burleigh, Wave Meter WA-1500-VIS-KK) which includes a scanning Michelson interferometer, and fringe patterns of a reference cavity of the dye laser was also monitored with an oscilloscope, during the experiment to check the wavenumber scanning was correctly working.

The collimated molecular beam was crossed with the incident dye laser beam at the right angles in the main chamber in order to reduce the Doppler width. High-resolution fluorescence excitation spectra were observed by detecting the fluorescence with a photomultiplier tube (Hamamatsu, R2758). The detected signal was amplified with a high

speed amplifier unit (Hamamatsu, C5594) and then inputted into a gated photon counter (Stanford Research Systems, SR400). The molecular beam, the dye laser beam, and the direction of detection were all mutually perpendicular (See Figure 3-1). Fluorescence collecting mirror system, which consists of a half-spherical mirror and a half-ellipsoidal mirror, was used for the effective collection of fluorescence. The scattered laser light was blocked just before the photomultiplier tube with color filters (Toshiba, an R69 and an R70 filters).

A pair of solenoids were attached outside of the fluorescence collecting mirror system to observe the Zeeman effect. The details of this electromagnet will be described in the following section.

3.3. Electromagnet

To observe the Zeeman splitting of the rotational lines clearly, a homogeneous external magnetic field is needed; an inhomogeneous magnetic field is not suitable for this purpose, because the interaction between the inhomogeneous magnetic field and the electronic spin give rise to the deflection of molecules, which was demonstrated by Stern and Gerlach [127] (the Stern-Gerlach experiment), ending up with the absence of molecules at the intersection with the incident dye laser beam. In this study a homogeneous magnetic field was generated by using a pair of solenoids as a Helmholtz coil.

Figure 3-3. Electromagnet.

A pair of solenoids was attached outside of the fluorescence collecting mirror system. Figure 3-3 shows a picture of the electromagnet. Each solenoid consists of an aluminum hollow tube whose inner and outer diameters are 80 mm and 100 mm, respectively, with one layer of water cooling tube of 1/8 inch in diameter made with copper which was followed by about 1200 windings of a wire of 2 mm in diameter. The separation between the solenoids was 15 mm.

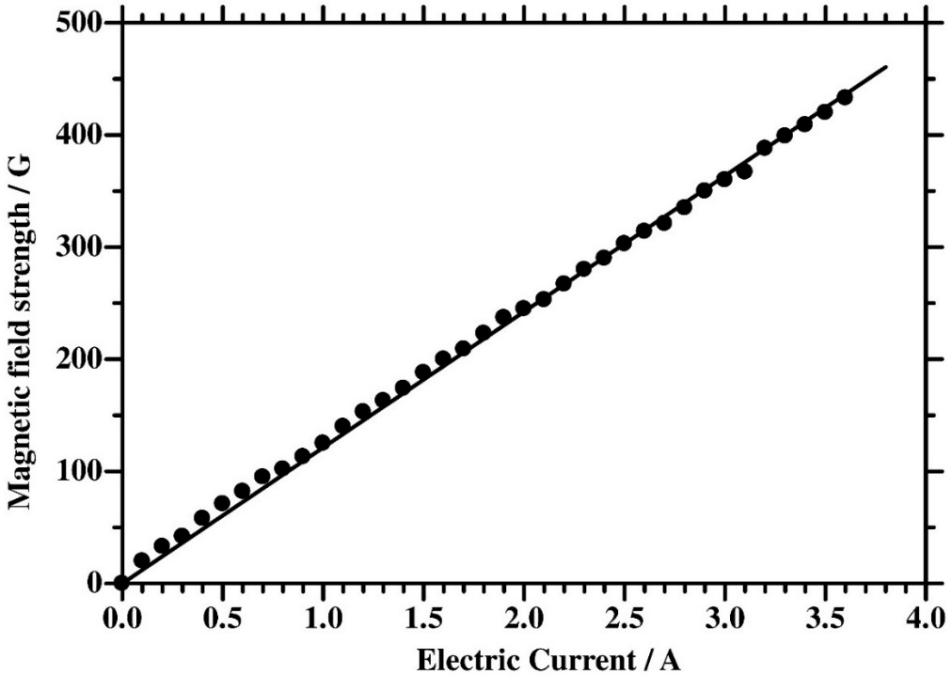

Figure 3-4. Obtained magnetic field strength against an electric current at the intersection of the molecular beam and the dye laser beam. The solid line is a function: $H = 121.2 \times I$, where H is magnetic field strength in unit of gauss and I is electric current in unit of ampere.

Before the Zeeman effect observation, the performance of this electromagnet was evaluated with a gaussmeter (Walker LDJ Scientific Inc. MG-4D). A power supply (Takasago, EX-375L) enabled to apply an electric current up to 3.6 A for a very short time (Figure 3-4); however, the high-resolution laser spectroscopy needs a long time to scan the frequency of the incident laser beam. Appling high electric current for a long time resulted in a sharp rising the solenoids' temperature. Therefore, the reality was that an electric current was available up to 3.0 A and a homogeneous magnetic field was obtained up to 360 G at the intersection of the molecular beam and the incident laser beam. The polarization of the incident laser beam

was selected to be either perpendicular to the magnetic field vector (the σ-pump condition) or parallel with the magnetic field vector (the π-pump condition).

3.4. Absolute wavenumber calibration

To determine the precise spectroscopic constants of molecules, we must carry out the spectroscopic study with not only high-resolution but also high-accuracy. Then, to calibrate absolute wavenumber of the NO_3 signal in high-accuracy, a Doppler-free saturation spectrum of iodine molecule and a fringe pattern of a stabilized confocal étalon were recorded simultaneously with the NO_3 spectrum measurement. Figure 3-5 shows a typical scan of this study. The upper trace is the fringe pattern of the étalon. The middle trace is the Doppler-free saturation spectrum of iodine molecule, in which the hyperfine structure can be recognized. The lower trace is the fluorescence excitation spectrum of $^{14}NO_3$. The details of the étalon and the iodine spectroscopy will be described as the following.

Doppler-free saturation spectroscopy of iodine molecule

We suppose that we introduce two tunable laser beams with the completely same angular frequency ω_0 into a gas cell from opposite sides each other, and also suppose that we

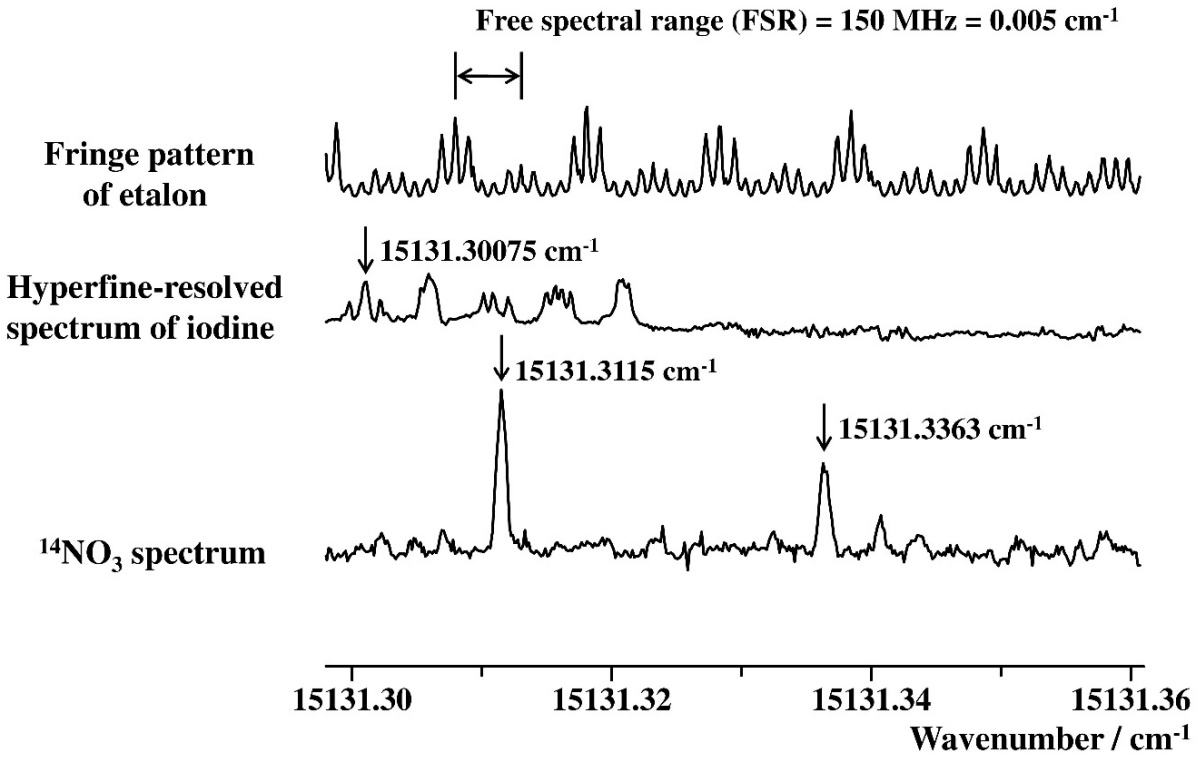

Figure 3-5. Typical scan of this study. (Upper) The transmission spectrum of the stabilized étalon as an interpolation frequency marker. (Middle) The Doppler-free saturation spectrum of iodine molecule as a frequency standard. (Lower) The observed high-resolution fluorescence excitation spectrum of $^{14}NO_3$. These three spectra were recorded simultaneously to calibrate absolute wavenumber.

observe an absorption spectrum as a function of laser frequency by detecting the intensity of the transmitted laser beam. In this case, because of the saturation effect, the population in the absorbing level of molecules decreases, leading to a small sharp dip at ω_0 in the Doppler-broadened absorption profile. This dip caused by saturation of population in the absorbing level is called the Lamb dip. This Lamb dip is a Doppler-free signal, because only the molecules interacting with both two laser beams with opposite directions simultaneously, i.e.,

the molecules with no velocity components along the propagation vector of the incident laser beams are able to contribute to this dip signal.

Iodine molecule is often used as the standard for the calibration of absolute frequency, because the rich rotational lines of the $\tilde{B}\,{}^3\Pi_{0^+_u} \leftarrow \tilde{X}\,{}^1\Sigma_g^+$ electronic transition of iodine molecule are widely spread in the visible region, 14000 – 20000 cm^{-1}. This electronic transition is allowed because of the strong spin-orbit interaction caused by the heavy atom effect. Additionally, we can find the vast hyperfine signals with sharp linewidths owing to the total nuclear spin of iodine molecule of five: the rotational lines with even *J"* split into 15 hyperfine lines, and those with odd *J"* split into 21 hyperfine lines.

As the frequency standard, the Doppler-free saturation spectrum of iodine molecule was observed in this experiment, by using an iodine gas cell. The experimental setup for this saturation spectroscopy is shown in Figure 3-6. A portion of output of the dye laser was split into a strong pump beam and a weak probe beam by the first polarization beam splitter (PBS1). The pump beam was periodically chopped at about 2.9 kHz by a mechanical chopper (EG & G Princeton Applied Research, Model 197), because the combination of the periodical chopping of the pump beam and a lock-in detection of the probe beam enables us to eliminate the Doppler-broadened background of the observed spectrum. Then the pump beam traveled clockwise (M1 → PBS2 → M2 → iodine cell → M3 → PBS1), and finally went to a beam catcher. On the other hand, the probe beam traveled counterclockwise (M3 → iodine cell →

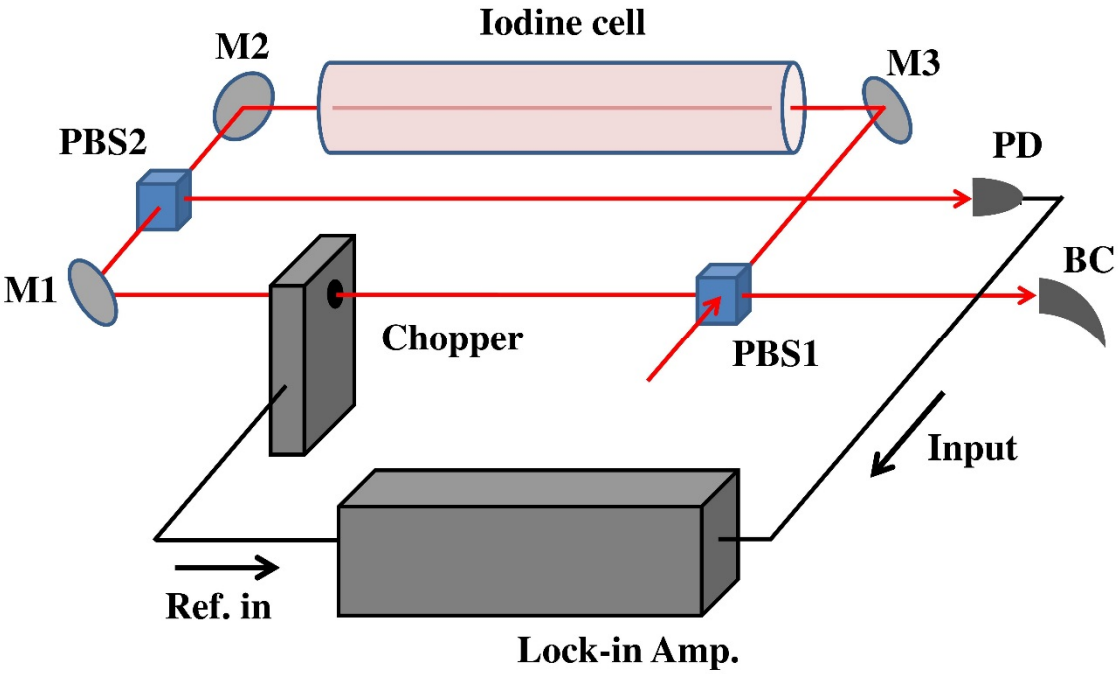

Figure 3-6. Setup for Doppler-free saturation spectroscopy of iodine molecule. M is mirror, PBS is polarization beam splitter, PD is photodiode, and BC is beam catcher.

M2 → PBS2). Then the intensity of probe beam was detected with a photodiode which was followed by a lock-in amplifier (NF Electronic Instruments, LI-570A).

The region around 15000 – 15500 cm^{-1} corresponds to the hot bands of iodine molecule from the vibrational quantum numbers of $\upsilon'' \geq 2$ [128]. Therefore, I had to heat the iodine cell to about 50°C to record the Doppler-free spectrum of iodine molecule in good signal-to-noise ratio.

Stabilized étalon

A confocal étalon (Burleigh, CFT-500) was used in this study. When we use a confocal étalon, the transmission from this étalon gives maxima at the condition of

$$v = \frac{M}{4nL}, \tag{3-16}$$

where v is the wavenumber of the incident laser beam, M is the resonance order, n is refractive index of the medium inside the étalon, and L is the spacing between the two mirrors which consist of this étalon. In this experiment, n was close to unity and L was 500 mm. The FSR (free spectral range), which is the peak-to-peak interval in a transmission spectrum, of this étalon was thus about 0.005 cm^{-1} (= 150 MHz). The dye laser beam which was fed into the étalon was modulated in frequency by 30 MHz (= 0.001 cm^{-1}) with an electro-optic modulator (Newport, Resonant phase modulator, 4001). If we hold the cavity length L constant, we can obtain the transmission spectrum of this étalon with constant FSR, which can be used as a ruler with the constant interval of 150 MHz and the minimum scale value of 30 MHz (See the upper spectrum in Figure 3-5).

At first, another Doppler-free saturation spectroscopy of iodine molecule was carried out by using an output of a single-mode Nd: YAG laser (Innolight, Prometheus 20, wavelength 532 nm, power 20 mW). Then, the output wavenumber of this Nd: YAG laser was locked to the *o* hyperfine line of the $\tilde{B}\,^3\Pi_{0^+_u}$ (v' = 32, J' = 53) ← $\tilde{X}\,^1\Sigma_g^+$ (v'' = 0, J'' = 54) rovibronic

transition of iodine molecule which is located at 18786.75142 cm^{-1} or 532.290005 nm in wavelength, by using the method reported by Arie *et al.* [129]. Then, this frequency-locked laser beam passed through the étalon, and the cavity length of the étalon was actively stabilized to satisfy the resonance condition against this laser beam, by using the Pound-Drever-Hall locking method [130], as described in Ref. 131. I continued to confirm that the étalon cavity locking was working well during the experiment.

Calibration

Under the assumptions that the FSR of the stabilized étalon is constant within the spectral range of the scan and that the frequency steps of the ring dye laser are constant between the successive fringe patterns, the absolute wavenumber calibration was performed with the following procedure. At first, the FSR and absolute wavenumbers of the fringe pattern peaks of the stabilized étalon were determined accurately based upon the observed spectrum of iodine molecule, by referring to the high-resolution spectral atlas of iodine molecule [131]. In this way, we can obtain the étalon markers with the constant FSR, whose absolute wavenumbers were precisely determined. Then, the absolute wavenumber of each NO_3 signal was calibrated by using this stabilized étalon markers. The standard deviation of the absolute wavenumber calibration with the high-resolution atlas is reported to be 0.000054 cm^{-1} [131].

The absolute wavenumber error can be evaluated to be 1/10 of the minimum scale value of the stabilized étalon (30 MHz = 0.001 cm^{-1}) in this experiment. Therefore, the absolute wavenumber of each NO_3 rotational line was calibrated in the accuracy of 0.0001 cm^{-1}.

3.5. NO_2 spectroscopy

I also observed high-resolution fluorescence excitation spectra of NO_2 by using commercially available NO_2 gas (Sumitomo Seika Chemicals Co. Ltd., purity > 99%) to discriminate the NO_3 signals from the NO_2 signals experimentally, because the N_2O_5 pyrolysis reaction generates not only NO_3 but also NO_2, and NO_2 also absorbs the visible light. This visible absorption of NO_2 mainly corresponds to the $\tilde{A}\,^2B_2 - \tilde{X}\,^2A_1$ electronic transition. NO_2 was mixed with helium gas at –10°C and expanded into the vacuum chamber. NO_2 gas was not heated, because NO_2 is pyrolyzed to generate NO + O_2 [132-135], ending up with the low signal-to-noise ratio. The other experimental setup was the same as that of the NO_3 experiment.

Chapter 4. High-resolution laser spectroscopy of $^{14}NO_3$ radical

4.1. Result and analysis

Spectral feature

Figure 4-1 shows the high-resolution fluorescence excitation spectrum observed by using the N_2O_5 pyrolysis reaction: $N_2O_5 \rightarrow NO_3 + NO_2$. The observed region was 15070 – 15145 cm^{-1}, where is assigned to the 0 – 0 band of the $\tilde{B}\,^2E' \leftarrow \tilde{X}\,^2A_2'$ transition [95]. In this region, intense signals concentrate at around 15085 cm^{-1}, 15100 cm^{-1}, 15115 cm^{-1}, and 15130 cm^{-1} region. This spectral feature is similar to the feature reported by Carter *et al.* previously [104]. A portion of the observed spectrum (0.4 cm^{-1}) is shown in Figure 4-2 (a). Each signal is the rotational line. Typical linewidth of the observed rotational lines was about 25 MHz in full width at half maximum, which is mainly due to the residual Doppler width and the frequency jitter of the dye laser. Any hyperfine structures originated from the ^{14}N nuclear were not recognized in the spectral resolution of this study: 0.0008 cm^{-1}. In the 15070 – 15145 cm^{-1} region, about 150 strong rotational lines and more than 3000 weak rotational lines were found. The rotational line density was about 1×10^3 lines / nm. The rotational assignment seemed to be difficult, because the observed spectrum did not seem to have the

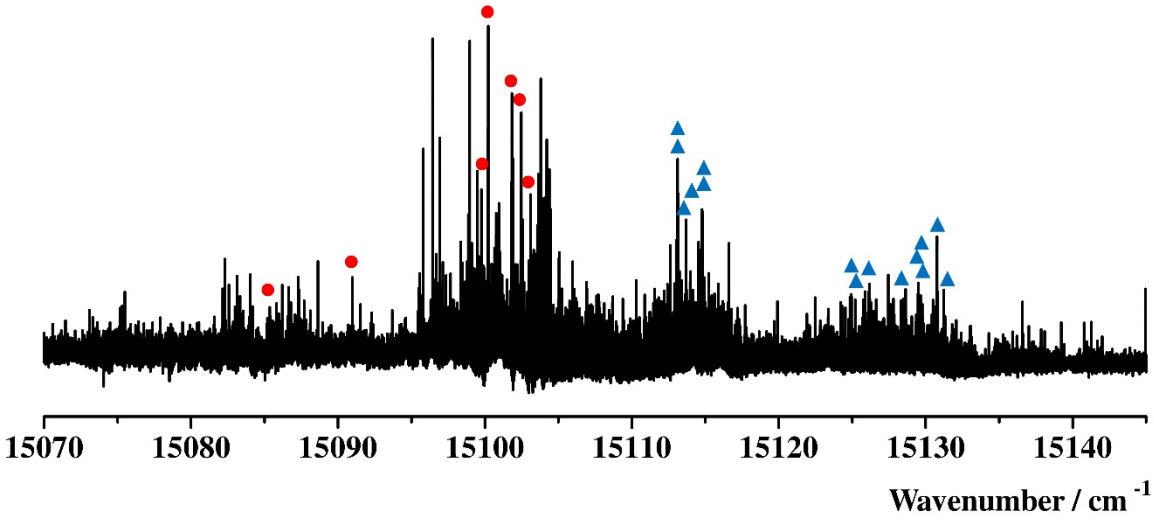

Figure 4-1. The observed high-resolution fluorescence excitation spectrum of $^{14}NO_3$. The red circles and the blue triangles indicate the rotational line pairs with 0.0246 cm^{-1} spacing and are assigned to the transitions to the lowest *J'* levels, i.e., the $^2E'_{3/2}$ (*J'* = 1.5) levels and $^2E'_{1/2}$ (*J'* = 0.5) levels, respectively. See the text.

regular rotational branch structures.

In this study the N_2O_5 pyrolysis reaction: $N_2O_5 \rightarrow NO_3 + NO_2$ was used to generate NO_3. In this case, the NO_2 contamination to the NO_3 spectrum is unavoidable. In the observed 15070 – 15145 cm^{-1} region, four vibronic bands of NO_2 have been reported at 15097.6 cm^{-1}, 15135.2 cm^{-1}, 15138.0 cm^{-1}, and 15150.1 cm^{-1} by Smalley *et al* [125]. Then, in order to discriminate the NO_3 signals from the NO_2 signals, I also observed the high-resolution fluorescence excitation spectra of pure NO_2. A part of the observed NO_2 spectrum is shown in Figure 4-2 (b), where the two rotational lines with the hyperfine structures appeared

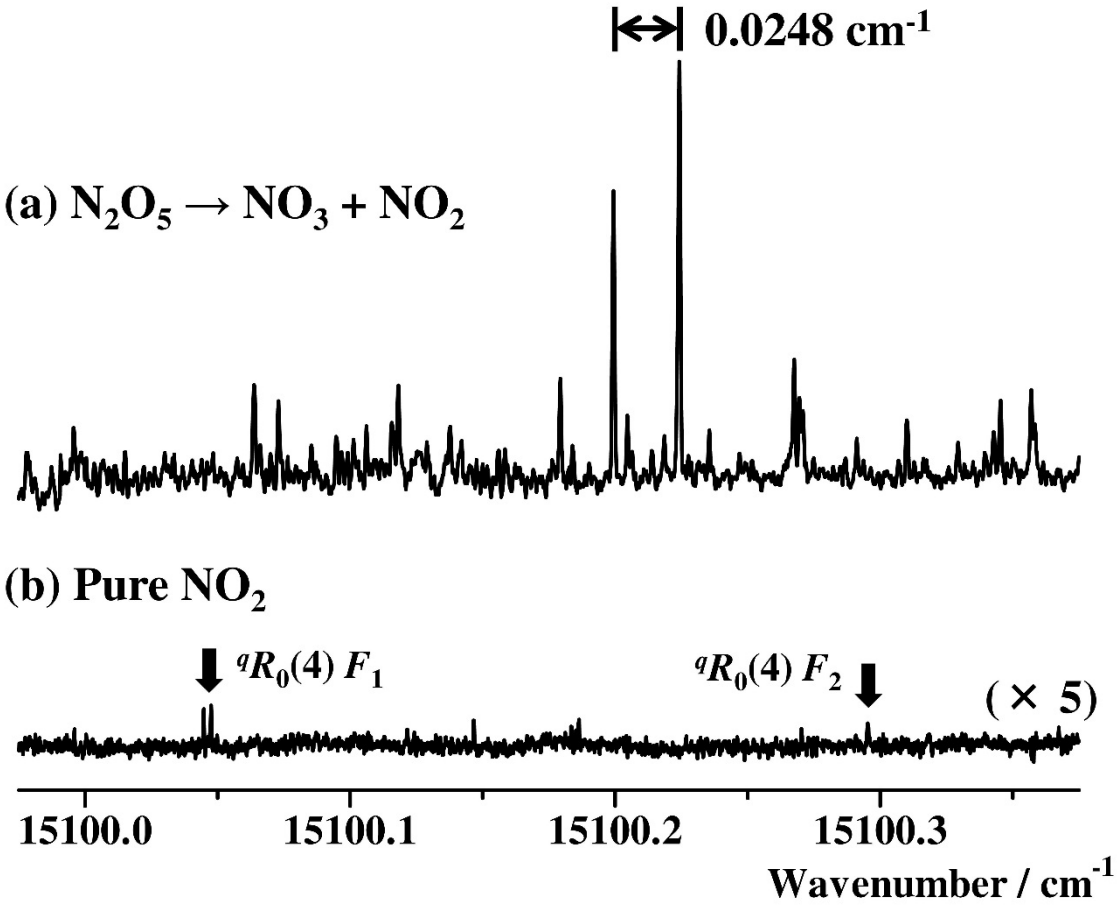

Figure 4-2. A portion of the high-resolution fluorescence excitation spectrum. (a) Fluorescence excitation spectrum observed by using the N_2O_5 pyrolysis reaction: $N_2O_5 \rightarrow NO_3 + NO_2$. One rotational line pair with about 0.0246 cm^{-1} spacing can be seen at about 15100.2 cm^{-1}. (b) Fluorescence excitation spectrum observed by using commercial pure NO_2 gas. The rotational lines of NO_2 are indicated by the arrows. Note that the spectrum (b) is magnified by five in intensity.

as indicated by arrows. They were assigned as the F_1 and F_2 spin components of the $^qR_0(4)$ line of the 15097.6 cm^{-1} band, referring to the reported molecular constants [125]. Here, we adopt the nomenclature $^{\Delta k}\Delta N_{k''}(N'')$ in labeling the NO_2 rotational lines. NO_2 is a prorate-like

asymmetric top molecule, and *k* is the projection of **N** along the molecular fixed *a* axis. These $^qR_0(4)$ lines were the most intense lines in this 15097.6 cm^{-1} band under the experimental condition of this study; however, they were not found in Figure 4-2 (a). Other rotational lines of the 15097.6 cm^{-1} band were also not found in the spectrum observed by using the N_2O_5 pyrolysis reaction. The other three vibronic bands of NO_2 around 15100 cm^{-1} region have the similar band intensities with the 15097.6 cm^{-1} [125]. Therefore, it was confirmed that the NO_2 contamination to the NO_3 spectrum can be ignored around 15100 cm^{-1} region. As mentioned in Section 3.5, NO_2 may be pyrolyzed to generate NO molecule, but NO molecule is not a problem, because the lowest electronic transition ($\tilde{A}\,^2\Sigma^+ \leftarrow \tilde{X}\,^2\Pi_r$) of NO molecule lies at around 44000 cm^{-1} [136]. Here, the subscript *r* indicates the *regular* spin-orbit splitting.

Zeeman effect observation and rotational assignment

In the observed spectrum, I found more than 20 remarkable rotational line pairs with about 0.0246 cm^{-1} spacing. An example of such rotational line pairs can be seen at around 15100.2 cm^{-1} in Figure 4-2 (a). I envisaged that these line pairs correspond to the rovibronic transitions with lower quantum numbers, because they have large line intensities under the jet-cooled condition. Then I started the rotational assignment from these line pairs.

When we set the quantum number *k* to be zero, the rotational energies of the spin

components in the ground state can be simplified as

$$E(N)_{F_1} = BN(N+1) - D_N N^2 (N+1)^2 + \frac{\varepsilon_{bb}}{2} N\,, \tag{4-1}$$

$$E(N)_{F_2} = BN(N+1) - D_N N^2 (N+1)^2 - \frac{\varepsilon_{bb}}{2} (N+1)\,, \tag{4-2}$$

from Equations (2-13), (2-14) and (2-15). Thus the separation between the F_1 and F_2 spin components is equal to $\varepsilon_{bb}(N + 1/2)$. The ε_{bb} value reported by Fujimori *et al.* is –0.01642(14) cm^{-1} [74]. Then I recognized that the observed 0.0246 cm^{-1} spacing is 1.5 times larger than this reported ε_{bb} value in magnitude: this means that the observed 0.0246 cm^{-1} spacing originates from the spin-rotation splitting of the $\tilde{X}\,^2A_2$' (v = 0, k = 0, N = 1) rotational level. Then, these line pairs were assigned to the rovibronic transitions from the $\tilde{X}\,^2A_2$' (v" = 0, k" = 0, N" = 1, J" = 0.5 and 1.5) levels to certain rovibronic excited levels. If the excited electronic state $\tilde{B}\,^2$E' was described by Hund's coupling case (b), this 0.0246 cm^{-1} spacing was never directly observed in the fluorescence excitation spectrum owing to the selection rules: $F_1 \leftrightarrow F_1$ and $F_2 \leftrightarrow F_2$ are allowed, whereas $F_1 \leftrightarrow F_2$ is forbidden, because the electronic spin states must not change during optical transitions, as expressed by the Kronecker's delta in Equation (2-28). Therefore, I confirmed that the $\tilde{B}\,^2$E' state is described by Hund's coupling case (a). From the selection rules of the $\tilde{B}\,^2$E' ← $\tilde{X}\,^2A_2$' transition, three types of transition;

$^2E'_{3/2}$ (P' = 1.5, k' = 1, J' = 1.5) ← $\tilde{X}\,^2A_2$' (k" = 0, N" = 1, J" = 0.5 and 1.5),

$^2E'_{1/2}$ (P' = 0.5, k' = 1, J' = 0.5) ← $\tilde{X}\,^2A_2$' (k" = 0, N" = 1, J" = 0.5 and 1.5),

$^2E'_{1/2}$ (P' = 0.5, k' = 1, J' = 1.5) ← $\tilde{X}\,^2A_2$' (k" = 0, N" = 1, J" = 0.5 and 1.5),

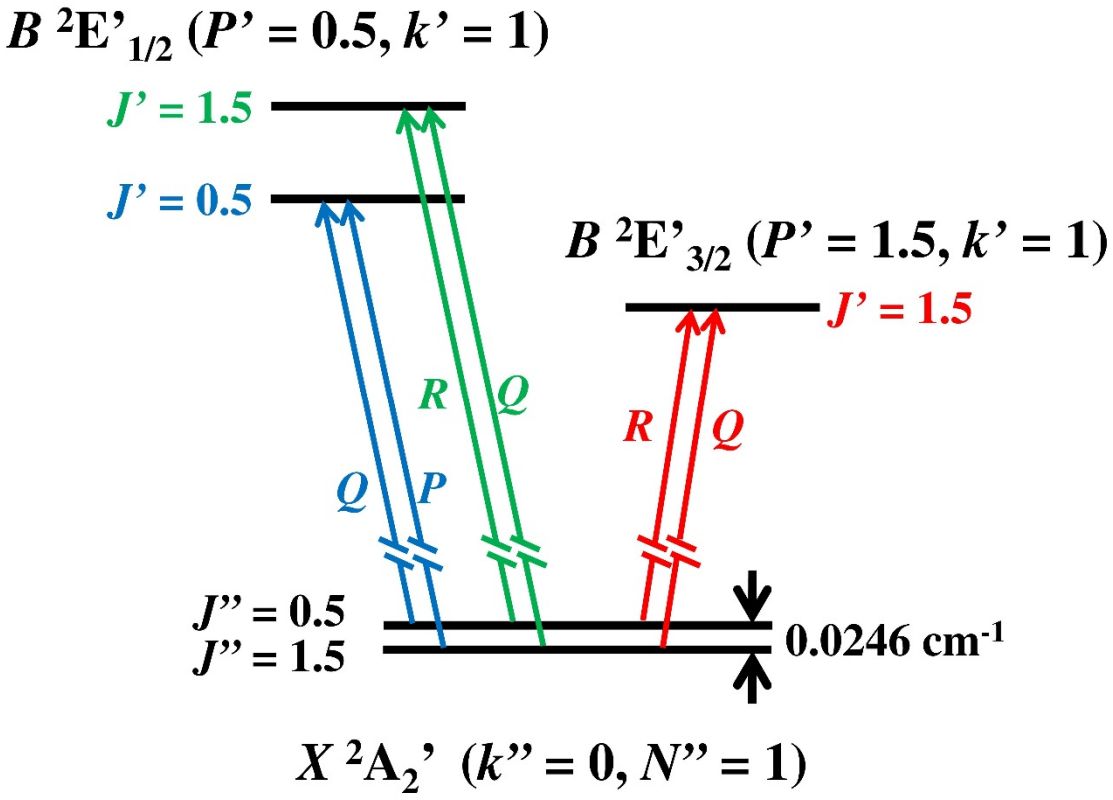

Figure 4-3. Three types of the allowed rovibronic transitions from the $\tilde{X}\,^2A_2'$ (v" = 0, k" = 0, N" = 1, J" = 0.5 and 1.5) to the $^2E'_{3/2}$ (J' = 1.5), $^2E'_{1/2}$ (J' = 0.5) and $^2E'_{1/2}$ (J' = 1.5) levels. These transitions correspond to the rotational line pairs with 0.0246 cm^{-1} spacing.

correspond to the rotational line pairs with 0.0246 cm^{-1} spacing. Figure 4-3 shows these allowed transitions schematically. To discriminate these transitions from each other I observed the Zeeman splitting by applying an external magnetic field, because the Zeeman splitting depends on the quantum numbers of the upper and lower levels (See Section 2.3) and thus it is useful for unambiguous rotational assignment.

Figures 4-4 and 4-5 show the observed Zeeman splitting for the σ-pump and π-pump

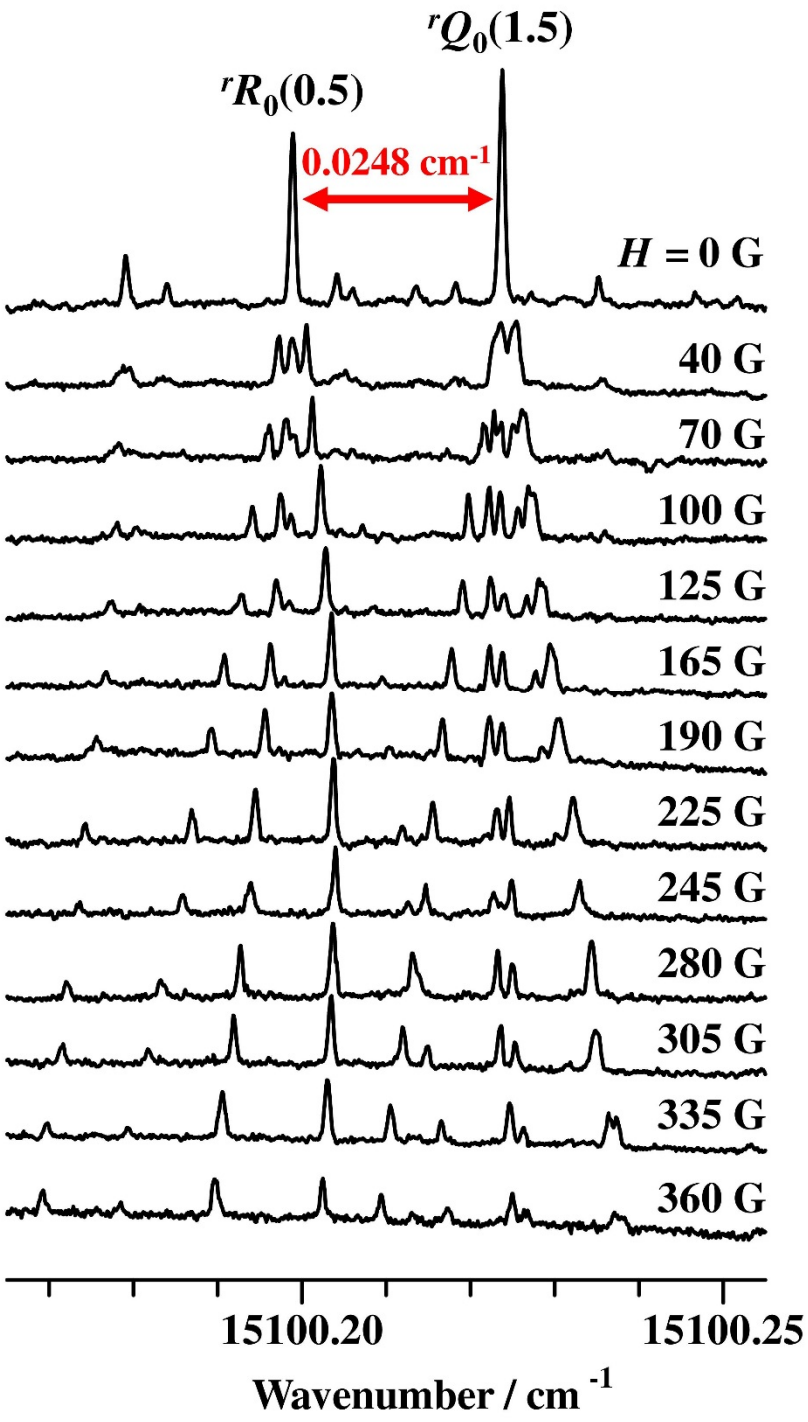

Figure 4-4. Fluorescence excitation spectrum of NO_3 at around 15100.2 cm^{-1}, and its variation with the external magnetic field strength H for the σ-pump condition. In this region one pair of $^rR_0(0.5)$ and $^rQ_0(1.5)$ of the $^2E'_{3/2} \leftarrow \tilde{X}\ ^2A_2'$ transition were assigned.

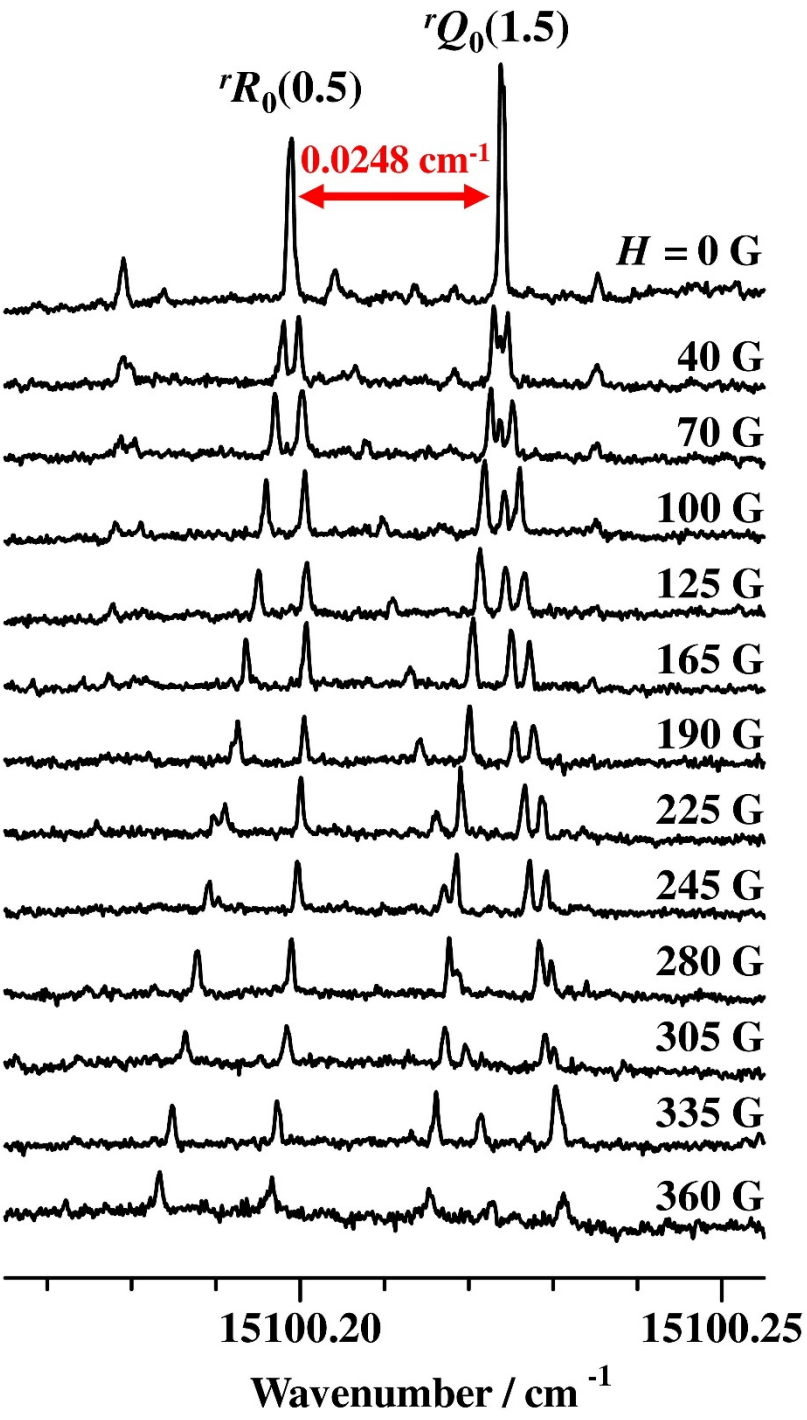

Figure 4-5. Fluorescence excitation spectrum of NO_3 at around 15100.2 cm^{-1}, and its variation with the external magnetic field strength *H* for the π-pump condition.

conditions, respectively, of the 15100.1990 cm^{-1} and 15100.2238 cm^{-1} line pair. The selection rules of the σ-pump and π-pump conditions are $\Delta M_J = \pm 1$ and $\Delta M_J = 0$, respectively, when M_J is a good quantum number. For the σ-pump condition, the 15100.1990 cm^{-1} line splits into four Zeeman components, and the 15100.2238 cm^{-1} line splits into six components (three of the six components are almost in superposition). On the other hand for the π-pump condition, the 15100.1990 cm^{-1} line splits into two Zeeman components whereas the 15100.2238 cm^{-1} line seems to split into three, actually four, Zeeman components. After several trials, I found that this line pair corresponds to the transition $^2E'_{3/2}$ (P' = 1.5, J' = 1.5) ← $\tilde{X}\,^2A_2'$ (k'' = 0, N'' = 1, J'' = 0.5 and 1.5), by comparing the observed Zeeman splitting and the calculated splitting using Equations (2-18), (2-19) and (2-22). The g-factors were determined by least squares fitting as g_S = 2.020(36) for the ground state and $g_{\rm eff}$ (= $g_L\zeta_e d + g_S/2$) = 0.889(30) for this excited state. Numbers in parentheses denote the standard deviation, and apply to the last digits of the values. The calculated and the observed transition energies of the Zeeman components of the line pair at 15100.2 cm^{-1} for the σ-pump and π-pump conditions are shown in Figures 4-6 and 4-7, respectively. The observed transition energies are plotted by the filled circles, and the calculated transition energies with the determined g-factors are shown by the solid lines. The observed transition energies are in good agreement with the calculated ones. Therefore, I successfully assigned this rotational line pair to $^rR_0(0.5)$ and $^rQ_0(1.5)$ of the $^2E'_{3/2} \leftarrow \tilde{X}\,^2A_2'$ transition. Here, we adopt the nomenclature $^{\Delta k}\Delta J_{k''}(J'')$

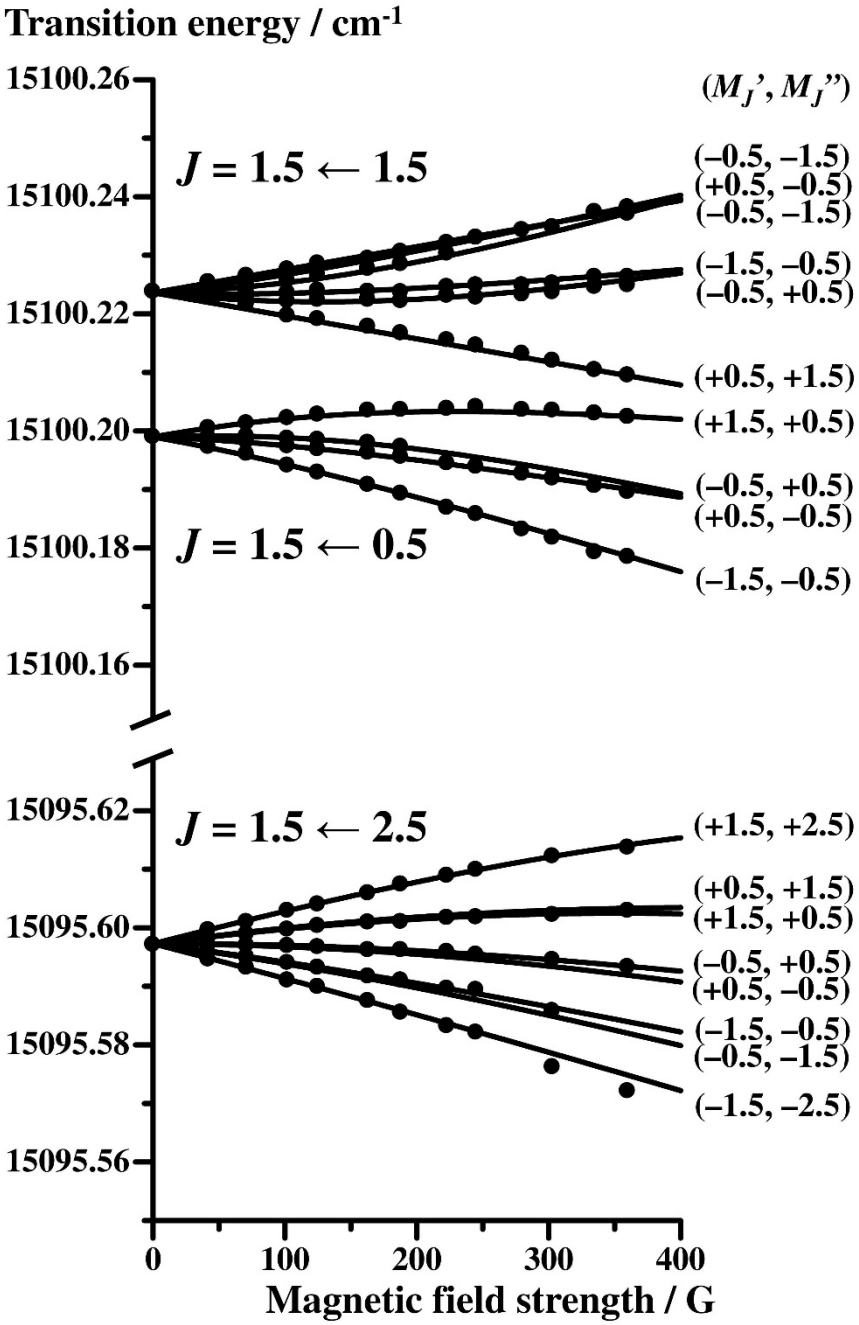

Figure 4-6. Transition energies of the observed Zeeman components at around 15095.6 cm^{-1} and 15100.2 cm^{-1} region for the σ-pump condition at the various magnetic field strengths are plotted by the filled circles. The solid lines indicate the calculated Zeeman splitting with the determined *g*-factors: g_S = 2.020 for the ground state and g_{eff} = 0.889 for this excited state.

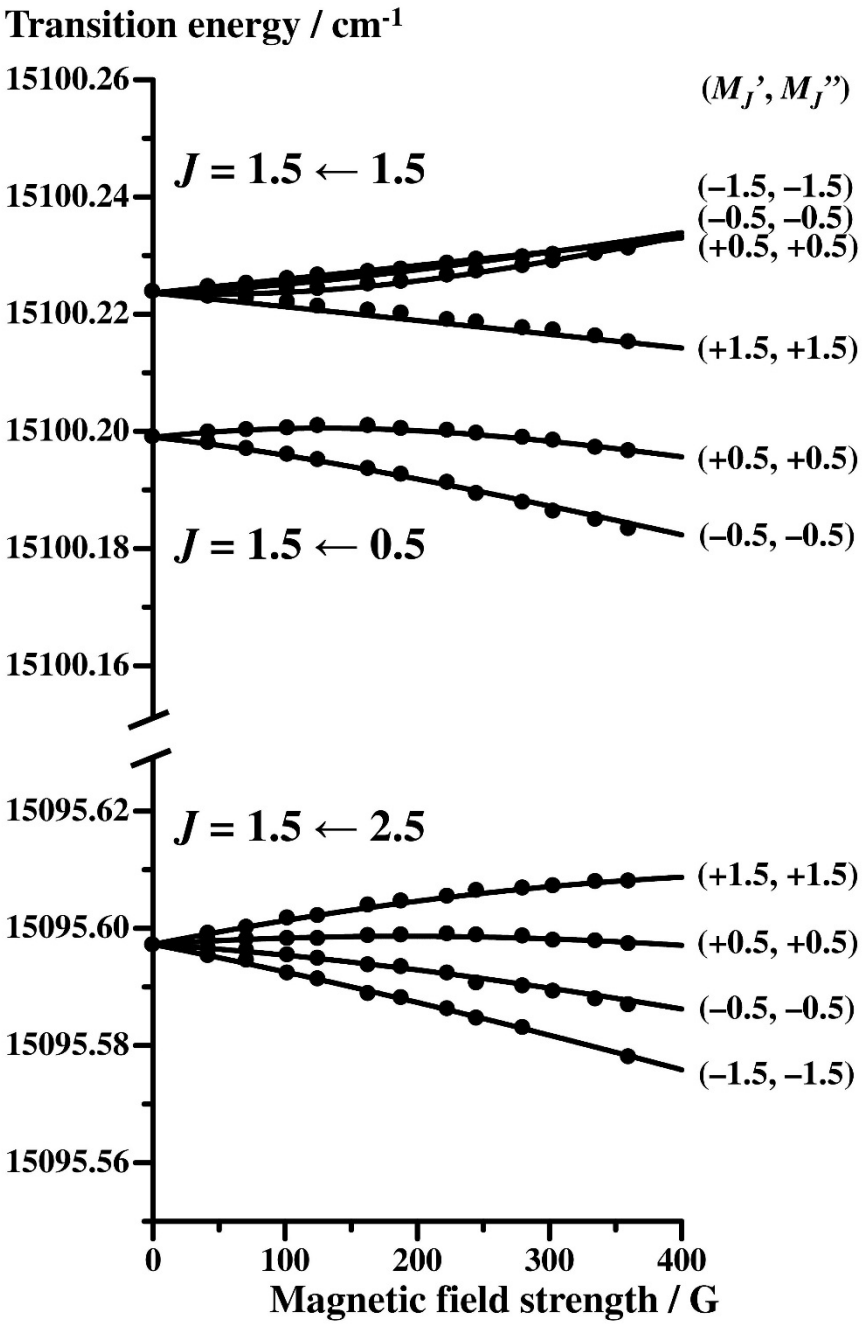

Figure 4-7. Transition energies of the observed Zeeman components at around 15095.6 cm^{-1} and 15100.2 cm^{-1} region for the π-pump condition at the various magnetic field strengths are plotted by the filled circles. The solid lines indicate the calculated Zeeman splitting with the determined *g*-factors: g_S = 2.020 for the ground state and g_{eff} = 0.889 for this excited state.

in labeling the rotational lines of NO_3. The $^rP_0(2.5)$ line of this $^2E'_{3/2} \leftarrow \tilde{X}\,^2A_2'$ transition, which shares the upper $J' = 1.5$ level with these $^rR_0(0.5)$ and $^rQ_0(1.5)$ lines, was expected to be located at around 15095.597 cm^{-1} based on the ground state combination differences calculated from the molecular constants [74]. Then the rotational line located at 15095.5971 cm^{-1} was assigned to the $^rP_0(2.5)$ line. Figures 4-8 and 4-9 show the Zeeman splitting of the 15095.5971 cm^{-1} line for the σ-pump and π-pump conditions, respectively. For the σ-pump condition the 15095.5971 cm^{-1} line seems to split into five Zeeman components, whereas for the π-pump condition, four Zeeman components. This Zeeman splitting is consistent with the rotational assignment to $^rP_0(2.5)$, as illustrated in Figures 4-6 and 4-7 where the observed and the calculated transition energies of the Zeeman components of the 15095.5971 cm^{-1} line agree well. Therefore, these 15095.5971 cm^{-1}, 15100.1990 cm^{-1}, and 15100.2238 cm^{-1} lines were unambiguously assigned to $^rP_0(2.5)$, $^rR_0(0.5)$, and $^rQ_0(1.5)$ of the $^2E'_{3/2} \leftarrow \tilde{X}\,^2A_2'$ transition, respectively. These are the first rotational assignments of $^{14}NO_3$ radical in its electronic transition in the visible region. In a similar way, by using the ground state combination differences and the Zeeman splitting, rotational lines located at 15097.8878 cm^{-1}, 15097.8300 cm^{-1}, and 15102.4565 cm^{-1} were assigned to $^rP_0(3.5)$, $^rQ_0(2.5)$, and $^rR_0(1.5)$ of the $^2E'_{3/2} \leftarrow \tilde{X}\,^2A_2'$ transition, respectively, sharing the upper $^2E'_{3/2}$ ($P' = 1.5$, $J' = 2.5$) level. Assuming these six transitions to $J' = 1.5$ and $J' = 2.5$ belong to a single vibronic band, the effective molecular constants of this $^2E'_{3/2}$ state were estimated to be $B = 0.447$ cm^{-1} and $T_0 = 15100.0$ cm^{-1}, under

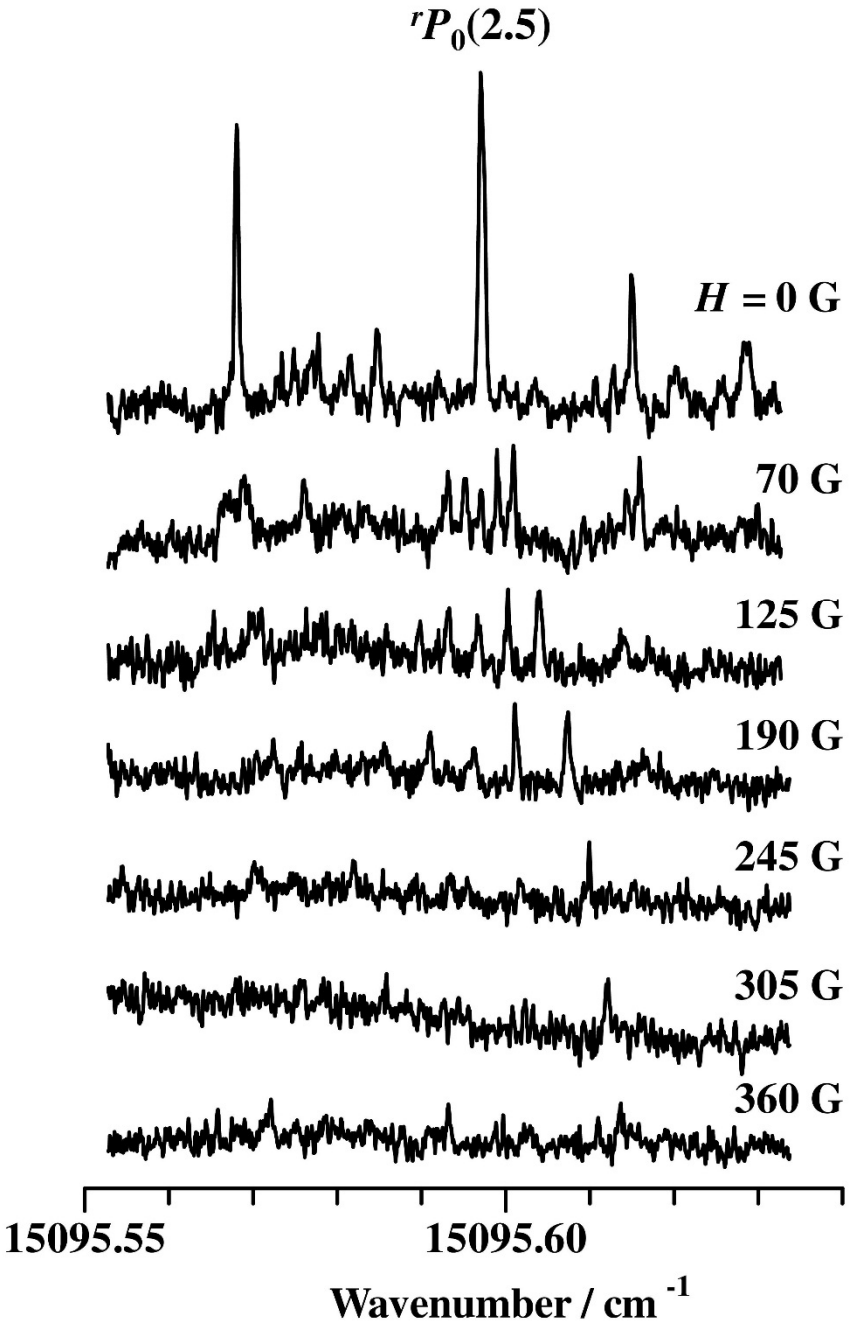

Figure 4-8. Fluorescence excitation spectrum of NO_3 at around 15095.6 cm^{-1} and its variation with the external magnetic field strengths *H* for the σ-pump condition. In this region the $^{r}P_0$(2.5) line of the $^{2}E'_{3/2} \leftarrow \tilde{X}\,^{2}A_2'$ transition was assigned.

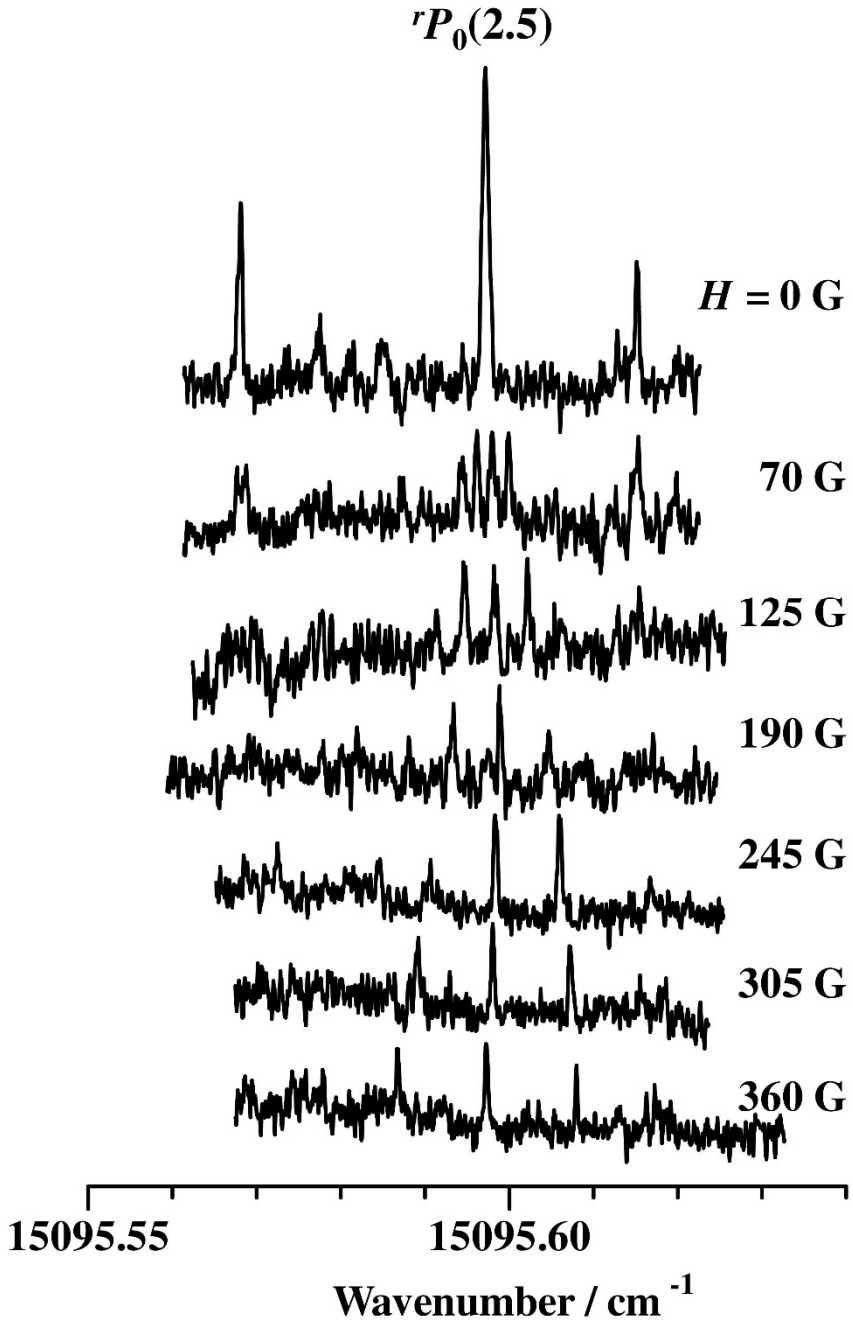

Figure 4-9. Fluorescence excitation spectrum of NO_3 at around 15095.6 cm^{-1} and its variation with the external magnetic field strengths *H* for the π-pump condition.

the oblate symmetric-top model, in which the simplest rotational energy form is expressed as $E_{J,P} = T_0 + B\,J\,(J + 1) + (C - B)\,P^2$ and $C = B / 2$. Here, B and C are the rotational constants and T_0 is the band origin. The assigned rotational lines, which belong to the $^2E'_{3/2} \leftarrow \tilde{X}\,^2A_2'$ transitions, and the determined g_{eff} values of the rovibronic excited levels are tabulated in Table 4-1, where the observed vibronic bands of NO_3 were named after the lower line positions of the rotational line pairs with 0.0246 cm^{-1} spacing corresponding to the transition to the lowest J', because many vibronic bands were identified in the 15070 – 15145 cm^{-1} region. For example, the vibronic band including the 15100.1990 cm^{-1} and 15100.2238 cm^{-1} line pair was named the 15100.2 cm^{-1} band.

Seven rotational line pairs with 0.0246 cm^{-1} spacing, which were assigned to the $^2E'_{3/2} \leftarrow \tilde{X}\,^2A_2'$ transitions by their Zeeman splitting, were found to distribute in the region below 15105 cm^{-1}. On the other hand, 15 rotational line pairs, which were assigned to the $^2E'_{1/2} \leftarrow \tilde{X}\,^2A_2'$ transitions, were found above 15112 cm^{-1}. The positions of the rotational line pairs are shown in Figure 4-1, where the filled circles indicate the transitions to the $^2E'_{3/2}$ spin-orbit component, and the filled triangles indicate the transitions to the $^2E'_{1/2}$ spin-orbit component. As an example of the rotational line pairs corresponding to the $^2E'_{1/2} \leftarrow \tilde{X}\,^2A_2'$ transition, the Zeeman splitting of 15130.7423 cm^{-1} and 15130.7670 cm^{-1} lines which were assigned to $^rQ_0(0.5)$ and $^rP_0(1.5)$ respectively, is shown in Figures 4-10 (σ-pump) and 4-11 (π-pump). For the σ-pump condition, the15130.7423 cm^{-1} and 15130.7670 cm^{-1} lines seem to split into two

Table 4-1. The transition energies of the assigned rotational lines which belong to the $^2E'_{3/2} \leftarrow \tilde{X}\,^2A_2'$ transition, the effective rotational constants of the upper states, and the determined effective g-factors of the $^2E'_{3/2}$ (J') levels. The transition energies are in units of wavenumber. The assignments of all rotational lines listed here were confirmed by the Zeeman splitting. Number in parentheses with the $g_{eff}(J')$ value denotes the standard deviation.

J'	$^rP_0(J'+1)$		$^rQ_0(J')$		$^rR_0(J'-1)$		$g_{eff}(J')$
15085.4 cm^{-1} band							
1.5	15080.7537	F_2	15085.3816	F_1	15085.3565	F_2	+0.45(12)
15091.0 cm^{-1} band							
1.5	[a]		15090.9777	F_1	15090.9534	F_2	+1.05(6)
15099.9 cm^{-1} band							
1.5	[a]		15099.8970	F_1	15099.8725	F_2	+0.66(9)
15100.2 cm^{-1} band (B_{eff} = 0.447 cm^{-1})							
1.5	15095.5971	F_2	15100.2238	F_1	15100.1990	F_2	+0.89(3)
2.5	15097.8878	F_1	15097.8300	F_2	15102.4565	F_1	+0.75(14)
15101.8 cm^{-1} band (B_{eff} = 0.509 cm^{-1})							
1.5	15097.2112	F_2	15101.8383	F_1	15101.8135	F_2	+0.92(6)
2.5	15099.8156	F_1	15099.7578	F_2	15104.3853	F_1	+0.75(14)
15102.4 cm^{-1} band (B_{eff} = 0.518 cm^{-1})							
1.5	15097.8445	F_2	15102.4716	F_1	15102.4468	F_2	+0.14(4)
2.5	15100.4820	F_1	15100.4237	F_2	15105.0511	F_1	[b]
3.5	15095.7930	F_2	15104.1196	F_1	15104.0628	F_2	[b]
15103.1 cm^{-1} band							
1.5	15098.4747	F_2	15103.1014	F_1	15103.0766	F_2	+0.66(12)

[a] Not found.

[b] In these upper J' levels, g_{eff} is close to zero. Then, the effective g-factors could not be determined precisely.

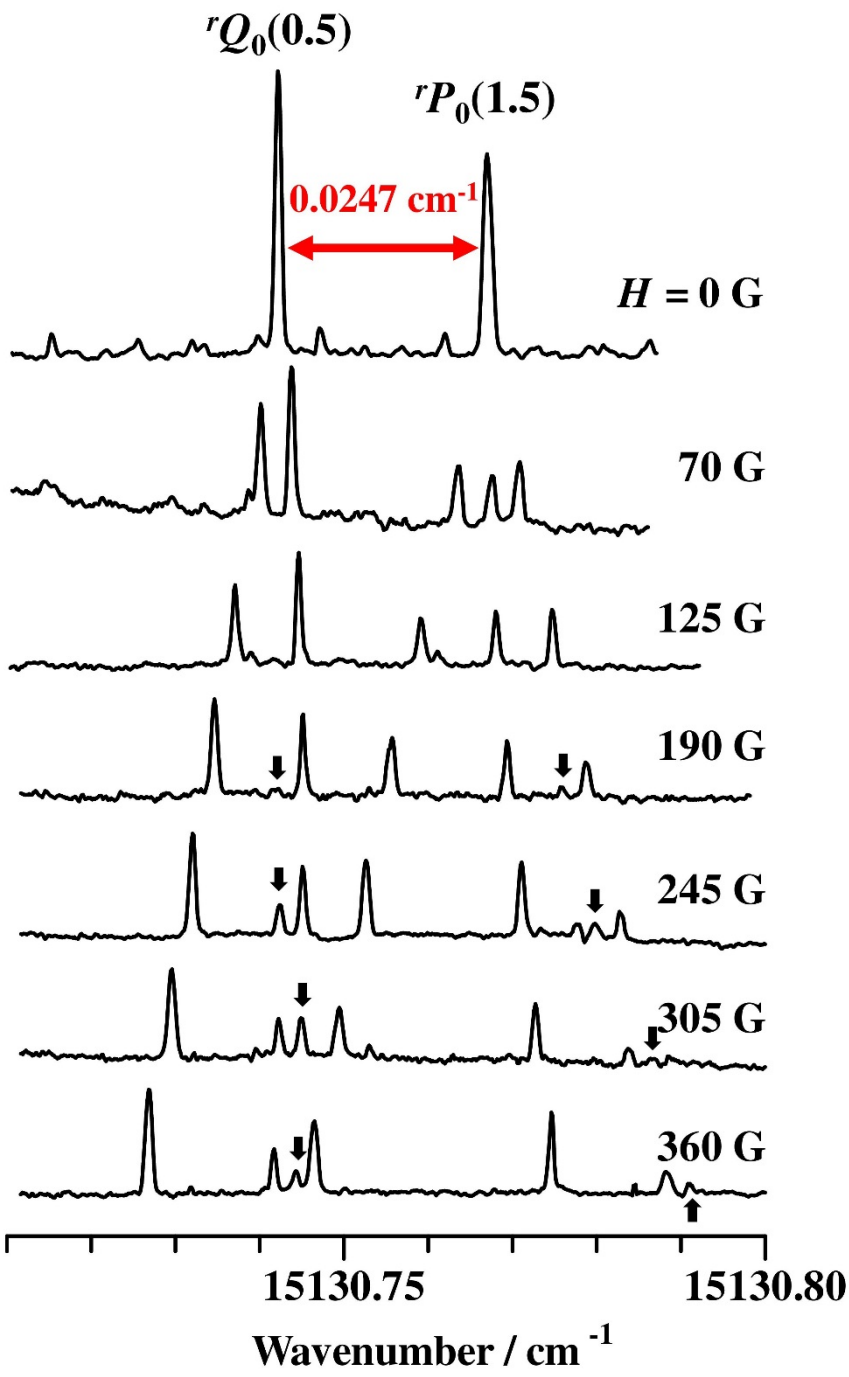

Figure 4-10. Fluorescence excitation spectrum of NO_3 at around 15130.75 cm^{-1} and its variation with external magnetic field strengths H for the σ-pump condition. In this region a pair of $^rQ_0(0.5)$ and $^rP_0(1.5)$ of the $^2E'_{1/2} \leftarrow \tilde{X}\,^2A_2'$ transition were assigned. The arrows indicate the signals originated from the perturber.

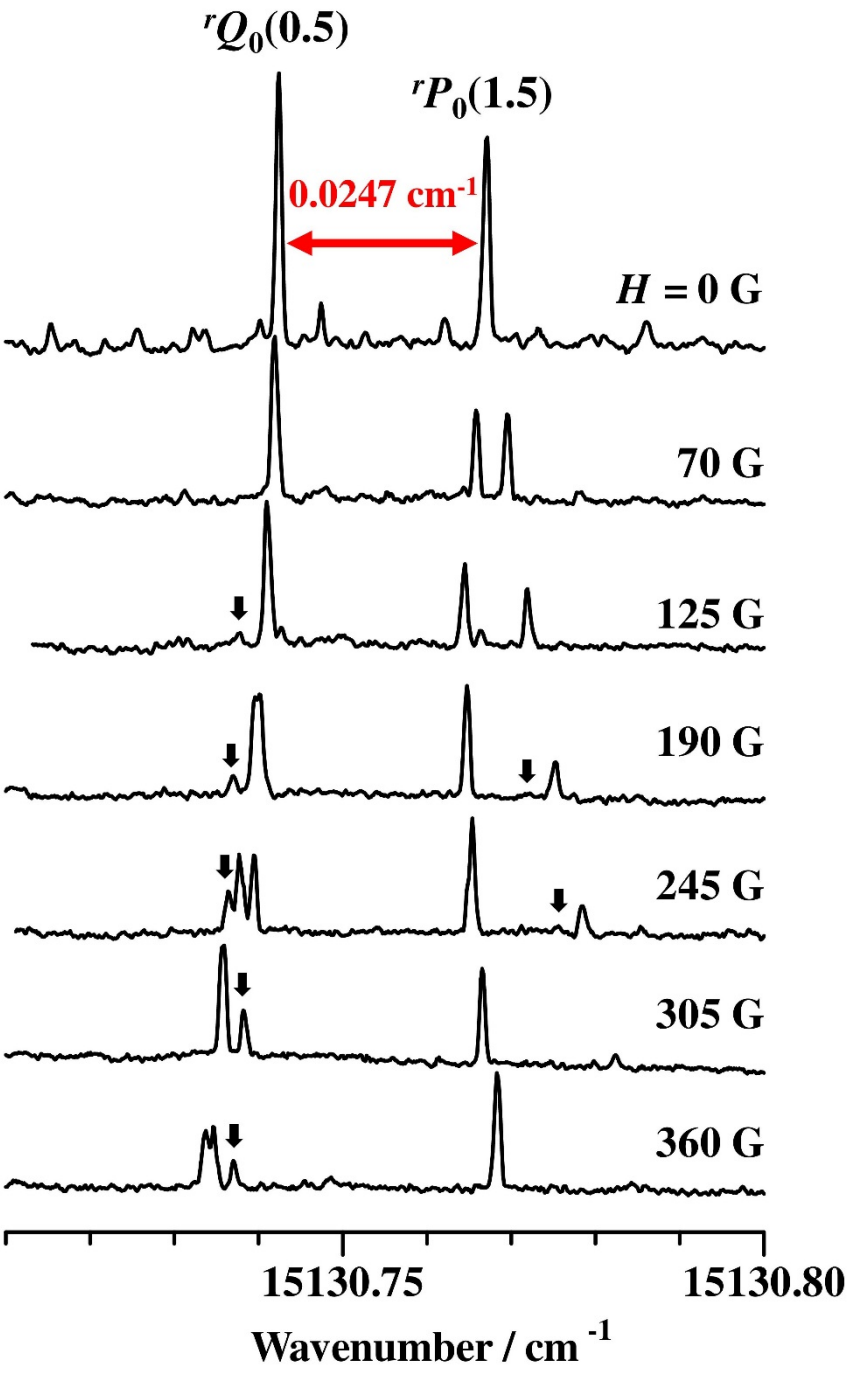

Figure 4-11. Fluorescence excitation spectrum of NO_3 at around 15130.75 cm^{-1} and its variation with external magnetic field strengths H for the π-pump condition. The arrows indicate the signals originated from the perturber.

and three, but in verity two and four, Zeeman components, respectively. On the other hand for the π-pump condition, the 15130.7423 cm^{-1} seems to remain one component and the 15130.7670 cm^{-1} line splits into two components. This Zeeman splitting is consistent with the $^rQ_0(0.5)$ and $^rP_0(1.5)$ rotational assignment, as shown in Figures 4-12 (σ-pump) and 4-13 (π-pump) where the comparisons between the observed and calculated transition energies of the Zeeman components at 15130.75 cm^{-1} region are illustrated. The observed transition energies of Zeeman splitting are plotted by the filled and blank circles. The calculated transition energies using the determined *g*-factors g_S = 2.020 (fixed) for the ground state and g_{eff} (= $g_L\zeta_e d - g_S/2$) = –0.725(91) for this excited state are drown by the solid lines. The observed transition energies are in good agreement with the calculated ones. An anomaly of the Zeeman splitting was recognized when an external magnetic field larger than 150 G was applied. This anomaly can be explained as a local perturbation with a neighbor level with the same quantum number M_J. From Equation (2-21) the neighbor level with the same M_J is able to perturb when the selection rule ΔJ = 0, ±1 is fulfilled, because the off-diagonal matrix elements do not vanish. In Figures 4-12 and 4-13 we can see only the M_J' = –0.5 level is perturbed by the neighbor level. The filled and blank circles indicate the transition energies to the perturbed M_J' = –0.5 level and the perturbing M_J' = –0.5 level, respectively. The Zeeman components of the perturber are indicated by arrows in Figures 4-10 and 4-11. The assigned rotational lines, which belong to the $^2E'_{1/2} \leftarrow \tilde{X}\,^2A_2'$ transitions, and the determined

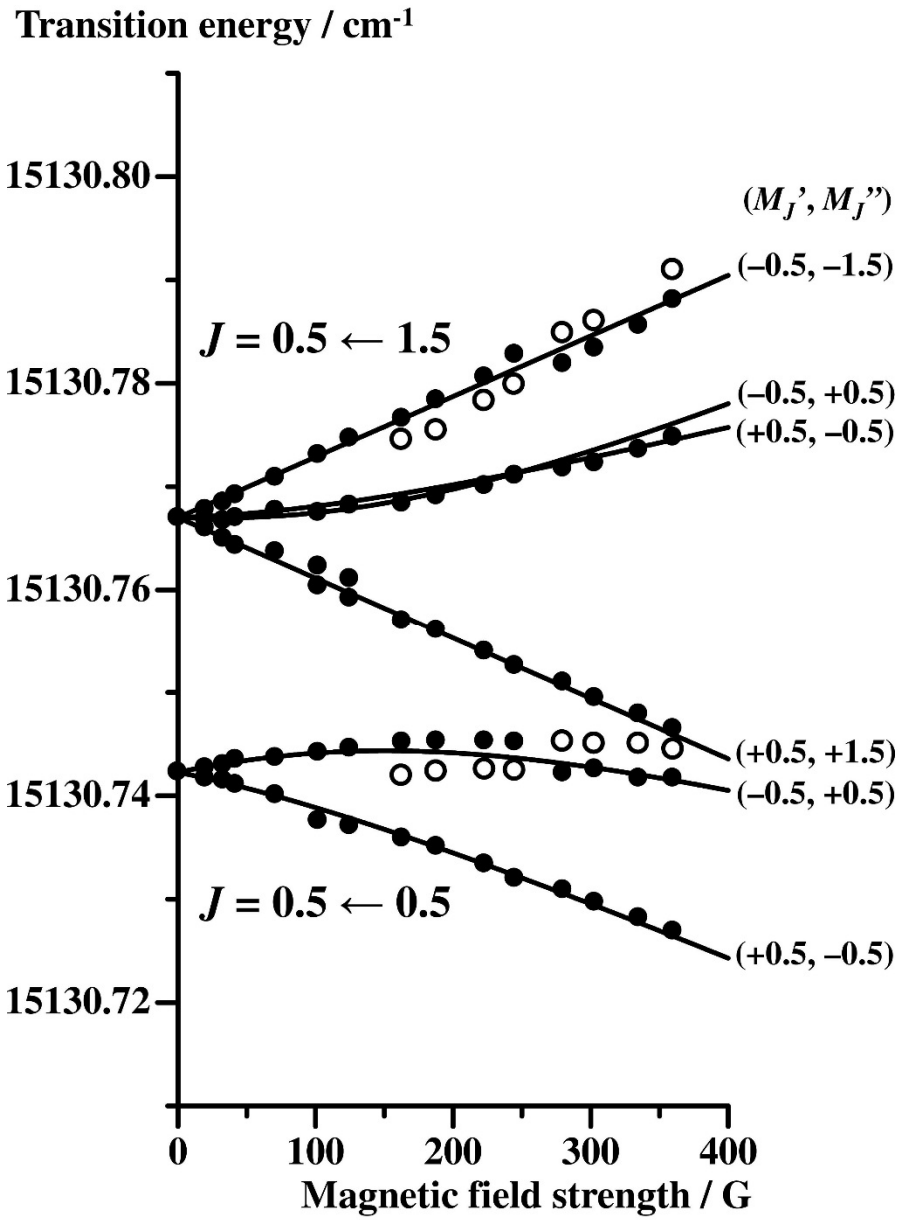

Figure 4-12. The transition energies of the observed Zeeman components at around 15130.75 cm^{-1} region for the σ-pump condition at the various magnetic field strengths are plotted by the filled circles. The blank circles indicate the transition energies to the $M_J' = –0.5$ level of the perturber. The solid lines indicate the calculated Zeeman splitting with the determined *g*-factors: $g_S = 2.020$ (fixed) for the ground state and $g_{\mathrm{eff}} = –0.725$ for this excited state.

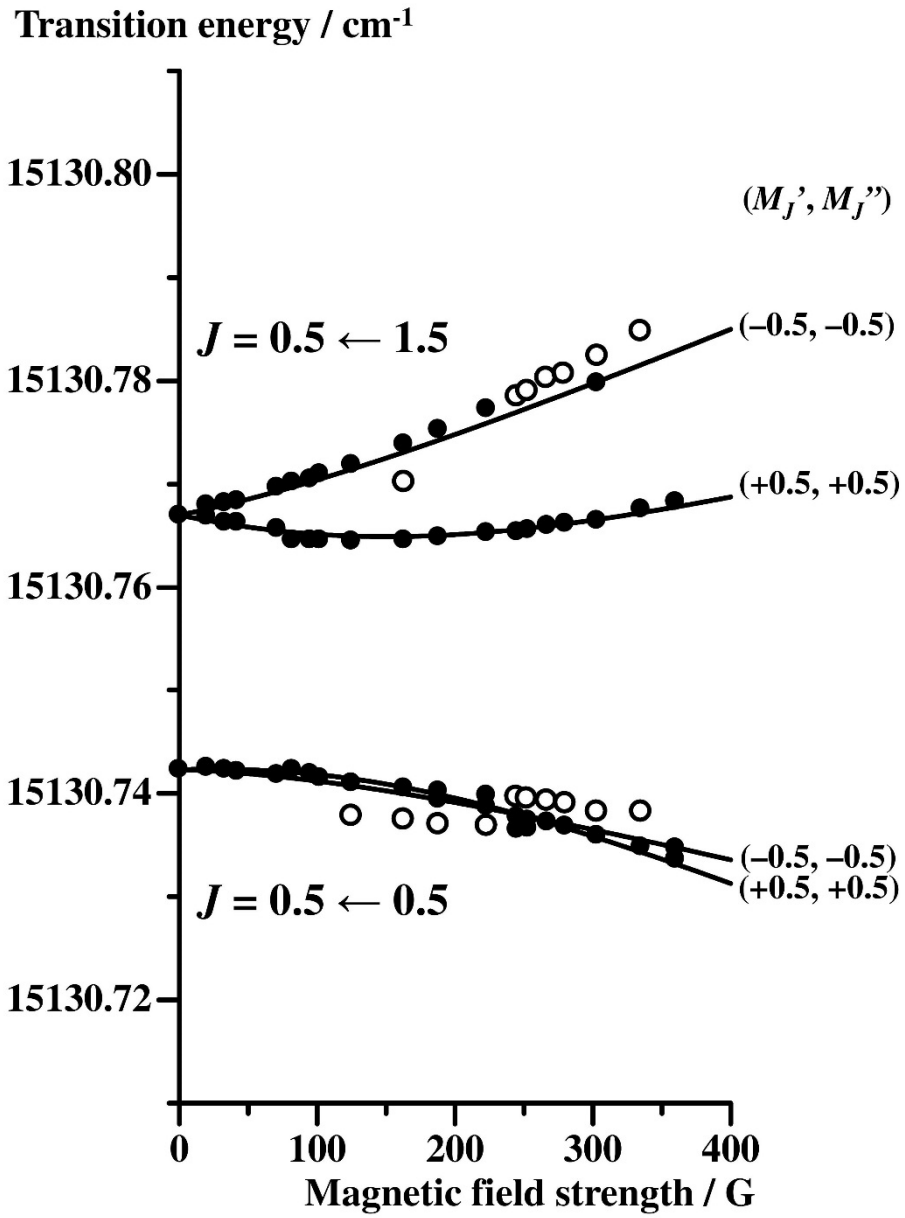

Figure 4-13. The transition energies of the observed Zeeman components at around 15130.75 cm^{-1} region for the π-pump condition at the various magnetic field strengths are plotted by the filled circles. The blank circles indicate the transition energies to the $M_J' = –0.5$ level of the perturber. The solid lines indicate the calculated Zeeman splitting with the determined *g*-factors: $g_S = 2.020$ (fixed) for the ground state and $g_{\mathrm{eff}} = –0.725$ for this excited state.

Table 4-2. The transition energies of the assigned rotational lines which belong to the $^2E'_{1/2}$ ← $\tilde{X}\,^2A_2'$ transition, the effective rotational constants of the upper states, and the determined effective *g*-factors of the $^2E'_{1/2}$ (*J'*) levels. The transition energies are in units of wavenumber. The rotational assignments whose upper *J'* is 0.5 were confirmed by the Zeeman splitting.

J'	$^rP_0(J'+1)$		$^rQ_0(J')$		$^rR_0(J'-1)$		$g_{eff}(J')$
15113.0 cm^{-1} band							
0.5	15113.0540	F_1	15113.0293	F_2	–		–1.35(13)
15113.1 cm^{-1} band							
0.5	15113.1374	F_1	15113.1129	F_2	–		–1.04(6)
15113.4 cm^{-1} band (B_{eff} = 0.502 cm^{-1})							
0.5	15113.4225	F_1	15113.3978	F_2	–		–0.81(3)
1.5	15110.3025	F_2	15114.9292	F_1	15114.9046	F_2	
15114.0 cm^{-1} band (B_{eff} = 0.502 cm^{-1})							
0.5	15113.9904	F_1	15113.9660	F_2	–		–0.59(6)
1.5	15110.8720	F_2	15115.4984	F_1	15115.4738	F_2	
15114.6 cm^{-1} band							
0.5	15114.6642	F_1	15114.6394	F_2	–		–0.74(9)
15114.8 cm^{-1} band							
0.5	15114.8049	F_1	15114.7802	F_2	–		–0.85(15)
15124.9 cm^{-1} band (B_{eff} = 0.418 cm^{-1})							
0.5	15124.9534	F_1	15124.9290	F_2	–		–0.80(7)
1.5	15121.5824	F_2	15126.2089	F_1	15126.1842	F_2	
15125.2 cm^{-1} band							
0.5	15125.2321	F_1	15125.2071	F_2	–		–0.70(13)
15126.2 cm^{-1} band (B_{eff} = 0.437 cm^{-1})							
0.5	15126.1932	F_1	15126.1685	F_2	–		–0.76(11)
1.5	15122.8793	F_2	15127.5051	F_1	15127.4811	F_2	
15128.3 cm^{-1} band (B_{eff} = 0.378 cm^{-1})							
0.5	15128.3450	F_1	15128.3198	F_2	–		–0.77(23)
1.5	15124.8526	F_2	15129.4792	F_1	15129.4548	F_2	
15129.5 cm^{-1} band							
0.5	15129.5022	F_1	15129.4771	F_2	–		–1.00(12)

Table 4-2 (continued).

J'	$^rP_0(J'+1)$		$^rQ_0(J')$		$^rR_0(J'-1)$		$g_{\text{eff}}(J')$
15129.7 cm^{-1} band (B_{eff} = 0.463 cm^{-1})							
0.5	15129.6828	F_1	15129.6580	F_2	–		–1.05(15)
1.5	15126.4450	F_2	15131.0720	F_1	15131.0473	F_2	
15129.8 cm^{-1} band (B_{eff} = 0.441 cm^{-1})							
0.5	15129.7917	F_1	15129.7669	F_2	–		–0.75(12)
1.5	15126.4887	F_2	15131.1150	F_1	15131.0902	F_2	
15130.7 cm^{-1} band (B_{eff} = 0.504 cm^{-1})							
0.5	15130.7670	F_1	15130.7423	F_2	–		–0.73(9)
1.5	15127.6369	F_2	15132.2634	F_1	15132.2381	F_2	
15131.9 cm^{-1} band (B_{eff} = 0.493 cm^{-1})							
0.5	15131.3363	F_1	15131.3115	F_2	–		–0.90(24)
1.5	15128.1880	F_2	15132.8149	F_1	15132.7902	F_2	

g_{eff} values are tabulated in Table 4-2.

Most of the rotational assignment with $J' \geq 2.5$ is still difficult, because these rotational lines were not intense enough to be observed the clear Zeeman splitting.

4.2. Discussion

The vibronic interaction

If the $\tilde{B}\,^2\text{E}'$ ($v = 0$) state was not perturbed by any vibronic states, only three rotational

line pairs with 0.0246 cm^{-1} spacing must be found in the observed spectrum as shown in Figure 4-3. However, I identified more than 20 rotational line pairs. This result indicates that the $\tilde{B}\,^2$E' (v = 0) state massively interacts with the surrounding dark vibronic states, and such vibronic states appeared by the intensity borrowing from the optically allowed $\tilde{B}$ – $\tilde{X}$ electronic transition. The candidates of the perturbing vibronic states are highly vibrationally excited states of the $\tilde{A}\,^2$E" and/or $\tilde{X}\,^2A_2$' electronic states. In order to analyze the vibronic interactions, the density of the perturbers isoenergetic with the $\tilde{B}\,^2$E' (v = 0) state is useful. When more than one e' symmetry vibrational modes are excited, such vibronic states split into substates [137,138]. We thus have to enumerate the substates which can interact with the $\tilde{B}\,^2$E' (v = 0) state.

The dark $\tilde{A}\,^2$E" state is able to interact with the $\tilde{B}\,^2$E' (v = 0) state through the a_2" symmetry vibrational modes, because the direct product of E" (electronic) and A_2" (vibrational) is E' (vibronic). Recently the frequencies of the 0 – 0 band of the $\tilde{A}$ – $\tilde{X}$ transition and the four normal vibrational modes were reported [81,139]. By using these normal vibrational frequencies of the $\tilde{A}$ state, we can estimate the number of the E'-type vibronic states originated from the $\tilde{A}\,^2$E" electronic state to be about 15, in which about 40 vibronic substates can interact with the $\tilde{B}\,^2$E' (v = 0) state, in the 15070 – 15145 cm^{-1} region: the density of the substates is ~ 0.5 states / cm^{-1}. This density is comparable with the density of the vibronic states found in the observed spectrum.

The ground $\tilde{X}\,^2A_2$' state is also able to interact with the $\tilde{B}\,^2E'$ (v = 0) state, and in this case the e' symmetry vibrational modes mediate this vibronic coupling, because the direct product of A_2' (electronic) and E' (vibrational) also leads to E' (vibronic). When we set the frequencies of the four normal vibrational modes of the $\tilde{X}\,^2A_2$' state to be ν_1 = 1050 cm^{-1}, ν_2 = 762 cm^{-1}, ν_3 = 1492 cm^{-1} and ν_4 = 365 cm^{-1} referring to the traditional vibrational assignment [48,51], we can estimate the number of the E'-type vibronic states originated from the $\tilde{X}\,^2A_2$' to be about 80, in which about 500 vibronic substates are able to interact with the $\tilde{B}\,^2E'$ (v = 0) state, in the 15070 – 15145 cm^{-1} region. When we use the lower ν_3 frequency of about 1100 cm^{-1} [59-61], the number of the E'-type vibronic states is estimated to be 100 with about 600 vibronic substates in the 15070 – 15145 cm^{-1} region. These densities of substates (6 – 8 states / cm^{-1}) is much larger than the density of states in our experimental result.

Therefore, I conclude that the complicated rotational structure of the 0 – 0 band of the $\tilde{B}\,^2E' \leftarrow \tilde{X}\,^2A_2$' transition mainly owes to the vibronic coupling between the $\tilde{A}\,^2E$" state and the $\tilde{B}\,^2E'$ state through the a_2" symmetry vibrational modes.

The spin-orbit interaction of the $\tilde{B}\,^2E'$ (v = 0) state

In this study the rotational line pairs corresponding to the $^2E'_{3/2}$ (J' = 1.5) $\leftarrow \tilde{X}\,^2A_2$' ($k$" = 0, N" = 1) transitions and the $^2E'_{1/2}$ (J' = 0.5) $\leftarrow \tilde{X}\,^2A_2$' ($k$" = 0, N" = 1) transitions have

been found in 15085 – 15103 cm^{-1} region and 15113 – 15131 cm^{-1} region, respectively. I considered the deperturbed line positions corresponding to the transitions to the lowest J' of the $^2E'_{3/2}$ and $^2E'_{1/2}$ spin-orbit components as the intensity-weighted mean positions of the rotational line pairs with the same assignments in the observed spectrum. Under this consideration, the deperturbed transition energies to the $^2E'_{3/2}$ (J' = 1.5) level and the $^2E'_{1/2}$ (J' = 0.5) level were estimated to be 15100.1 cm^{-1} and 15120.9 cm^{-1}, respectively. This about 21 cm^{-1} energy separation results from the spin-orbit interaction of the $\tilde{B}\,^2E'$ (v = 0) state. As mentioned in Section 2.2, the diagonal matrix element of the spin-orbit interaction is given by

$$\langle H_{SO} \rangle = A_{SO}\zeta_e d\Sigma = A_{SO}^{eff}\Sigma , \tag{4-3}$$

where A_{SO} is the original spin-orbit interaction constant. Therefore the 21 cm^{-1} separation between the $^2E'_{3/2}$ and $^2E'_{1/2}$ components is equal to the effective spin-orbit interaction constant; $A_{SO}^{eff} = A_{SO}\zeta_e d$, in magnitude. The sign of this interaction constant is negative, because the $^2E'_{3/2}$ spin-orbit component is lower than the $^2E'_{1/2}$ spin-orbit component in energy. Therefore the effective spin-orbit interaction constant of the $\tilde{B}\,^2E'$ (v = 0) state was estimated to be –21 cm^{-1}. This effective spin-orbit interaction constant is two orders of magnitude larger than the typical rotational constant of NO_3, $B \sim 0.5$ cm^{-1}; therefore again, it was confirmed that Hund's coupling case (a) is the appropriate limit to describe the $\tilde{B}\,^2E'$ (v = 0) state.

The determined g_{eff} of the upper $^2E'_{3/2}$ and $^2E'_{1/2}$ states were found to distribute around +0.7 and –0.8, respectively, excluding the $^2E'_{3/2}$ state located at 15102 cm^{-1}, based on the

observed Zeeman splitting. This result indicates that $g_L\zeta_e d$ is estimated to be 0.2 – 0.3 in magnitude, assuming the electronic spin *g*-factor of the excited state is similar to that of the free electron. The electronic orbital *g*-factor g_L is unity, because the excited state is ^{2}E' whose electronic orbital angular momentum is **L** = 1. Then $\zeta_e d$, which is the effective value of the molecular axial component of **L**, may be estimated as 0.2 – 0.3. By setting the effective spin-orbit interaction constant to be –21 cm^{-1} and $\zeta_e d$ to be 0.2, the original spin-orbit interaction constant of the $\tilde{B}\,^2$E' (v = 0) state can be roughly estimated to be –105 cm^{-1} (= (–21 cm^{-1}) / 0.2). This value is favorably compared with the spin-orbit interaction constants of nitrogen and oxygen atoms: 73.3 cm^{-1} and 151 cm^{-1}, respectively, in magnitude [140].

The *g*-factor of the $\tilde{X}\,^2\mathbf{A_2}$' ($v$ = 0) state

The electronic spin *g*-factor of the $\tilde{X}\,^2$A$_2$' (v = 0) state was determined to be g_S = 2.020(36) based on the Zeeman splitting of the 15100.1990 cm^{-1} and 15100.2238 cm^{-1} line pair. This value is in good agreement with the previously reported *g*-factor determined from the ESR study in H_2O/D_2O matrices: g_S = 2.0202 [141]. Theoretically, the three axial components of the *g*-tensor are related to those of the spin-rotation interaction tensor **ε** [142];

$$g_{ii} = g_e - h^2\varepsilon_{ii}I_{ii}\,, \qquad (i = a, b, c) \tag{4-4}$$

where g_e is the Landé *g*-factor of the free electron; 2.00232, h is Planck's constant, ε_{ii} is the *ii*

component of the spin-rotation interaction tensor, and I_{ii} is the *ii* component of the moment of inertia tensor **I**. In the case of this study, the above relation may be written as

$$g_S = g_e - \frac{\varepsilon_{bb}}{2B}. \quad (4\text{-}5)$$

When we use the molecular constants reported in Ref. 74 to this relationship, the theoretical g_S is derived to be 2.0202. This theoretical value also agrees with the experimental result of this study.

4.3. Conclusion

In this study, the rotationally-resolved high-resolution fluorescence excitation spectrum of jet-cooled $^{14}NO_3$ has been observed by using the N_2O_5 pyrolysis reaction: $N_2O_5 \rightarrow NO_3 + NO_2$. The observed region was 15070 – 15145 cm^{-1}, where is assigned to the 0 – 0 band of the $\tilde{B}\,^2E' \leftarrow \tilde{X}\,^2A_2'$ transition. The NO_2 contamination to the NO_3 spectrum was confirmed to be negligible in the observed region. More than 3000 rotational lines of NO_3 was found in the observed region, and they seemed to have the less rotational branch structures. Thus, the rotational assignment was difficult. However, more than 20 rotational line pairs with 0.0246 cm^{-1} spacing were identified. The Zeeman splitting observation under high-resolution and high-accurate condition is powerful tool for the unambiguous rotational assignment, because the Zeeman splitting depends on the quantum numbers of the upper and

lower levels. These rotational line pairs were successfully assigned to the transitions from the $\tilde{X}\,^2A_2'$ ($v'' = 0$, $k'' = 0$, $N'' = 1$) level, based on the Zeeman splitting and the ground state combination differences. In the observed region many vibronic bands were identified. This result indicates that the $\tilde{B}\,^2E'$ ($v = 0$) state massively interacts with the surrounding dark vibronic states, and they appeared by the intensity borrowing from the optically allowed $\tilde{B}$ – $\tilde{X}$ electronic transition. The effective molecular constants of the excited electronic states were estimated. From the density of the identified vibronic states, it was concluded that the complicated rotational structure of this 662 nm band mainly owes to the vibronic coupling between the $\tilde{B}\,^2E'$ state and the $\tilde{A}\,^2E''$ state through the a_2'' symmetry vibrational modes. The effective spin-orbit interaction constant of the $\tilde{B}\,^2E'$ ($v = 0$) state was estimated to be –21 cm^{-1}.

4.4. Publication statement

This work was published in *The Journal of Chemical Physics* as an original article entitled “High-resolution laser spectroscopy and magnetic effect of the $\tilde{B}\,^2E' \leftarrow \tilde{X}\,^2A_2'$ transition of $^{14}NO_3$ radical” under Kohei Tada, Wataru Kashihara, Masaaki Baba, Takashi Ishiwata, Eizi Hirota, and Shunji Kasahara; *J. Chem. Phys.* **141**, 184307 (2014) [143].

Chapter 5. High-resolution laser spectroscopy of $^{15}NO_3$ radical

5.1. Result and analysis

Spectral feature

The rotationally-resolved fluorescence excitation spectrum of $^{15}NO_3$ radical observed by using the $^{15}N_2O_5$ pyrolysis reaction, ranging 15080 – 15103 cm^{-1} assigned to the 0 – 0 band of the $\tilde{B}\,^2E' \leftarrow \tilde{X}\,^2A_2'$ transition, is shown in Figure 5-1 (a). When the $^{15}N_2O_5$ pyrolysis reaction is used to generate $^{15}NO_3$ radical, the $^{15}NO_2$ contamination is unavoidable. However, I ignored this $^{15}NO_2$ contamination, because the vibronic bands of $^{15}NO_2$ located at around 15100 cm^{-1} region have relatively small intensity [144,145]. In the case of $^{14}NO_3$, we confirmed that the $^{14}NO_2$ contamination can be ignored in 15100 cm^{-1} region by observing the pure $^{14}NO_2$ spectrum [143]. Then it was considered that all of the observed rotational lines in the observed region originate from $^{15}NO_3$ radical. In the 15080 – 15103 cm^{-1} region, about 200 strong lines and several thousand weak lines were found. Intense rotational lines seem to be concentrated in 15094 – 15102 cm^{-1} region. Portions of the observed spectrum (1 cm^{-1} and 0.15 cm^{-1} region) are magnified in Figures 5-1 (b) and (c), respectively. Typical linewidth of each rotational line was about 25 MHz in full width at half maximum, which is mainly due

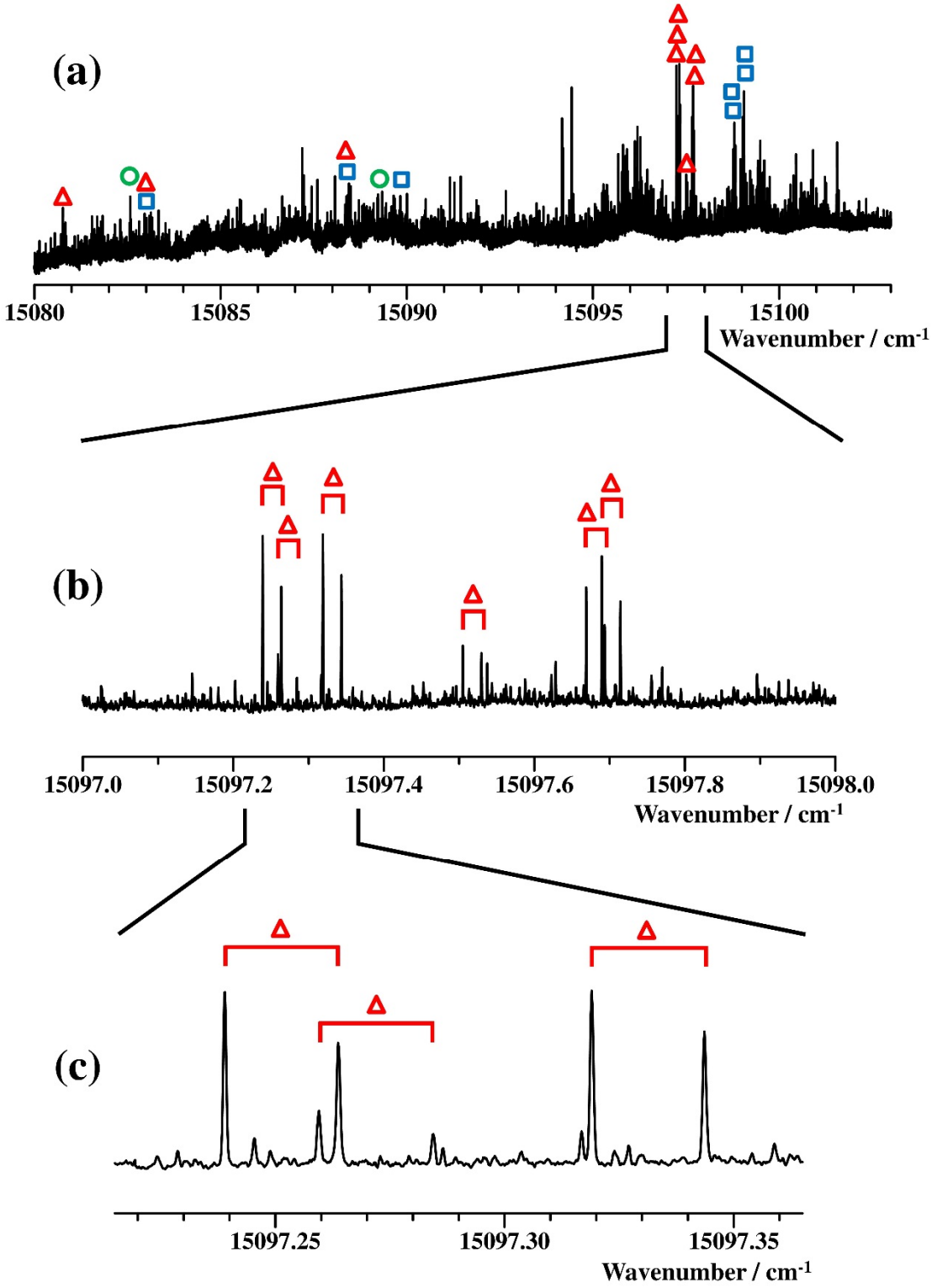

Figure 5-1. Fluorescence excitation spectrum of $^{15}NO_3$ for (a) 15080 – 15103 cm^{-1} (23 cm^{-1}) region, (b) 15097 – 15098 cm^{-1} (1 cm^{-1}) region, and (c) 15097.215 – 15097.365 cm^{-1} (0.15 cm^{-1}) region. The rotational line pairs assigned to the transitions to the $^2E'_{3/2}$ (J' = 1.5), $^2E'_{1/2}$ (J' = 0.5) and $^2E'_{1/2}$ (J' = 1.5) levels, whose assignments were confirmed by the Zeeman splitting, are indicated by the circles, triangles and squares, respectively.

to the residual Doppler width and the frequency jitter of the dye laser. I could not resolve any ^{15}N hyperfine structures with the spectral resolution of this study.

Zeeman effect observation and rotational assignment

To tell the result first, I clearly assigned only the rotational lines corresponding to the $k = 1 \leftarrow 0$ transition in this $^{15}NO_3$ study. Therefore, hereafter we focus on such transitions. As already mentioned in the previous chapter, the rotational energies of the spin components in the $k = 0$ stack in the ground state are given by

$$E(N)_{F_1} = BN(N+1) - D_N N^2 (N+1)^2 + \frac{\varepsilon_{bb}}{2} N , \quad (5\text{-}1)$$

$$E(N)_{F_2} = BN(N+1) - D_N N^2 (N+1)^2 - \frac{\varepsilon_{bb}}{2} (N+1) . \quad (5\text{-}2)$$

On the other hand the rotational energy of the $k = 1$ stack of the $\tilde{B}$ state may be expressed as

$$E(J) = T_0 + BJ(J+1) - D_J J^2 (J+1)^2 , \quad (5\text{-}3)$$

from Equation (2-4). Here, T_0 is the effective band origin including k' dependent terms, B is the effective rotational constant and D_J is the first-order centrifugal distortion constant.

Similarly to the $^{14}NO_3$ study, I started the assignment from the rotational line pairs with the lowest quantum numbers. From the latest molecular constants [74], the spin-rotation splitting of the $\tilde{X}\,^2A_2$' (v" = 0, k" = 0, N" = 1, J" = 0.5 and 1.5) levels was calculated to be 0.0237 cm^{-1}. In the observed spectrum, I recognized many rotational line pairs with about

0.0248 cm^{-1} spacing. These line pairs were assigned to the three types of transition from the $\tilde{X}\ ^2A_2$' (v" = 0, k" = 0, N" = 1, J" = 0.5 and 1.5) levels to the $^2E'_{3/2}$ (P' = 1.5, J' = 1.5), $^2E'_{1/2}$ (P' = 0.5, J' = 0.5), or $^2E'_{1/2}$ (P' = 0.5, J' = 1.5) excited level. To discriminate these transitions from each other clearly, the Zeeman splitting was observed.

Figure 5-2 shows three types of the observed Zeeman splitting of the rotational line pairs with 0.0248 cm^{-1} spacing for the σ-pump condition with the external magnetic field strength H = 70 G. The selection rule of the σ-pump condition is $\Delta M_J = \pm 1$. Figure 5-2 (a) shows that the rotational line pair splits into four and six components by an external magnetic field. From this Zeeman splitting, this rotational line pair was assigned to $^rR_0(0.5)$ and $^rQ_0(1.5)$ of the $^2E'_{3/2} \leftarrow \tilde{X}\ ^2A_2$' transition. Here, we adopt the nomenclature $^{\Delta k}\Delta J_{k"}(J")$ for labeling the rotational lines of $^{15}NO_3$. Two rotational line pairs in Figure 5-2 (b) seem to split into two and three Zeeman components. Thus they were assigned to $^rQ_0(0.5)$ and $^rP_0(1.5)$ of the $^2E'_{1/2} \leftarrow \tilde{X}\ ^2A_2$' transitions, respectively. These two types of the Zeeman splitting have been reported in our previous study of $^{14}NO_3$ (See Figures 4-4 and 4-10 in the previous chapter) [143]. Two rotational line pairs in Figure 5-2 (c) also split into four and six components, but the Zeeman pattern is different from that in Figure 5-2 (a). This result indicates that the quantum numbers of the upper levels are the same (J' = 1.5), but g_{eff} values of the upper levels are different from each other. The Zeeman splitting in Figure 5-2 (c) can be explained when these rotational line pairs are assigned to $^rR_0(0.5)$ and $^rQ_0(1.5)$ of the $^2E'_{1/2} \leftarrow \tilde{X}\ ^2A_2$' transition.

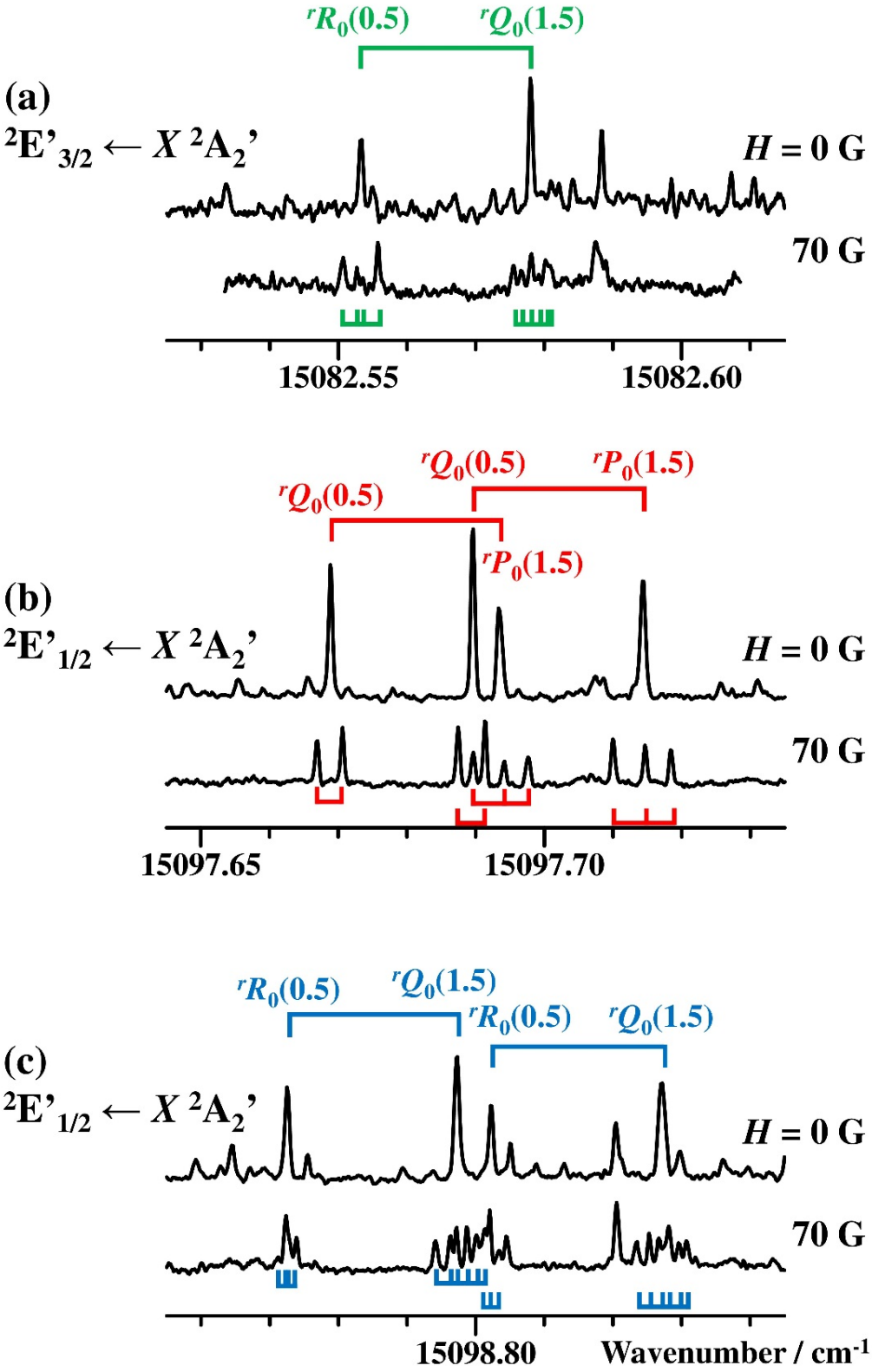

Figure 5-2. Three types of the Zeeman splitting of the line pairs with 0.0248 cm^{-1} spacing for the σ-pump condition, where the magnetic field vector is perpendicular to the polarization of the incident laser beam. (a) Transition to the $^2E'_{3/2}$ (J' = 1.5) level. (b) Transition to the $^2E'_{1/2}$ (J' = 0.5) level. (c) Transition to the $^2E'_{1/2}$ (J' = 1.5) level.

From the observed Zeeman splitting, I finally confirmed that 18 line pairs with 0.0248 cm^{-1} spacing correspond to the transitions from the $\tilde{X}\,^2A_2'$ (v'' = 0, k'' = 0, N'' = 1, J'' = 0.5 and 1.5) levels, in which two, nine, and seven pairs were assigned to the transitions to the $^2E'_{3/2}$ (J' = 1.5), $^2E'_{1/2}$ (J' = 0.5), and $^2E'_{1/2}$ (J' = 1.5) excited levels, respectively. They are shown in Figure 5-1, where the circles, the triangles, and the squares indicate the line pairs assigned to the transitions to the $^2E'_{3/2}$ (J' = 1.5), $^2E'_{1/2}$ (J' = 0.5), and $^2E'_{1/2}$ (J' = 1.5) levels, respectively.

The Zeeman splitting of the rotational line pairs was observed up to 360 G to determine the g_{eff} values of the excited levels. As an example, Figure 5-3 shows the observed Zeeman splitting for the σ-pump condition of the rotational line pairs at 15097.7 cm^{-1} region, where the $^rQ_0(0.5)$ and $^rP_0(1.5)$ line pairs of the $^2E'_{1/2} \leftarrow \tilde{X}\,^2A_2'$ transitions appeared, as shown in Figure 5-2 (b). In an analogous way to our previous study on $^{14}NO_3$ [143], the effective g-factors of the excited levels were determined as g_{eff} (= $g_L\zeta_e d - g_S/2$) = –0.48(18) for the 15097.6689 cm^{-1} and 15097.6933 cm^{-1} line pair, and g_{eff} = –0.95(6) for the 15097.6897 cm^{-1} and 15097.7143 cm^{-1} line pair. During the analysis, the g_S value of the ground state was fixed to 2.020 based on the Curl's relationship [142]; $g_S = g_e - (\varepsilon_{bb}/2B)$, because this relationship was confirmed in our previous study [143] and the ESR study [141] to hold in the ground state of $^{14}NO_3$. Here, g_e denotes the Landé g-factor of the free electron (g_e = 2.00232) and B is the rotational constant. In similar way, the g_{eff} values of the excited rovibronic levels were determined as listed in Table 5-1.

Table 5-1. Assigned rotational lines and the determined g_{eff} values of the upper levels. The rotational assignments with g_{eff} values were confirmed by the Zeeman splitting. B is the effective rotational constant of the upper vibronic state. Number in parentheses denotes the standard deviation. Transition energies of $^rP_0(J'+1)$, $^rQ_0(J')$, and $^rR_0(J'-1)$ lines are in units of wavenumber.

J'	$^rP_0(J'+1)$		$^rQ_0(J')$		$^rR_0(J'-1)$		$g_{\mathrm{eff}}(J')$
$^2E'_{3/2} \leftarrow \tilde{X}\ ^2A_2'$ transition							
15081.9 cm^{-1} band (B = 0.421 cm^{-1})							
1.5	[a]		15082.5781	F_1	15082.5533	F_2	+0.73(12)
2.5	15080.1161	F_1	15080.0587	F_2	15084.6855	F_1	
15088.6 cm^{-1} band (B = 0.419 cm^{-1})							
1.5	15084.6049	F_2	15089.2326	F_1	15089.2076	F_2	+0.64(14)
2.5	15086.7115	F_1	15086.6536	F_2	15091.2809	F_1	
3.5	15081.3547	F_2	15089.6829	F_1	15089.6249	F_2	
$^2E'_{1/2} \leftarrow \tilde{X}\ ^2A_2'$ transition							
15081.4 cm^{-1} band (B = 0.448 cm^{-1})							
0.5	15080.8005	F_1	15080.7757	F_2	–		–0.23(13)
1.5	[a]		15082.1436	F_1	15082.1191	F_2	
15082.3 cm^{-1} band (B = 0.416 cm^{-1})							
0.5	15081.7438	F_1	15081.7198	F_2	–		
1.5	[a]		15082.9934	F_1	15082.9686	F_2	[b]
15083.5 cm^{-1} band (B = 0.526 cm^{-1})							
0.5	15083.0102	F_1	15082.9856	F_2	–		[b]
1.5	[a]		15084.5894	F_1	15084.5650	F_2	
15087.6 cm^{-1} band (B = 0.469 cm^{-1})							
0.5	15087.0407	F_1	15087.0160	F_2	–		
1.5	15083.8193	F_2	15088.4466	F_1	15088.4217	F_2	–0.20(18)
15089.0 cm^{-1} band (B = 0.461 cm^{-1})							
0.5	15088.3757	F_1	15088.3509	F_2	–		–0.52(23)
1.5	15085.2015	F_2	15089.8284	F_1	15089.8039	F_2	[b]

Table 5-1 (continued).

J'	$^rP_0(J'+1)$		$^rQ_0(J')$		$^rR_0(J'-1)$		$g_{\mathrm{eff}}(J')$
15098.2 cm^{-1} band (B = 0.428 cm^{-1}) [c]							
0.5	15097.2637	F_1	15097.2389	F_2	–		–1.43(21)
0.5	15097.2845	F_1	15097.2595	F_2	–		–1.00(17)
0.5	15097.3436	F_1	15097.3190	F_2	–		–0.98(9)
0.5	15097.5296	F_1	15097.5050	F_2	–		+0.34(19)
0.5	15097.6933	F_1	15097.6689	F_2	–		–0.48(18)
0.5	15097.7143	F_1	15097.6897	F_2	–		–0.95(6)
1.5	15094.1707	F_2	15098.7973	F_1	15098.7725	F_2	–1.41(28)
1.5	15094.2003	F_2	15098.8272	F_1	15098.8022	F_2	–1.66(29)
1.5	15094.4285	F_2	15099.0551	F_1	15099.0302	F_2	–0.83(13)
1.5	15094.4699	F_2	15099.0968	F_1	15099.0718	F_2	–1.20(27)
2.5	15096.1829	F_1	15096.1255	F_2	15100.7529	F_1	
2.5	15096.3485	F_1	15096.2910	F_2	15100.9183	F_1	
3.5	15091.1589	F_2	15099.4869	F_1	15099.4291	F_2	
4.5	15095.1751	F_1	15095.0833	F_2	[a]		
5.5	15087.1937	F_2	15099.2226	F_1	15099.1308	F_2	
6.5	15092.5757	F_1	15092.4491	F_2	[a]		
7.5	15082.1647	F_2	15097.8958	F_1	15097.7698	F_2	
8.5	15088.8691	F_1	15088.7100	F_2	[a]		
9.5	[a]		15095.9144	F_1	15095.7552	F_2	
10.5	15083.5264	F_1	15083.3351	F_2	15102.7638	F_1	

[a] Out of the observed region.

[b] In these upper J' levels, g_{eff} is close to zero. Then, the effective g-factors could not be determined precisely.

[c] Six line pairs with J' = 0.5, four sets of lines with J' = 1.5, and two sets of lines with J' = 2.5 were considered to belong to a single vibronic band. See text.

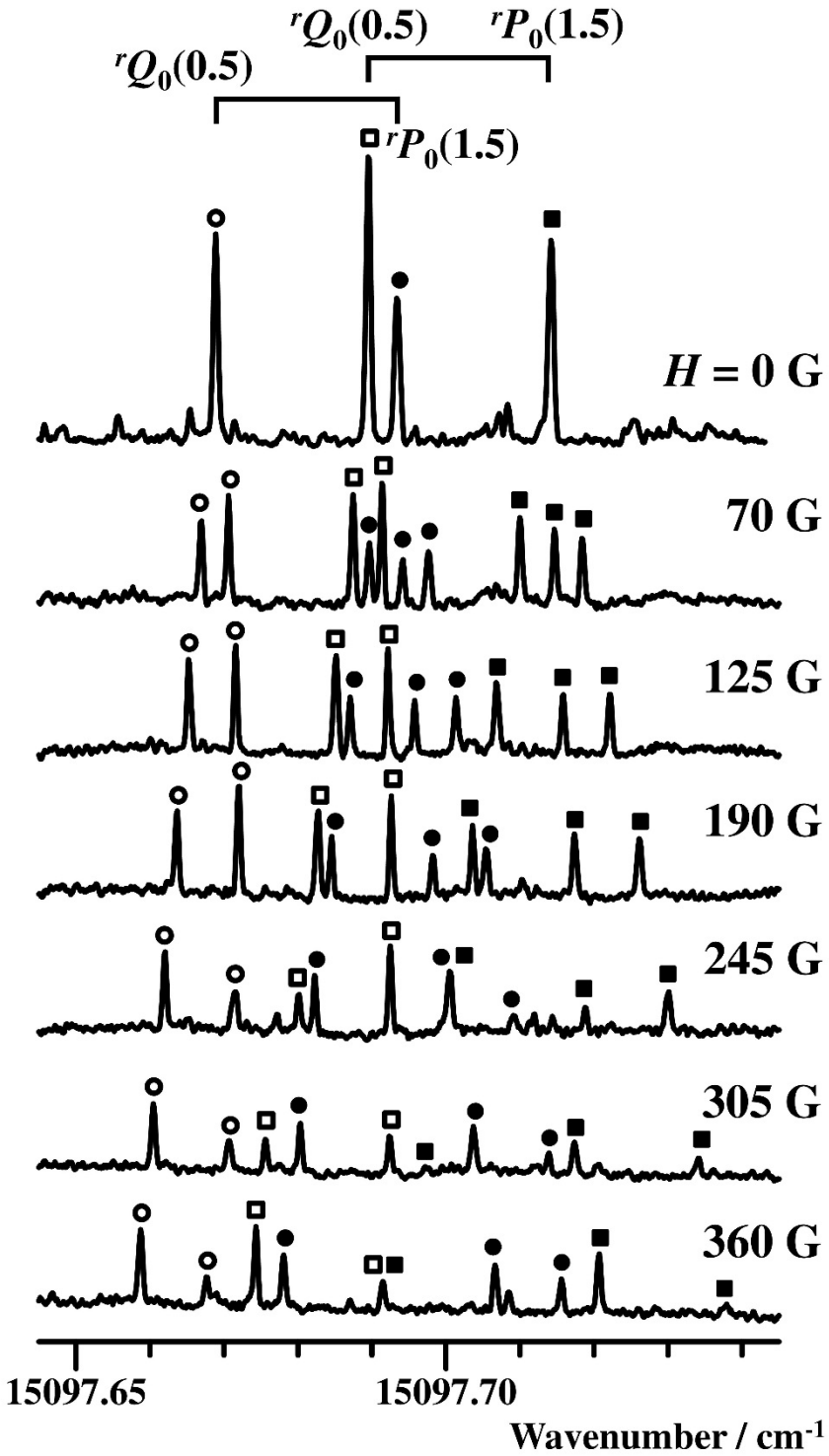

Figure 5-3. Fluorescence excitation spectrum of $^{15}NO_3$ at around 15097.7 cm^{-1} and its variation with the magnetic field strength H up to 360 G for the σ-pump condition. Blank circles, blank squares, filled circles, and filled squares indicate the Zeeman components originating from the 15097.6689 cm^{-1}, 15097.6897 cm^{-1}, 15097.6933 cm^{-1}, and 15097.7143 cm^{-1}, respectively.

Six intense pairs of $^{r}Q_0(0.5)$ and $^{r}P_0(1.5)$ and four intense pairs of $^{r}R_0(0.5)$ and $^{r}Q_0(1.5)$ were closely found at around 15097.5 cm^{-1} and 15098.9 cm^{-1}, respectively. The $^{r}P_0(2.5)$ line was expected to lie about 4.603 cm^{-1} below the $^{r}R_0(0.5)$ line from the ground state combination differences [74], and then four $^{r}P_0(2.5)$ lines were found at 4.6018 ± 0.0001 cm^{-1} below the four $^{r}R_0(0.5)$ lines. This assignment was confirmed by the Zeeman splitting. As the example, the Zeeman splitting of the rotational lines located at 15094.1707 cm^{-1} and 15094.2003 cm^{-1} for the σ-pump condition is shown in Figure 5-4. The observed Zeeman splitting is consistent with the rotational assignment to $^{r}P_0(2.5)$. These intense rotational lines with J' = 0.5 (six pairs) and J' = 1.5 (four sets) seem to belong to a single vibronic band with the regular rotational branch structure, and the individual rotational lines seem to *accidentally split* into several lines with the same assignments. The *accidental splitting* may originate from the vibronic coupling between the bright $\tilde{B}\,^2E'_{1/2}$ (v = 0) state and the surrounding dark vibronic state(s). Finally for this most intense band, 50 rotational lines of J' ranging from 0.5 up to 10.5 were assigned by using the ground state combination differences. When characteristic Zeeman splitting was observed, it was used to confirm the rotational assignment. Figure 5-5 shows the observed Zeeman splitting of a rotational line located at 15096.1255 cm^{-1}, as an example of the characteristic Zeeman splitting. This rotational line shows the *Bell-shape* Zeeman splitting for the σ-pump condition, and this is consistent with the rotational assignment to $^{r}Q_0(2.5)$. The assigned rotational lines of $^{15}NO_3$ are also listed in Table 5-1.

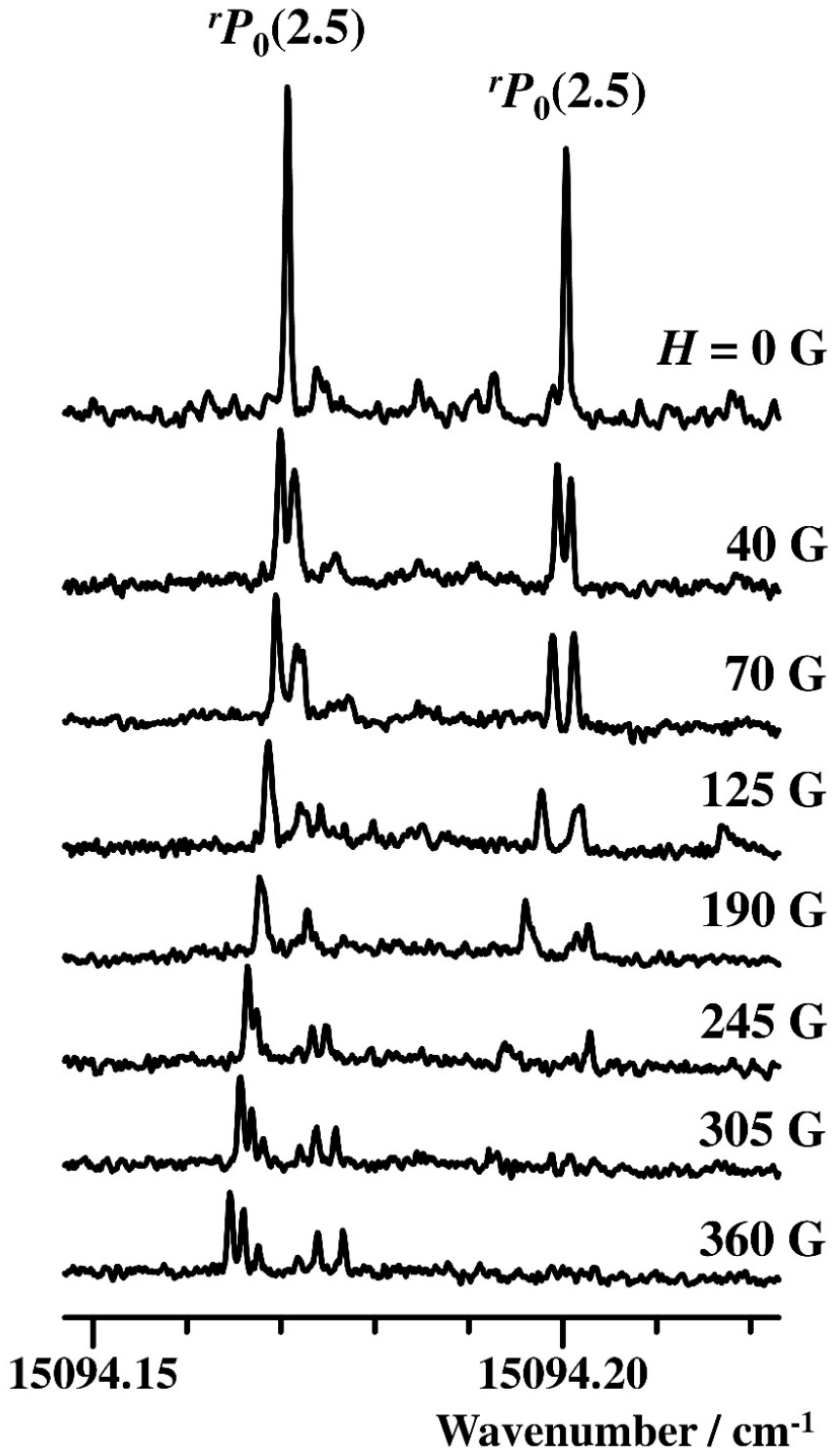

Figure 5-4. Fluorescence excitation spectrum of $^{15}NO_3$ at around 15094.2 cm^{-1}, and its variation with the magnetic field strength H up to 360 G for the σ-pump condition. The *M-shape* Zeeman splitting is consistent with the $^rP_0(2.5)$ rotational assignment.

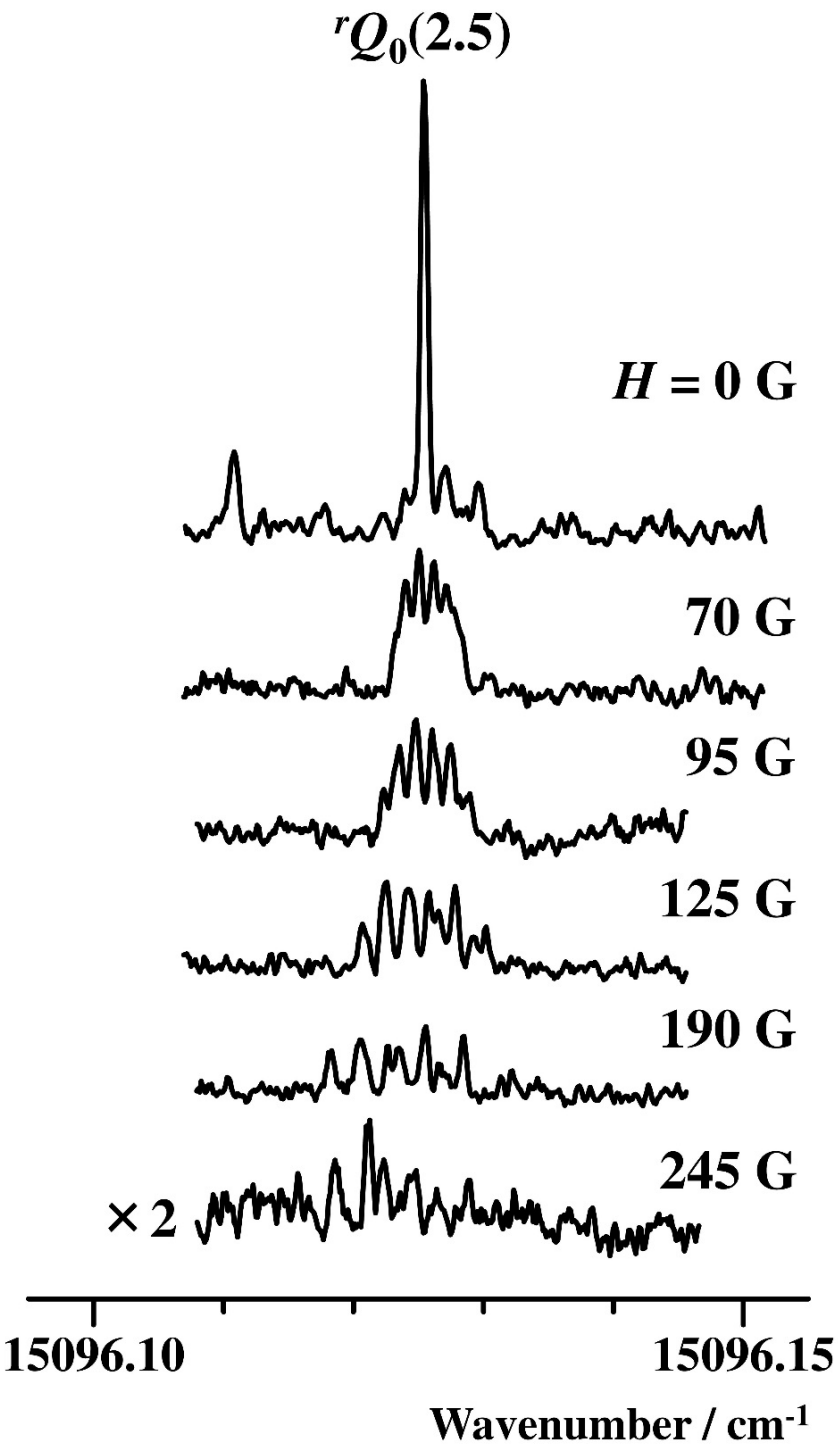

Figure 5-5. Fluorescence excitation spectrum of $^{15}NO_3$ at around 15096.1 cm^{-1}, and its variation with the magnetic field strength H up to 245 G for the σ-pump condition. The *Bell-shape* Zeeman splitting is consistent with the $^{r}Q_0(2.5)$ rotational assignment.

From this rotational assignment, the ground state molecular constants were determined as B = 0.458544(2) cm^{-1}, D_N = 0.56(2) × 10^{-6} cm^{-1}, and ε_{bb} = –0.01670(4) cm^{-1} by using Equations (5-1) and (5-2) by the least-squares fitting. The standard deviation was 0.0005 cm^{-1}, which is slightly larger than our experimental accuracy but within an acceptable range. The molecular constants of the excited state were estimated to be T_0 = 15098.20(4) cm^{-1}, B = 0.4282(7) cm^{-1}, and D_J = 4 × 10^{-4} cm^{-1} by using Equation (5-3), under a perturbation-free assumption, in which the original line positions were defined by the intensity-weighted line positions with the same assignments and the original line intensities were defined by the sums of the line intensities with the same assignments. This most intense band was considered as the original $\tilde{B}\,^2\mathrm{E}'_{1/2}$ (v' = 0) ← $\tilde{X}\,^2\mathrm{A}_2'$ (v'' = 0) transition and named the 15098.2 cm^{-1} band after its band origin. Figure 5-6 shows a comparison among the observed, the deperturbed, and the calculated spectra of this 15098.2 cm^{-1} band. The observed fluorescence excitation spectrum is shown in Figure 5-6 (a), where the marked rotational lines were assigned to the k = 1 ← 0 transition of the 15098.2 cm^{-1} band. The same marks indicate the transitions to the rotational levels with the same J', e.g., the rotational lines with the circles were assigned to $^rR_0(1.5)$, $^rQ_0(2.5)$ and $^rP_0(3.5)$ with J' = 2.5. Figure 5-6 (b) shows the *unperturbed* spectrum of the k = 1 ← 0 transition in the 15098.2cm^{-1} band, obtained from the perturbation-free assumption. Figure 5-6 (c) is the calculated spectrum of the 15098.2 cm^{-1} band by using the Hönl-London factors listed in Table 2-2 and the determined molecular constants. The

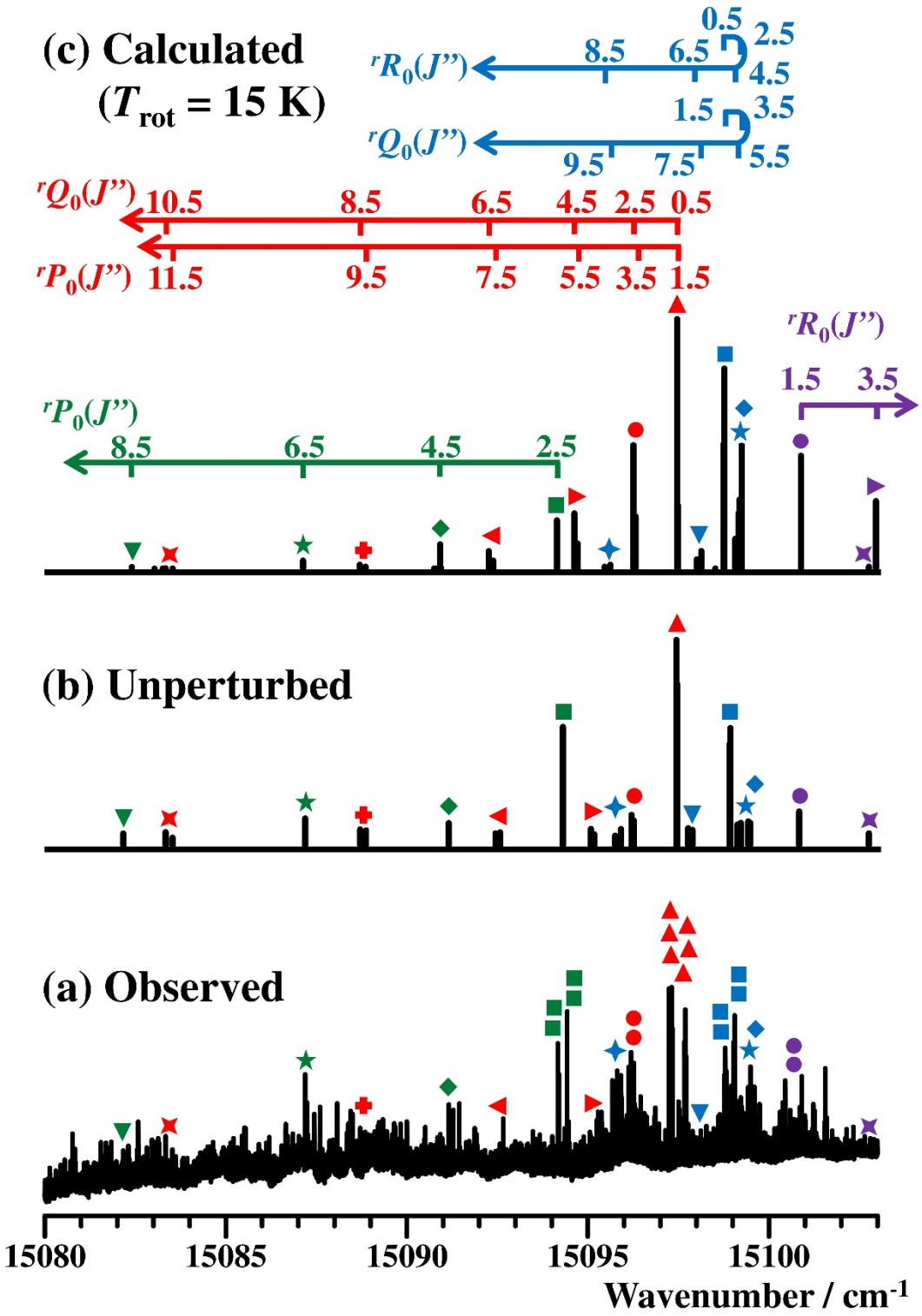

Figure 5-6. The comparison between the observed spectrum and the calculated spectrum. (a) The observed spectrum, (b) the unperturbed spectrum for the $k = 1 \leftarrow 0$ stack of the 15098.2 cm^{-1} band, and (c) the calculated spectrum for the $k = 1 \leftarrow 0$ stack of the 15098.2 cm^{-1} band at the rotational temperature of 15 K with the determined molecular constants. The same marks indicate the transitions to the rotational levels with the same upper J'.

rotational temperature was estimated to be 15 K from the intensity distribution of the unperturbed rotational lines. The calculated spectrum agrees quite well with the unperturbed one.

In the observed region of 15080 – 15103 cm^{-1}, I identified additional vibronic bands, whose rotational lines were assigned by the ground state combination differences and the Zeeman splitting. These bands were also named after their band origins, and the assigned lines are also listed in Table 5-1.

The rotational assignment for $k" \neq 0$ levels based on the ground state combination differences seems to be possible. However, it is difficult to confirm these assignments because most of the observed rotational lines were not intense enough to observe Zeeman splitting clearly. In addition, it is difficult to make rotational assignment for rotational lines, because of too many perturbations in excited electronic states.

5.2. Discussion

Eight vibronic transitions were identified in the observed spectrum, while only one vibronic 0 – 0 band had been expected to appear. This result indicates that the $\tilde{B}\,^2E'$ ($v = 0$) state is strongly perturbed by the surrounding dark vibronic states in the form of the energy shifts of the rotational lines as well as the intensity borrowing. The candidates of the

perturbers are the highly vibrationally excited states of the $\tilde{A}$ and $\tilde{X}$ electronic states, then the a_2" and e' symmetry vibrational modes mediate the vibronic interactions with the $\tilde{A}^2$E" states and the $\tilde{X}\,^2A_2$' states, respectively. In order to analyze the vibronic interactions, the density of the perturber levels at the energy of the $\tilde{B}$ ($v = 0$) state is useful. The frequencies of the v_1, v_2, and v_4 vibrational modes in the $\tilde{A}^2$E" state of the $^{15}NO_3$ isotopologue in neon matrix can be estimated to be 770 cm^{-1}, 650 cm^{-1}, and 510 cm^{-1}, respectively, from the result by Jacox and Thompson [82]; however, those frequencies in a gas phase are not reported yet. I thus assumed that there is not so much of a difference between $^{14}NO_3$ and $^{15}NO_3$ in terms of the vibrational frequencies of the $\tilde{A}^2$E" and $\tilde{X}\,^2A_2$' states by ignoring the vibrational isotope shifts, as the lowest-order assumption. Under this rough assumption, the densities of the perturbers originated from the $\tilde{A}$ and $\tilde{X}$ states at the energy of the $\tilde{B}$ ($v = 0$) state can be estimated to be 0.5 states / cm^{-1} and 7 states / cm^{-1}, respectively. The former estimated density is comparable with the observed density of vibronic bands in the spectrum. Additionally, the latter estimated density is comparable with the density of the *accidental split* rotational lines with lower *J'* of the 15098.2 cm^{-1} band. Therefore, we can conclude that the $\tilde{B}^2$E' ($v = 0$) state interacts with not only the $\tilde{A}^2$E" state but also the $\tilde{X}\,^2A_2$' state. In the $^{14}NO_3$ study in the previous chapter, I concluded that the vibronic coupling between the $\tilde{B}^2$E' ($v = 0$) state and the $\tilde{A}^2$E" state, not the $\tilde{X}\,^2A_2$' state, is mainly responsible for the complexity of the observed spectrum. The variation in the curvature of the potential energy surfaces of the low-

lying electronic states caused by the vibrational isotope effect may lead to the variation between $^{14}NO_3$ and $^{15}NO_3$ in the strength of the intra-molecular interactions.

In contrast to $^{14}NO_3$ [143], I successfully carried out the rotational analysis of the observed spectrum of $^{15}NO_3$. The determined constants of the $\tilde{X}\,^2A_2'$ ($v = 0$) state are B = 0.458544(2) cm^{-1}, $D_N = 0.56(2) \times 10^{-6}$ cm^{-1}, and ε_{bb} = –0.01670(4) cm^{-1}. These values are close to the recently reported ones of $^{15}NO_3$ in Ref. 74, except the ε_{bb}. The ε_{bb} value of this study is rather consistent with those of the recent study of $^{14}NO_3$ [74] and the previous study of $^{15}NO_3$ [72]. This result suggests that the previously reported ε_{bb} constant [74] may not be able to reproduce the actual (experimental) spin-rotation splitting of the ground state. Further high-resolution spectroscopic study of the ground state may be needed.

As already mentioned above, I considered the most intense 15098.2 cm^{-1} band as the original $\tilde{B}\,^2E'_{1/2} \leftarrow \tilde{X}\,^2A_2'$ transition. On the other hand, the $^2E'_{3/2} \leftarrow \tilde{X}\,^2A_2'$ transitions were identified at 15081.9 cm^{-1} and 15088.6 cm^{-1}. When we assume the position of the original $\tilde{B}\,^2E'_{3/2} \leftarrow \tilde{X}\,^2A_2'$ transition to be the intensity-weighted position of these two vibronic bands, we obtain the transition energy as 15085.5 cm^{-1}. This 12 cm^{-1} energy separation between the $\tilde{B}\,^2E'_{1/2} \leftarrow \tilde{X}\,^2A_2'$ and the $\tilde{B}\,^2E'_{3/2} \leftarrow \tilde{X}\,^2A_2'$ transitions results from the spin-orbit interaction in the $\tilde{B}\,^2E'$ ($v = 0$) state. From this energy separation we can estimate the effective spin-orbit interaction constant to be –12 cm^{-1}, which is somewhat smaller in magnitude than that of $^{14}NO_3$ radical; –21 cm^{-1} [143]. In the 15080 – 15103 cm^{-1}region,

the transition intensity to the $^2E'_{3/2}$ spin-orbit component was found to be much smaller than that to the $^2E'_{1/2}$ spin-orbit component. Then, if the original $\tilde{B}\,^2E'_{3/2} \leftarrow \tilde{X}\,^2A_2'$ transition is identified below 15080 cm^{-1}, the effective spin-orbit interaction constant of the $\tilde{B}\,^2E'$ ($v = 0$) state may become larger in magnitude, and it may approach the interaction constant of $^{14}NO_3$ isotopologue. Thus, we should regard the effective spin-orbit interaction constant –12 cm^{-1} estimated from this study as the lower limit of this constant in magnitude.

5.3. Conclusion

In the present study, rotationally-resolved high-resolution fluorescence excitation spectrum of jet-cooled $^{15}NO_3$ radical was observed in the 15080 – 15103 cm^{-1} region assigned to the 0 – 0 band of the $\tilde{B}\,^2E' \leftarrow \tilde{X}\,^2A_2'$ transition. This is the first high-resolution spectroscopic study of the $\tilde{B} \leftarrow \tilde{X}$ electronic transition of $^{15}NO_3$ radical. The observed spectrum consists of about 200 strong lines and several thousand weak lines. The $^{15}NO_2$ contamination to the $^{15}NO_3$ spectrum was assumed to be negligible in the observed region referring to the $^{14}NO_3$ study. I recognized many rotational line pairs with 0.0248 cm^{-1} spacing. Eighteen pairs of them were successfully assigned to the transitions from the $\tilde{X}\,^2A_2'$ ($v'' = 0$, $k'' = 0$, $N'' = 1$, $J'' = 0.5$ and 1.5) levels based on the Zeeman splitting and the ground state combination differences. Starting from these line pairs, 90 rotational lines were finally

assigned. The molecular constants of the $\tilde{B}\,^2\mathrm{E}'_{1/2}$ state were estimated to be T_0 = 15098.20(4) cm^{-1}, B = 0.4282(7) cm^{-1}, and $D_J = 4 \times 10^{-4}$ cm^{-1}. Eight vibronic bands were identified in 15080 – 15103 cm^{-1} region. This spectral structure was concluded to be due to the vibronic coupling between the $\tilde{B}\,^2\mathrm{E}'$ (v = 0) state and the $\tilde{X}$ and $\tilde{A}$ electronic states. Both two spin-orbit components $^2\mathrm{E}'_{1/2}$ and $^2\mathrm{E}'_{3/2}$ were identified in the observed region, and the lower limit of the effective spin-orbit interaction constant of the $\tilde{B}\,^2\mathrm{E}'$ (v = 0) state was estimated to be –12 cm^{-1} based on the energy separation of these spin-orbit components.

5.4. Publication statement

This work was submitted to *The Journal of Chemical Physics* as an original article under Kohei Tada, Kanon Teramoto, Takashi Ishiwata, Eizi Hirota, and Shunji Kasahara.

Summary

In this doctoral dissertation I have reported the rotationally-resolved high-resolution laser spectroscopic study and the Zeeman effect observation of the electronic transition of NO_3 radical in the visible region.

As the introduction of this dissertation, the Born-Oppenheimer approximation, the degrees of freedom of motions in a molecule, and the free radicals were reviewed briefly in Chapter 1. Then the numerous papers of NO_3 were introduced to describe the current situation of this radical.

In Chapter 2, the theoretical treatment of NO_3 radical was described mainly based on the theory of angular momentum. The derived equations are indispensable to analyze the rotationally-resolved high-resolution spectra of NO_3 and their magnetic effect appropriately. Then, the intensity borrowing mechanism was introduced by using the fundamental perturbation theory. Several types of line broadening effect were shortly described.

In Chapter 3, the principles and procedures of high-resolution laser spectroscopic method were described. NO_3 radical was generated by the pyrolysis reaction of N_2O_5. A single-mode ring dye laser, which is a tunable laser with a narrow energy linewidth, was applied as the light source. The molecular beam method was used to reduce the Doppler width and to cool the molecules by the adiabatic expansion. A pair of solenoids was used to observe an

external magnetic effect. A Doppler-free spectrum of iodine and a fringe pattern of an étalon were recorded for the absolute wavenumber calibration in the accuracy of 0.0001 cm^{-1}.

In Chapter 4, the high-resolution laser spectroscopy of $^{14}NO_3$ isotopologue was reported. Rotationally-resolved fluorescence excitation spectrum was observed in 15070 – 15145 cm^{-1} region assigned to the 0 – 0 band of the $\tilde{B}\,^2E' \leftarrow \tilde{X}\,^2A_2'$ transition. The NO_2 contamination to the NO_3 spectrum was confirmed to be negligible in the observed region. More than 3000 rotational lines of NO_3 were found, and they seemed to have less the rotational branch structures. In the observed region more than 20 intense rotational line pairs with 0.0246 cm^{-1} spacing were identified. This spacing is the same with the spin-rotation splitting of the $\tilde{X}\,^2A_2'$ ($v'' = 0$, $k'' = 0$, $N'' = 1$) level in magnitude. The candidates of the upper level of this line pairs are the $^2E'_{3/2}$ ($J' = 1.5$), $^2E'_{1/2}$ ($J' = 0.5$), and $^2E'_{1/2}$ ($J' = 1.5$) levels. The Zeeman splitting enabled us to discriminate from each other clearly. Seven line pairs were assigned to the transitions to the $^2E'_{3/2}$ ($J' = 1.5$), and 15 line pairs were assigned to those to the $^2E'_{1/2}$ ($J' = 0.5$), based on the observed Zeeman splitting and the ground state combination differences. This is the first study that the rotational assignment of the $\tilde{B}$ – $\tilde{X}$ transition in NO_3 radical was successfully carried out. The effective rotational constants of the excited electronic states were estimated. The magnetic *g*-factors of the ground state and the excited states were determined. In the spectrum, many vibronic bands were identified, while only one vibronic 0 – 0 band had been expected to appear. This result indicates that the $\tilde{B}\,^2E'$ (v

= 0) state massively interacts with the surrounding dark vibronic states, and they appeared by the intensity borrowing from the optically allowed $\tilde{B}$ – $\tilde{X}$ electronic transition. From the density of the identified vibronic states, it was concluded that the complicated rotational structure of the observed region mainly owes to the vibronic coupling between the $\tilde{B}\,^2$E' state and the $\tilde{A}\,^2$E" state through the a_2" symmetry vibrational modes. The effective spin-orbit interaction constant of the $\tilde{B}\,^2$E' (v = 0) state was estimated to be –21 cm^{-1}. The Curl's relationship was confirmed to be verified in the ground state of NO_3 radical.

In Chapter 5, the high-resolution laser spectroscopy of $^{15}NO_3$ isotopologue was reported. This is the first high-resolution spectroscopic study of the electronic transition of $^{15}NO_3$ isotopologue. The observed region was 15080 – 15103 cm^{-1}, which is assigned to the 0 – 0 band of the $\tilde{B}\,^2$E' ← $\tilde{X}\,^2A_2$' transition. The $^{15}NO_2$ contamination to the $^{15}NO_3$ spectrum was assumed to be negligible in this region, referring to the $^{14}NO_3$ study in the previous chapter. About 200 strong lines and several thousand weak lines were found. Many rotational line pairs with 0.0248 cm^{-1} spacing were recognized in the spectrum. Eighteen pairs of them were successfully assigned to the transitions from the $\tilde{X}\,^2A_2$' (v" = 0, k" = 0, N" = 1, J" = 0.5 and 1.5) levels, based on the Zeeman splitting and the ground state combination differences. Starting from these line pairs, about 90 rotational lines were finally assigned. The molecular constants of the ground state were determined as B = 0.458544(2) cm^{-1}, D_N = 0.56(2) × 10^{-6} cm^{-1}, and ε_{bb} = –0.01670(4) cm^{-1}. The molecular constants of the $\tilde{B}\,^2E'_{1/2}$ state were

estimated to be T_0 = 15098.20(4) cm^{-1}, B = 0.4282(7) cm^{-1}, and $D_J = 4 \times 10^{-4}$ cm^{-1}, under the perturbation-free assumption. Eight vibronic bands were identified in 15080 – 15103 cm^{-1} region. This complicated structure was concluded to be due to the vibronic coupling between the $\tilde{B}$ ^{2}E' (v = 0) state and the $\tilde{X}$ and $\tilde{A}$ electronic states. Both the two spin-orbit components ^{2}E'$_{1/2}$ and ^{2}E'$_{3/2}$ were identified, and the spin-orbit interaction constant of the $\tilde{B}$ ^{2}E' (v = 0) state was estimated to be –12 cm^{-1} as the lower limit based on the energy separation of these spin-orbit components.

Acknowledgements

The work reported in this doctoral dissertation has been carried out at Molecular Photoscience Research Center in Kobe University under the direction of Professor Shunji Kasahara from April 2012 to December 2014.

First of all, I would like to express my deepest gratitude to Professor Shunji Kasahara (Kobe University) for his continuous support, kind advice, and warm encouragement during the course of study. When I joined his group, he proposed me the challenging and fascinating research project. This project was quite tough for a beginner in molecular spectroscopy; however, now I believe that this project enabled me to grow as a scientist. He provided me not only the fascinating research project but also many opportunities to participate in domestic and international conferences. Everything was really excellent experience.

Second, I am enormously grateful to Professor Takashi Ishiwata (Hiroshima City University) for providing N_2O_5 and its ^{15}N substituted isotopomer as the sample of this study. He also provided me a lot of fruitful advice. Without his kind support, this research project would never be possible.

Third, I would like to express my sincere gratitude to Professor Eizi Hirota (The Graduate University for Advanced Studies), Professor Yasuki Endo (The University of Tokyo), Professor Masaru Fukushima (Hiroshima City University), and Professor Kentarou Kawaguchi

(Okayama University). Fruitful discussion with these giants in high-resolution molecular spectroscopy was excellent experience for me. Simultaneously I learned the stance as a scientist from their meaningful comment. I always remember the comment Professor Hirota told me, “Scientists must pursue tirelessly what they are interested in, for veritable development of Science.”

Fourth, I am sincerely grateful to Professor Akihide Wada (Kobe University) and Professor Keisuke Tominaga (Kobe University) for providing me a lot of advice and guidance as the referees of this doctoral dissertation.

Fifth, my colleagues in Kasahara group in Kobe University; Mr. Kenichiro Kanzawa, Mr. Takumi Nakano, Ms. Tsukiko Takashima, Mr. Wataru Kashihara, Mr. Ryo Yamamoto, Mr. Tsuyoshi Takashino, Ms. Kanon Teramoto, and Ms. Hitomi Matsubara have helped me for experiments and discussion. I would like to thank them for their enormous cooperation.

Sixth, I would like to thank the Research Fellowships of Japan Society for the Promotion of Science for Young Scientists from April 2014.

Last but not least, I would like to express my deepest gratitude to my family. I cannot thank them enough for their unwavering love, continuous support and understanding, and warm encouragement up until now in weal and woe.

Kohei Tada

Kobe, January 2015

References

[1] M. Born, and R. Oppenheimer, *Ann. Physik.* **84**, 457 (1927).

[2] L. D. Landau, and E. M. Lifshitz, *Mechanics, Volume 1 of Course of Theoretical Physics* (Pergamon Press, 1960), Chapters V and VI.

[3] L. D. Landau, and E. M. Lifshitz, *Quantum Mechanics (Non-relativistic Theory), Volume 3 of Course of Theoretical Physics, Second edition* (Pergamon Press, 1965), Chapter XIII.

[4] H. Katô, T. Kobayashi, Y. C. Wang, K. Ishikawa, M. Baba, and S. Nagakura, *Chem. Phys.* **162**, 107 (1992).

[5] H. Katô, T. Kumauchi, K. Nishizawa, M. Baba, and K. Ishikawa, *J. Chem. Phys.* **98**, 6684 (1993).

[6] H. Katô, and M. Baba, *Chem. Rev.* **95**, 2311 (1995).

[7] S. Kasahara, M. Shibata, M. Baba, and H. Katô, *J. Phys. Chem. A* **101**, 422 (1997).

[8] S. Kasahara, Y. Hasui, K. Otsuka, M. Baba, W. Demtröder, and H. Katô, *J. Chem. Phys.* **106**, 4869 (1997).

[9] S. Kasahara, K. Otsuka, M. Baba, and H. Katô, *J. Chem. Phys.* **109**, 3393 (1998).

[10] M. Baba, T. Kokita, S. Kasahara, and H. Katô, *J. Chem. Phys.* **111**, 9574 (1999).

[11] M. H. Kabir, T. Shinano, and S. Kasahara, *J. Chem. Phys.* **118**, 7817 (2003).

[12] R. Criegee, and G. Wenner, *Justus Liebig Ann. Chem.* **564**, 9 (1949).

[13] R. Criegee, *Angew. Chem. Int. Ed. Engl.* **14**, 745 (1975).

[14] Y.-T. Su, Y.-H. Huang, H. A. Witek, and Y. P. Lee, *Science* **340**, 174 (2013).

[15] C. A. Taatjes, O. Welz, A. J. Eskola, J. D. Savee, A. M. Scheer, D. E. Shallcross, B. Rotavera, E. P. F. Lee, J. M. Dke, D. K. W. Mok, D. L. Osborn, and C. J. Percival, *Science* **340**, 177 (2013).

[16] J. M. Beames, F. Liu, L. Lu, and M. I. Lester, *J. Chem. Phys.* **138**, 244307 (2013).

[17] M. Nakajima, and Y. Endo, *J. Chem. Phys.* **139**, 101103 (2013).

[18] M. C. McCarthy, L. Cheng, K. N. Crabtee, O. Martinez, T. L. Nguyen, C. C. Womack, and J. F. Stanton, *J. Phys. Chem. Lett.* **4**, 4133 (2013).

[19] L. Sheps, *J. Phys. Chem. Lett.* **4**, 4201 (2013).

[20] M. Nakajima, and Y. Endo, *J. Chem. Phys.* **140**, 011101 (2014).

[21] F. Liu, J. M. Beames, A. M. Green, and M. I. Lester, *J. Phys. Chem. A* **118**, 2298 (2014).

[22] F. Liu, J. M. Beames, A. S. Petit, A. B. McCoy, and M. I. Lester, *Science* **345**, 1596 (2014).

[23] M. Baba, H. Yamada, and K. Nishizawa, *J. Chem. Phys.* **97**, 4569 (1992).

[24] J. F. Noxon, R. B. Norton, and W. R. Henderson, *Geophys. Res. Lett.* **5**, 675 (1978).

[25] J. F. Noxon, R. B. Norton, and E. Marovich, *Geophys. Res. Lett.* **7**, 125 (1980).

[26] U. Platt, D. Perner, J. Schröder, C. Kessler, and A. Toennissen, *J. Geophys. Res.* **86**, 11965 (1981).

[27] J. P. Naudet, D. Huguenin, P. Rigaud, and D. Cariolle, *Planet. Space Sci.* **29**, 707 (1981).

[28] P. Rigaud, J. P. Naudet, and D. Huguenin, *J. Geophys. Res.* **88**, 1463 (1983).

[29] J. F. Noxon, *J. Geophys. Res.* **88**, 11017 (1983).

[30] J. P. Pommereau, P. Fabian, G. Flentje, M. Helten, H. W. Pätz, D. H. Ehhalt, F. Karcher, G. Froment, G. Armand, W. A. Matthews, D. Offermann, H. Rippel, P. Rigaud, J. P. Naudet, D. Huguenin, P. C. Simon, W. Peetermans, P. Vandeneede, R. Zander, and G. Roland, *Planet. Space Sci.* **35**, 615 (1987).

[31] J. P. Naudet, P. Rigaud, M. Pirre, and D. Huguenin, *J. Geophys. Res.* **94**, 6374 (1989).

[32] S. Solomon, R. W. Sanders, G. H. Mount, M. A. Carroll, R. O. Jakoubek, and A. L. Schmeltekopt, *J. Geophys. Res.* **94**, 16423 (1989).

[33] U. Platt, Fresenius *J. Anal. Chem.* **340**, 633 (1991).

[34] F. Heintz, U. Platt, H. Flentje, and R. Dubois, *J. Geophys. Res.* **101**, 22891 (1996).

[35] N. Carslaw, L. J. Carpenter, J. M. C. Plane, B. J. Allan, R. A. Burgess, K. C. Clemitshaw, H. Coe, and S. A. Penkett, *J. Geophys. Res.* **102**, 18917 (1997).

[36] A. Geyer, B. Alicke, D. Mihelcic, J. Stutz, and U. Platt, *J. Geophys. Res.* **104**, 26097 (1999).

[37] S. Li, W. Liu, P. Xie, A. Li, M. Qin, and K. Dou, *Adv. Atmos. Sci.* **24**, 875 (2007).

[38] S. Li, W. Liu, P. Xie, A. Li, M. Qin, F. Peng, and Y. Zhu, *J. Environ. Sci.* **20**, 45 (2008).

[39] D. Asaf, E. Tas, D. Pedersen, M. Peleg, and M. Luria, *Environ. Sci. Technol.* **44**, 5901

(2010).

[40] V. F. Sofieva, N. Kalakoski, P. T. Verronen, S.-M. Päivärinta, E. Kyrölä, L. Backman, and J. Tamminen, *Atmos. Chem. Phys.* **12**, 1051 (2012).

[41] R. P. Wayne, I. Barnes, P. Biggs, J. P. Burrows, C. E. Canosa-Mas, J. Hjorth, G. Le Bras, G. K. Moortgat, D. Perner, G. Poulet, G. Restelli, and H. Sidebottom, *Atmos. Environ.* **25**, 1 (1991).

[42] R. Atkinson, *Atmos. Environ.* **34**, 2063 (2000).

[43] J. Chappuis, *Ann. Sci. l'É.N.S. 2e série* **11**, 137 (1882).

[44] E. J. Jones, and O. R. Wulf, *J. Chem. Phys.* **5**, 873 (1937).

[45] A. D. Walsh, *J. Chem. Soc.* 2301 (1953).

[46] T. E. H. Walker, and J. A. Horsley, *Mol. Phys.* **21**, 939 (1971).

[47] H. H. Nelson, L. Pasternack, and J. R. McDonald, *J. Phys. Chem.* **87**, 1286 (1983).

[48] T. Ishiwata, I. Fujiwara, Y. Naruge, K. Obi, and I. Tanaka, *J. Phys. Chem.* **87**, 1349 (1983).

[49] B. Kim, P. L. Hunter, and H. S. Johnson, *J. Chem. Phys.* **96**, 4057 (1992).

[50] J. F. Stanton, J. Gauss, and R. J. Bartlett, *J. Chem. Phys.* **94**, 4084 (1991).

[51] R. R. Friedl, and S. P. Sander, *J. Phys. Chem.* **91**, 2721 (1987).

[52] T. Ishiwata, I. Tanaka, K. Kawaguchi, and E. Hirota, *J. Chem. Phys.* **82**, 2196 (1985).

[53] K. Kawaguchi, E. Hirota, T. Ishiwata, and I. Tanaka, *J. Chem. Phys.* **93**, 951 (1990).

[54] E. Hirota, K. Kawaguchi, T. Ishiwata, and I. Tanaka, *J. Chem. Phys.* **95**, 771 (1991).

[55] E. Hirota, *Bull. Chem. Soc. Jpn.* **68**, 1 (1995).

[56] K. Kawaguchi, T. Ishiwata, I. Tanaka, and E. Hirota, *Chem. Phys. Lett.* **180**, 436 (1991).

[57] T. Ishiwata, I. Tanaka, K. Kawaguchi, and E. Hirota, *J. Mol. Spectrosc.* **153**, 167 (1992).

[58] K. Kawaguchi, T. Ishiwata, E. Hirota, and I. Tanaka, *Chem. Phys.* **231**, 198 (1998).

[59] J. F. Stanton, *J. Chem. Phys.* **126**, 134309 (2007).

[60] J. F. Stanton, *Mol. Phys.* **107**, 1059 (2009).

[61] C. S. Simmons, T. Ichino, and J. F. Stanton, *J. Phys. Chem. Lett.* **3**, 1946 (2012).

[62] A. Weaver, D. W. Arnold, S. E. Bradforth, and D. M. Neumark, *J. Chem. Phys.* **94**, 1740 (1991).

[63] M. Mayer, L. S. Cederbaum, and H. Köppel, *J. Chem. Phys.* **100**, 899 (1994).

[64] R. D. Davy, and H. F. Schaefer, *J. Chem. Phys.* **91**, 4410 (1989).

[65] U. Kaldor, *Chem. Phys. Lett.* **166**, 599 (1990).

[66] E. D. Glendening, and A. M. Halpern, *J. Chem. Phys.* **127**, 264307 (2007).

[67] C. Schäfer, and C. Bormuth, *Z. Physik* **62**, 508 (1930).

[68] T. G. Kujumzelis, *Z. Physik* **109**, 586 (1938).

[69] D. Forney, W. E. Thompson, and M. E. Jacox, *J. Chem. Phys.* **99**, 7393 (1993).

[70] M. E. Jacox, and W. E. Thompson, *J. Chem. Phys.* **129**, 204306 (2008).

[71] H. Beckers, H. Willner, and M. E. Jacox, *ChemPhysChem* **10**, 706 (2009).

[72] T. Ishiwata, Y. Nakano, K. Kawaguchi, E. Hirota, and I. Tanaka, *J. Phys. Chem. A* **114**,

980 (2010).

[73] K. Kawaguchi, N. Shimizu, R. Fujimori, J. Tang, T. Ishiwata, and I. Tanaka, *J. Mol. Spectrosc.* **268**, 85 (2011).

[74] R. Fujimori, N. Shimizu, J. Tang, T. Ishiwata, and K. Kawaguchi, *J. Mol. Spectrosc.* **283**, 10 (2013).

[75] K. Kawaguchi, R. Fujimori, J. Tang, and T. Ishiwata, *J. Phys. Chem. A* **117**, 13732 (2013).

[76] B. Kim, H. S. Johnston, D. A. Clabo, and H. F. Schaefer, *J. Chem. Phys.* **88**, 3204 (1988).

[77] E. Hirota, T. Ishiwata, K. Kawaguchi, M. Fujitake, N. Ohashi, and I. Tanaka, *J. Chem. Phys.* **107**, 2829 (1997).

[78] A. Deev, J. Sommar, and M. Okumura, *J. Chem. Phys.* **122**, 224305 (2005).

[79] M. Okumura, J. F. Stanton, A. Deev, and J. Sommar, *Phys. Scr.* **73**, C64 (2006).

[80] J. F. Stanton, and M. Okumura, *Phys. Chem. Chem. Phys.* **11**, 4742 (2009).

[81] K. Takematsu, N. C. Eddingsaas D. J. Robichaud, and M. Okumura, *Chem. Phys. Lett.* **555**, 57 (2013).

[82] M. E. Jacox, and W. E. Thompson, *J. Phys. Chem. A* **114**, 4712 (2010).

[83] S. Mahapatra, W. Eisfeld, and H. Köppel, *Chem. Phys. Lett.* **441**, 7 (2007).

[84] S. Faraji, H. Köppel, W. Eisfeld, and S. Mahapatra, *Chem. Phys.* **347**, 110 (2008).

[85] H. F. Davis, P. I. Ionov, S. I. Ionov, and C. Wittig, *Chem. Phys. Lett.* **215**, 214 (1993).

[86] H. F. Davis, B. Kim, H. S. Johnston, and Y. T. Lee, *J. Phys. Chem.* **97**, 2172 (1993).

[87] L. Valachovic, C. Riehn, K. Mikhaylichenko, and C. Wittig, *Chem. Phys. Lett.* **258**, 644 (1996).

[88] K. Mikhaylichenko, C. Riehn, L. Valachovic, A. Sanov, and C. Wittig, *J. Chem. Phys.* **105**, 6807 (1996).

[89] M. P. Grubb, M. L. Warter, K. M. Johnson, and S. W. North, *J. Phys. Chem. A* **115**, 3218 (2011).

[90] H. Xiao, S. Maeda, and K. Morokuma, *J. Phys. Chem. Lett.* **2**, 934 (2011).

[91] M. J. T. Jordan, and S. H. Kable, *Science* **335**, 1054 (2012).

[92] M. P. Grubb, M. L. Walter, H. Xiao, S. Maeda, K. Morokuma, and S. W. North, *Science* **335**, 1075 (2012).

[93] H. Xiao, S. Maeda, and K. Morokuma, *J. Chem. Theo. Comput.* **8**, 2600 (2012).

[94] B. Fu, J. M. Bowman, H. Xiao, S. Maeda, and K. Morokuma, *J. Chem. Theo. Comput.* **9**, 893 (2013).

[95] D. A. Ramsay, "Optical spectra of gaseous free radicals," in *Proc. 10th Colloq. Spectrosc. Int.* (Spartan Books, Washington, DC, 1963), p. 583.

[96] H. S. Johnston, and R. Graham, *Can. J. Chem.* **52**, 1415 (1974).

[97] D. N. Mitchell, R. P. Wayne, P. J. Allen, R. P. Harrison, and R. J. Twin, *J. Chem. Soc. Faraday Trans. II* **76**, 785 (1980).

[98] W. J. Marinelli, D. M. Swanson, and H. S. Johnston, *J. Chem. Phys.* **76**, 2864 (1982).

[99] A. R. Ravishankara, and P. H. Wine, *Chem. Phys. Lett.* **101**, 73 (1983).

[100] S. P. Sander, *J. Phys. Chem.* **90**, 4135 (1986).

[101] R. J. Yokelson, J. B. Burkholder, R. W. Fox, R. K. Talukdar, and A. R. Ravishankara, *J. Phys. Chem.* **98**, 13144 (1994).

[102] S. M. Ball, I. M. Povey, E. G. Norton, and R. L. Jones, *Chem. Phys. Lett.* **342**, 113 (2001).

[103] J. Orphal, C. E. Fellows, and P.-M. Flaud, *J. Geophys. Res.* **108**, 4077 (2003).

[104] R. T. Carter, K. F. Schmidt, H. Bitto, and J. R. Huber, *Chem. Phys. Lett.* **257**, 297 (1996).

[105] M. J. Frisch, G. W. Trucks, H. B. Schlegel, G. E. Scuseria, M. A. Robb, J. R. Cheeseman, J. A. Montgomery, Jr., T. Vreven, K. N. Kudin, J. C. Burant, J. M. Millam, S. S. Iyengar, J. Tomasi, V. Barone, B. Mennucci, M. Cossi, G. Scalmani, N. Rega, G. A. Petersson, H. Nakatsuji, M. Hada, M. Ehara, K. Toyota, R. Fukuda, J. Hasegawa, M. Ishida, T. Nakajima, Y. Honda, O. Kitao, H. Nakai, M. Klene, X. Li, J. E. Knox, H. P. Hratchian, J. B. Cross, C. Adamo, J. Jaramillo, R. Gomperts, R. E. Stratmann, O. Yazyev, A. J. Austin, R. Cammi, C. Pomelli, J. W. Ochterski, P. Y. Ayala, K. Morokuma, G. A. Voth, P. Salvador, J. J. Dannenberg, V. G. Zakrzewski, S. Dapprich, A. D. Daniels, M. C. Strain, O. Farkas, D. K. Malick, A. D. Rabuck, K. Raghavachari, J. B. Foresman, J. V. Ortiz, Q. Cui, A. G. Baboul, S. Clifford, J. Cioslowski, B. B. Stefanov, G. Liu, A. Liashenko, P. Piskorz, I. Komaromi, R. L. Martin, D. J. Fox, T. Keith, M. A. Al-Laham, C. Y. Peng, A. Nanayakkara, M. Challacombe, P. M. W. Gill, B. Johnson, W. Chen, M. W. Wong, C.

Gonzalez, and J. A. Pople, Gaussian 03, Revision B.05, Gaussian, Inc., Pittsburgh PA, 2003.

[106] L. Dogliotti, and E. Hayon, *J. Phys. Chem.* **71**, 3802 (1967).

[107] M. S. Child, and H. C. Longuet-Higgins, *Phil. Trans. R. Soc. Lond. A* **254**, 259 (1961).

[108] J. M. Brown, *Mol. Phys.* **20**, 817 (1971).

[109] G. Racah, *Phys. Rev.* **62**, 438 (1942).

[110] E. Hirota, *High-Resolution Spectroscopy of Transient Molecules* (Springer-Verlag, Berlin, 1985), p. 65.

[111] Y. Endo, S. Saito, and E. Hirota, *J. Chem. Phys.* **81**, 122 (1984).

[112] U. Fano, and G. Racah, *Irreducible Tensorial Sets* (Academic Press, 1959), Section I-5.

[113] H. Katô, *Bull. Chem. Soc. Jpn.* **66**, 3203 (1993).

[114] W. Demtröder, *Laser Spectroscopy Fourth Edition; Volume 1 Basic Principles* (Springer-Verlag, Berlin, Heidelberg, 2008), p. 71.

[115] H. H. Nelson, L. Pasternack, and J. R. McDonald, *J. Chem. Phys.* **79**, 4279 (1983).

[116] A. E. Douglas, *J. Chem. Phys.* **45**, 1007 (1966).

[117] P. F. Bernath, *Spectra of Atoms and Molecules Second Edition* (Oxford, 2005), p. 31.

[118] P. Connell, and H. S. Johnston, *Geophys. Res. Lett.* **6**, 553 (1979).

[119] T. Ide, T. Nakayama, K. Takahashi, and Y. Matsumi, *Int. J. Chem. Kinet.* **40**, 679 (2008).

[120] H. Herrmann, M. Exner, and R. Zellner, *Geochim. Cosmochim. Acta* **58**, 3239 (1994).

[121] B. A. Flowers, M. E. Angerhofer, W. R. Simpson, T. Nakayama, and Y. Matsumi, *J. Phys. Chem. A* **109**, 2552 (2005).

[122] M. Berglund, and M. E. Wieser, *Pure Appl. Chem.* **83**, 397 (2011).

[123] A. Kantrowitz, and J. Grey, *Rev. Sci. Instrum.* **22**, 328 (1951).

[124] J. B. Anderson, and J. B. Fenn, *Phys. Fluids* **8**, 780 (1965).

[125] R. E. Smalley, L. Wharton, and D. H. Levy, *J. Chem. Phys.* **63**, 4977 (1975).

[126] N. Mikami, *Oyo Buturi* **49**, 802 (1980).

[127] W. Gerlach, and O. Stern, *Z. Physik* **9**, 353 (1922).

[128] S. Gerstenkorn, and P. Luc, *Atlas du spectre d'absorption de la molecule d'iode 14800 – 20000 cm^{-1}* (CNRS, Paris, 1978).

[129] A. Arie, S. Schiller, E. K. Gustafson, and R. L. Byer, *Opt. Lett.* **17**, 1204 (1992).

[130] R. W. P. Drever, J. L. Hall, F. V. Kowalski, J. Hough, G. M. Ford, A. J. Munley, and H. Ward, *Appl. Phys. B* **31**, 97 (1983).

[131] H. Katô, M. Baba, S. Kasahara, K. Ishikawa, M. Misono, Y. Kimura, J. O'Reilly, H. Kuwano, T. Shimamoto, T. Shinano, C. Fujiwara, M. Ikeuchi, N. Fujita, M. H. Kabir, M. Ushino, R. Takahashi, and Y. Matsunobu, *Doppler-Free High Resolution Spectral Atlas of Iodine Molecule 15000 to 19000 cm^{-1}* (JSPS, Tokyo, 2000).

[132] W. A. Rosser, and H. Wise, *J. Chem. Phys.* **24**, 493 (1956).

[133] E. S. Fishburne, D. M. Bergbauer, and R. Edse, *J. Chem. Phys.* **43**, 1847 (1965).

[134] E. Zimet, *J. Chem. Phys.* **53**, 515 (1970).

[135] M. Röhrig, E. L. Petersen, D. F. Davidson, and R. K. Hanson, *J. Chem. Kinet.* **29**, 483 (1997).

[136] G. Herzberg, *Molecular Spectra and Molecular Structure Volume I – Spectra of Diatomic Molecules* (Krieger, 1989), p. 558.

[137] G. Herzberg, *Molecular Spectra and Molecular Structure Volume II – Infrared and Raman Spectra of Polyatomic Molecules* (Krieger, 1991), Section II-3.

[138] E. B. Wilson, J. C. Decius, and P. C. Cross, *Molecular Vibrations, The Theory of Infrared and Raman Vibrational Spectra* (McGraw-Hill, 1955), Section 7-3.

[139] T. J. Codd, M.-W. Chen, M. Roudjane, and T. A. Miller, *67th Int. Symp. Mol. Spectrosc.* (Ohio, 2012), TI01.

[140] H. Lefebvre-Brion, and R. W. Field, *The Spectra and Dynamics of Diatomic Molecules* (Elsevier, 2004), p. 316.

[141] D. Mihelcic, A. Volz-Thomas, H. W. Pätz, D. Kley, and M. Mihelcic, *J. Atmos. Chem.* **11**, 271 (1991).

[142] R. F. Curl, *Mol. Phys.* **9**, 585 (1965).

[143] K. Tada, W. Kashihara, M. Baba, T. Ishiwata, E. Hirota, and S. Kasahara, *J. Chem. Phys.* **141**, 184307 (2014).

[144] E. A. Volkers, A. Vredenborg, H. Linnartz, J. Bulthuis, S. Stolte, and R. Jost, *Chem. Phys.*

Lett. **391**, 106 (2004).

[145] E. A. Volkers, M. C. Koudijzer, A. Vredenborg, J. Bulthuis, S. Stolte, H. Linnartz, and R. Jost, *J. Mol. Spectrosc.* **235**, 1 (2006).